



A University of Sussex MPhil thesis

Available online via Sussex Research Online:

<http://sro.sussex.ac.uk/>

This thesis is protected by copyright which belongs to the author.

This thesis cannot be reproduced or quoted extensively from without first obtaining permission in writing from the Author

The content must not be changed in any way or sold commercially in any format or medium without the formal permission of the Author

When referring to this work, full bibliographic details including the author, title, awarding institution and date of the thesis must be given

Please visit Sussex Research Online for more information and further details

UNIVERSITY OF SUSSEX

**KINEMATIC ANALYSIS OF SEA CLIFF STABILITY USING UAV
PHOTOGRAMMETRY**

IGNACIO EDUARDO IBARRA COFRÉ.

MPhil IN PHYSICAL GEOGRAPHY
(Subtopic: APPLIED GEOMORPHOLOGY)

JUNE, 2017

SUMMARY

The coastal systems of East Sussex historically have been exposed to coastline retreat and sea cliff instability processes. Under this scenario, it is important to understand, quantify and model potential modes of slope failure, as it is a required stage in mitigating cliff instability hazards. Small unmanned aerial vehicles (UAVs) or drones are new types of aerial platforms from which high-resolution remote sensing measurements of landforms can be obtained. This research uses close range digital photogrammetry from an UAV to perform a kinematic slope stability analysis of chalk sea cliffs located at Telscombe, United Kingdom. The overall technique for data collection involved installation of a megapixel full frame digital camera on board an octocopter. Ground control for the survey was conducted using dGPS and total station surveying. The digital photogrammetry processing was undertaken in 3DM Analyst Mine Mapping Suite software. 210 individual Digital Terrain Models with a computed image accuracy of 0.25 pixels and a standard error around the control network of 0.13m were obtained. Rock mass discontinuities such as joints, faults and bedding planes were then manually mapped on the DTMs. These data were then used to assess differing modes of slope failure using stereographic projections for kinematic analysis. The results show that wedge failure is by far the most likely mode of slope instability, since 39% of the discontinuity intersections are favourable to wedge collapse occurring. Planar sliding is the second probable mode of slope failure, comprising 8% of all mapped joints. These types of cliff collapses are consistent with the dominant types of failures determined from other studies carried out on the Chalk cliffs between Brighton and Newhaven. The findings provide further understanding and numerical data about potential modes of cliff failure for the Newhaven Chalk of Sussex, and demonstrated the usefulness of using UAV photogrammetry for examining coastal geo-hazards.

Key words: UAV, photogrammetry, sea cliffs, kinematic analysis

Acknowledgements

I would like to thanks to Dr. John Barlow and Dr. Roger Moore for their supervision and guidance to carry out this research project, and to have taught me many aspects and techniques related to Applied Geomorphology. To the Internal and external examiners, for their helpful revisions that greatly improved the research. To Jamie Gilham for the technical guidance and support during several methodological stages. Many thanks to my lovely kathy, parents, brothers, and friends that form my world.

Table of contents

LIST OF FIGURES	1
LIST OF TABLES	3
LIST OF APPENDICES	3
LIST OF ABBREVIATIONS	3
1. INTRODUCTION	4
1.2 AIM AND OBJECTIVES	6
1.3 SITE DESCRIPTION	7
1.3.1 <i>Location and climate</i>	7
1.3.2 <i>Geological setting</i>	8
2. LITERATURE REVIEW	10
2.1 DIGITAL PHOTOGRAMMETRY	10
2.1.1 <i>Principles of photogrammetric measurement</i>	10
2.1.2 <i>Coordinate transformations between image and terrain</i>	13
2.1.3 <i>Space intersection</i>	15
2.1.3.1 Normal stereo model case	15
2.1.3.2 General stereo pair case	16
2.1.3.3 Multi-image processing	18
2.1.4 <i>Image matching</i>	18
2.1.4.1 Area-based matching	18
2.1.4.2 Feature-based matching	19
2.2 ROCK SLOPE DISCONTINUITIES AND KINEMATIC ANALYSIS	20
2.2.1 <i>Mechanisms of formation of discontinuities</i>	20
2.2.2 <i>Properties of discontinuities relative to the slope instability</i>	22
2.2.3 <i>Kinematic analysis</i>	24
2.2.4 <i>Stereographic analysis of discontinuity data</i>	25
2.3 GEOLOGY, GEOMORPHOLOGY AND CLIFF STABILITY AT THE STUDY SITE	26
2.3.1 <i>Stratigraphy</i>	26
2.3.1.1 Newhaven Chalk Formation	26
2.3.1.2 Culver Chalk Formation	29
2.3.2 <i>Geomorphological and environmental processes</i>	31
3. METHODOLOGY	33
3.1 DATA COLLECTION	33
3.1.1 <i>Topographic survey</i>	34
3.1.2 <i>Unmanned aerial vehicle for photogrammetric survey</i>	36
3.1.2.1 Photogrammetric project design and flight plan	36
3.1.2.2 UAV survey	38
3.1.2.3 Camera properties and settings	40
3.2 PHOTOGRAMMETRIC PROCESSING	42
3.2.1 <i>Interior orientation: camera calibration</i>	43
3.2.1.1 Self-calibrating bundle adjustment	43
3.2.1.2 Interior orientation: output report	44
3.2.2 <i>Absolute and exterior orientation</i>	45
3.2.2.1 Digitising ground control points on Images	45
3.2.2.2 Relative only points generation	46
3.1.2.3 Image resection	47
3.1.2.4 Multi-image processing by bundle adjustment	48

3.2.3 <i>Epipolar images and DTM generation</i>	49
3.3 DISCONTINUITY MAPPING	50
3.4 KINEMATIC ANALYSIS	52
3.4.1 <i>Identification of modes of slope instability</i>	52
3.4.1.1 Geometrical conditions for plane failure	52
3.4.1.2 Geometrical conditions for wedge failure	54
3.4.1.3 Geometrical conditions for flexural toppling	56
3.4.1.4 Geometrical conditions for direct toppling	58
3.4.2. <i>Parameters used for modelling the kinematic analysis</i>	60
3.4.2.1 Friction angle	60
3.4.2.2 Dip and dip direction	61
3.4.2.3 Definition of cliff sections	62
4. RESULTS	64
4.1 DIGITAL TERRAIN MODELS	64
4.2 DISCONTINUITY MAPPING	73
4.2.1 <i>Frequency distribution of discontinuities</i>	79
4.2.1.1 Joints	79
4.2.1.2 Faults	81
4.2.1.3 Bedding Planes	82
4.3 KINEMATIC ANALYSIS	84
4.3.1 <i>Stereonet assessment</i>	84
4.3.2 <i>General kinematic analysis</i>	89
4.3.2.1 Planar sliding	89
4.3.2.2 Wedge sliding	90
4.3.2.3 Flexural toppling	93
4.3.2.4. Direct toppling	94
4.3.3 <i>Kinematic analysis of cliff sections</i>	95
4.3.4 <i>Kinematic sensitivity analysis</i>	100
5. DISCUSSION	103
5.1. THE SELECTION CRITERIA USED FOR MAPPING DISCONTINUITY SURFACES	103
5.2 THE CAPABILITY OF UAV PHOTOGRAMMETRY FOR THE MEASUREMENT OF PROPERTIES OF DISCONTINUITIES RELATIVE TO SLOPE STABILITY	105
5.3 THE RELATIVE PERFORMANCE OF DIGITAL PHOTOGRAMMETRY AGAINST TLS AND DIRECT FIELD ASSESSMENT FOR MEASURING DIP AND DIP DIRECTION	106
6. CONCLUSIONS	109
REFERENCES	111
APPENDIX	124

List of figures

Figure 1: Study area, East Sussex, England.....	7
Figure 2: Map of chalk formations forming the Downs and cliffs of East Sussex	8
Figure 3: Telscombe Cliffs formed of Newhaven Chalk, locally capped by Culver Chalk	9
Figure 4: Principle of central perspective projection	11
Figure 5: Geometry in an oriented stereo pair model	12
Figure 6: Image and object coordinate systems	14
Figure 7: Normal case of stereo photogrammetry	16
Figure 8: Spatial intersection for the general stereo case	16
Figure 9: Cross correlation coefficients for area-based matching.....	19
Figure 10: Formation of joints due to burial and uplift of a rock mass	21
Figure 11: Geometrical properties of discontinuities controlling slope stability	24
Figure 12: Chalk stratigraphy of Newhaven and Culver Chalk formations	26
Figure 13: Newhaven to Brighton cliffs. The Peacehaven type of failures	28
Figure 14: General methodological workflow	33
Figure 15: Equipment and targets used for the topographic survey	34
Figure 16: Topographic survey map and view of the cliff face with GCPs.....	35
Figure 17: Strip of models with actual distance and base used for the project design	36
Figure 18: DJI S1000 octocopter and Nikon D810 FX DSLR camera.....	38
Figure 19: UAV flight path	39
Figure 20: UAV remote controls and its screens	40
Figure 21: Photogrammetric workflow executed in 3DM Analyst Mine Mapping Suit	42
Figure 22: Schematic interior orientation and its principal parameters	43
Figure 23: Survey target markers and example of the its placement on the cliff face	46
Figure 24: Generation of ROPs during the exterior orientation process	47
Figure 25: Schematic multi-image triangulation using bundle adjustment.....	48
Figure 26: Example of epipolar images of the photogrammetric processing	49
Figure 27: Example of mapped joints based on a DTM	51
Figure 28: Geometrical conditions of a slope showing plane failure	53
Figure 29: Stereographical depiction of structural conditions for planar failure	54
Figure 30: Geometrical conditions of a slope showing wedge failure	55
Figure 31: Scheme of direct and flexural toppling	56
Figure 32: Construction of stereonet overlay for flexural toppling.....	58
Figure 33: Construction of stereonet overlay for direct toppling	59
Figure 34: Determination of dip using Cloud Compare.....	61
Figure 35: Determination of dip direction using Cloud Compare	62
Figure 36: Definition of cliff sections.....	63
Figure 37: General view of Digital Terrain Models showing cliff sections	69
Figure 38: Cliff section 1 (S1), showing notch measurements	70
Figure 39: Cliff section 2 (S2), showing notch measurements	70
Figure 40: Cliff section 3 (S3), showing notch measurements	71
Figure 41: Cliff section 4 (S4), showing notch measurements	71
Figure 42: Cliff section 5 (S5), showing notch measurements (oblique view).....	72
Figure 43: Frontal view of all digitally mapped discontinuities	75
Figure 44: Discontinuities in the eastern section (S1: dip/dip direction = $71^{\circ}/207^{\circ}$). Number of mapped discontinuities: 71	76
Figure 45: Discontinuities in central-eastern section (S2: dip/dip direction = $75^{\circ}/204^{\circ}$). Number of mapped discontinuities: 87.	76

Figure 46: Discontinuities in the central section (S3: dip/dip direction = 81°/202°). Number of mapped discontinuities: 143.	77
Figure 47: Discontinuities in the central-wester section (S4: dip/dip direction = 80°/199°). Number of mapped discontinuities: 147.	77
Figure 48: Discontinuities in the western section (S5: dip/dip direction = 73°/207°). Number of mapped discontinuities: 41.	78
Figure 49: Histogram of jointing dip angle	79
Figure 50: Histogram of jointing dip direction	80
Figure 51: Histogram of jointing persistence	80
Figure 52: Histogram of faulting dip angle	81
Figure 53: Histogram of faulting dip direction	81
Figure 54: Histogram of faulting persistence	82
Figure 55: Histogram of bedding planes dip angle	83
Figure 56: Histogram of bedding planes dip direction	83
Figure 57: Rosette diagram of the cliff face and orientation all discontinuities	84
Figure 58: Stereographic projection with pole and contour plots	85
Figure 59: Great circles of discontinuities, cliff face and lines of intersections (I_n)	86
Figure 60: 2-dimensional modelling (not to scale) of the cliff face, I_1 and I_2	87
Figure 61: Fractures filled with layers of flints controlling chalk prone to slide	88
Figure 62: Progressive opening of tension-cracks, sub-parallel to the cliff face	88
Figure 63: Stereographic model of kinematic analysis for planar sliding	89
Figure 64: Examples of two actual joints prone to slide	90
Figure 65: Critical intersections and contours of density concentrations	91
Figure 66: Critical and non-critical intersections associated with wedge failure	91
Figure 67: Telscombe cliff face formed by two intersecting planes	92
Figure 68: Kinematic Analysis of JS1 = 72°/181° and JS2 = 68°/240°	92
Figure 69: Kinematic analysis for flexural toppling	93
Figure 70: Kinematic analysis for direct toppling	94
Figure 71: Blocks formed by orthogonal joints, with horizontal BP at the base	94
Figure 72: Kinematic analysis by cliff section	97
Figure 73: Wedge failure produced between site visits	98
Figure 74: Kinematic Analysis of wedge failure produced between site inspection	99
Figure 75: Critical percentages v/s ϕ of planar sliding	100
Figure 76: Critical percentages v/s ϕ of wedge sliding	101
Figure 77: Critical percentages v/s ϕ of flexural toppling	102

List of tables

Table 1: Summary of physical properties of the Newhaven Chalk	29
Table 2: Summary of physical properties of the Culver Chalk.....	30
Table 3: DJI S1000 octocopter characteristics	38
Table 4: Nikon D810 properties and settings used for capturing scenes.....	40
Table 5: Camera calibration correlation matrix	44
Table 6: Ranges of dip and dip direction per cliff section.....	63
Table 7: Characteristics of the individual DTMs used for mapping.....	64
Table 8: Summary of model accuracy	64
Table 9: Morphometric characteristics for cliff sections	69
Table 10: Summary of the data obtained from discontinuity mapping	73
Table 11: Characteristics of intersections between sets of discontinuities	86
Table 12: Percentages of critical intersections and poles by cliff section	95

List of appendices

Appendix 1: Object Distance Calculation Spreadsheet (ODCS)	124
Appendix 2: Digital photogrammetry	124
Appendix 3: Interior orientation report	129
Appendix 4: Exterior orientation report.....	131
Appendix 5: Input data table for kinematic analysis	134

List of abbreviations

- CRTDP: Close-Range Terrestrial Digital Photogrammetry
- 3DSE: Three-Dimensional Standard Error
- dGPS: differential Global Positioning System
- DTMs: Digital Terrain Models
- GCPs: Ground Control Points
- JS1/JS2: Joint Set 1 / Joint Set 2
- KSA: Kinematic Sensitivity Analysis
- ODCS: Object Distance Calculation Spreadsheet
- PDOP: Position Dilution of Precision
- PPK: Post Processing Kinematic
- RMS: Root Mean Square
- ROPs: Relative Only Points
- TLS: Terrestrial Laser Scanning
- UAV: Unmanned Aerial Vehicle

1. INTRODUCTION

Sea cliff instability is increasingly an issue for government agencies and local authorities around the world (Stavrou et al., 2011). Indeed, due to marine erosion, weathering, mass wasting processes and geological controls (McInnes and Moore, 2011; Moore and Davis, 2015), most of the chalk cliffs of northwest Europe and specifically southeast England suffer from frequent cliff failures (Stavrou et al., 2011). To illustrate, according to the distribution of cliff behaviour units (CBU) in England and Wales (Halcrow Group Ltd, 2002) an estimated 3,327 km (53%) of coastline are prone to cliff instability processes (Moore and Davis, 2015). Furthermore, in the context of climate change, the identification of the location, magnitude, frequency and modes of cliff failures is important for coastal planners and engineers (Mortimore et al., 2004a). Hence, high-precision monitoring of cliffs, geometrical rock slope characterization and slope stability assessment are required to mitigate chalk cliff failures.

In this context, this research uses digital photogrammetry of aerial imagery captured by an unmanned aerial vehicle (UAV) to characterise rock cliff parameters for kinematic slope stability analysis. Telscombe cliffs are an ideal study site (Figure 1) since they are an undefended cliff section, meaning that marine erosion is an active agent at the base of the cliff, and where cliff failures are mainly controlled by the lithology and structure of the Chalk, the geomorphological configuration, wave action and climatic conditions (Mortimore et al., 2004a). Moreover, this research demonstrates the value and issues of using UAV photogrammetry when assessing modes of slope failure.

An UAV is a remotely operated aircraft designed to operate with no human pilot onboard (Remondino et al., 2011). UAV photogrammetry describes photogrammetric measurement platforms, equipped with a photogrammetric measurement system (e.g. a digital camera). UAVs are low-cost alternatives to classical manned aerial photogrammetry (Eisenbeiss, 2008), and provide a manoeuvrable aerial platform to acquire high-resolution, detailed images and associated digital terrain models (DTMs) to study earth-surface processes (James and Robson, 2014).

Remote-sensing techniques such as close-range terrestrial digital photogrammetry (CRTDP) and UAV photogrammetry represent promising alternatives to common rock engineering scanline or window mapping methods to study the stability of rocky slopes and associated geohazards (Salvini et al., 2013; Francioni et al., 2015). The range of UAV Photogrammetry applications in engineering geology/geomorphology can be seen

in Haarbrink and Eisenbeiss (2008), Eisenbeiss (2009), Niethammer et al. (2010), Hugenholtz et al. (2013), and Francioni et al. (2015).

Furthermore, the emergence of UAV systems together with the emergence of digital cameras and numerous software systems for processing digital data have supplied a new method for data collection, from which results of similar accuracy can be obtained but with less data capture time and lower costs when compared with terrestrial laser scanning (TLS) and airborne and terrestrial light detection and ranging (LiDAR) (Slatton et al., 2007; Remondino et al., 2011; Hugenholtz et al., 2013).

Some important advantages provided by CRTDP and UAV photogrammetry for rock slope characterization are as follows (Sturzenegger and Stead, 2009a):

- a) The capability to sample large survey areas that are not limited to the base of steep and high rock slopes, provides more representative statistical samples. In the specific case of UAV photogrammetry, optimally acquired aerial images can be obtained, avoiding the access to difficult sites in complex slope zones. It also, enables the acquisition of repeat surveys at high frequency and at a relatively low cost.
- b) Risk reduction for workers since the survey can be accomplished from a remote and safe location.
- c) The generation of regular monitoring/inventories of the rock face conditions at a specific time provides the basis for engineering geological/geomorphological change detection.
- d) Discontinuity orientation measurements can be obtained when classical compass clinometer readings are affected by magnetic orebodies, hence avoiding potential orientation bias.

The thesis is organized as follows: first it presents the site description, followed by a literature review of digital photogrammetry, rock slope discontinuities, kinematic analysis, geology and geomorphology of the study site and their influence on cliff stability. Second, it describes the methodology, which is subdivided into three sections with their corresponding chapters of results as follows: a) data collection and photogrammetric processing; b) discontinuity mapping on the obtained 3D model; and c), stereographic projections for the kinematic analysis of the studied failure modes. Finally, it presents relevant research conclusions.

1.2 AIM AND OBJECTIVES

Aim

- The aim of the thesis is to examine potential modes of cliff failure at Telscombe cliffs, East Sussex using kinematic slope stability analysis and UAV Photogrammetry.

The objectives are to:

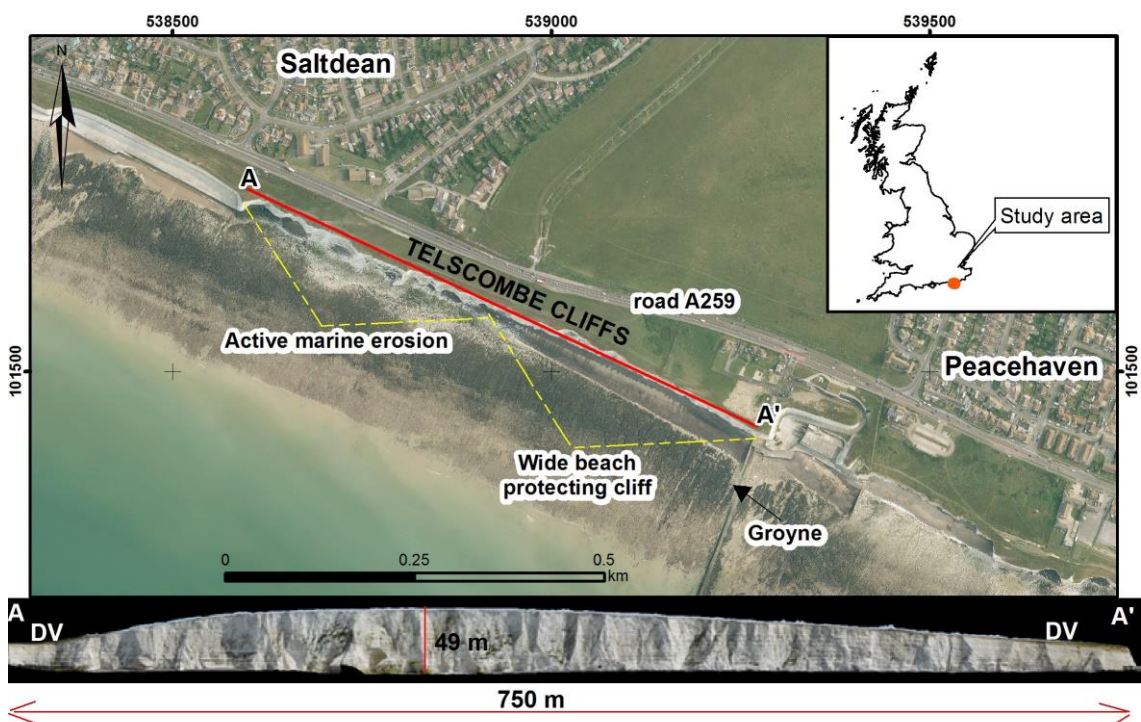
- generate a high resolution digital terrain model using digital photogrammetry of aerial imagery captured from an UAV;
- map rock mass discontinuities on DTMs and obtain geo-engineering data such as dip, dip direction, and persistence;
- determine potential rock slope failure mechanisms such as planar, wedge and toppling using stereographic projection technique for kinematic analysis; and
- examine the most probable modes of cliff failure by cliff section, based on homogeneous dip direction zones of the cliff face.

1.3 SITE DESCRIPTION

1.3.1 Location and climate

Telscombe cliffs are located in East Sussex in the south of England, between the towns of Saltdean and Peacehaven. The study area encompasses 750 m of unprotected cliffs, which have a near-vertical slope profile and a maximum height of 49 m. Telscombe cliffs maintain a fairly constant aspect trending WNW-ESE. The section is bordered by two dry hanging valleys, which are located at either end of the study area. At the base of the cliffs, a well-defined pebble beach and shore platform are present. A concrete groyne, located at the eastern end of Telscombe, provides an artificial obstacle to the movement of beach sediments, thereby creating a wide beach (about 35m) that protects the cliff base against marine erosion at the eastern section of the study site. This barrier creates two geomorphological zones in terms of the degree of exposure to marine erosion at the cliff base: a more protected central-eastern section along 300m; and a central-western active zone (about 412m) which is more exposed to marine forces (Figure 1).

Figure 1: Study area, East Sussex, England



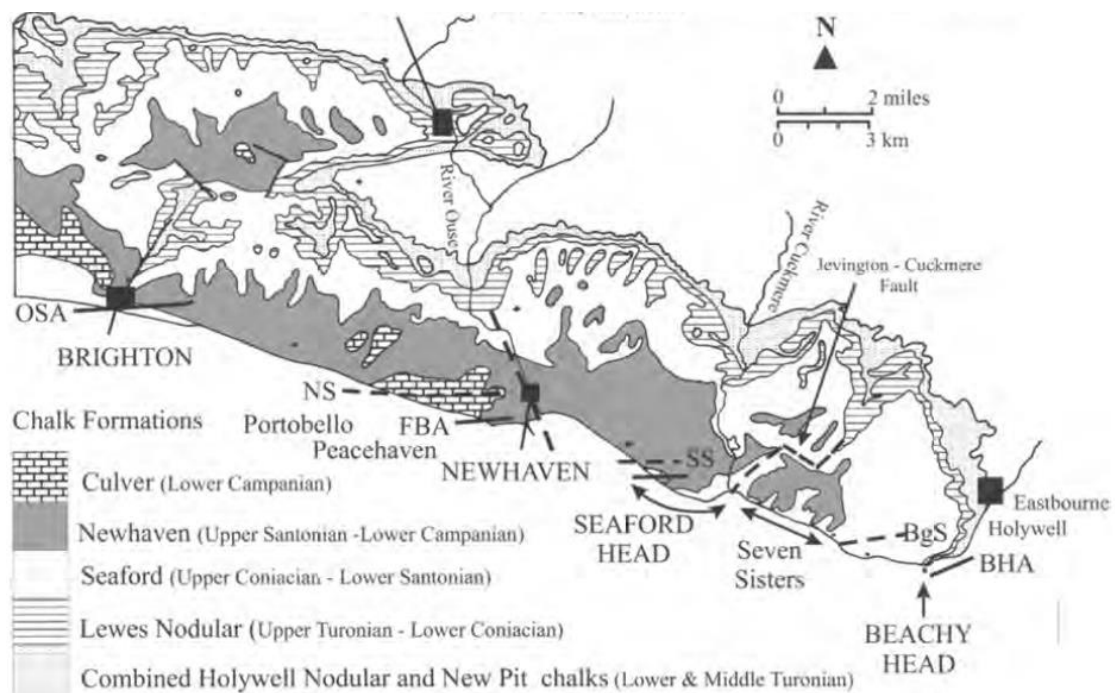
sources: Aerial Imagery courtesy of Chanel Coastal Observatory -CCO-. Frontal cliff DTM: author's creation. DV: Dry Valley.

The climate of the study site is controlled by continental European weather influences that induce cold spells during winter and humid, hot weather during summer (Met Office, 2016a). The area receives an average of 720 mm of rain annually, with the majority falling in winter months. The average of the annual days with air frost was 1.5 days between 1959 and 2005 (Met Office, 2016b). The site is macro tidal, with an average spring tidal range of 6.1 m (CCO, 2015), submerging the shore platform and permitting wave interaction with the cliff base. Wave heights measured for this coastal section average 0.64 m in summer and 1.04 m in winter (CCO, 2015). Cliff collapses are more common in winter when a combination of winter storm damage and wet weather weaken the chalk (Mortimer et al., 2004a; Brossard and Duperret, 2004).

1.3.2 Geological setting

The study site is part of the southern geological region of the UK (Figure 2). This region is characterized by the Cretaceous Chalk rim of the Weald basin shaping two of the most notable geomorphological features of southern England (Mortimore, 1997).

Figure 2: Map of chalk formations forming the Downs and cliffs of East Sussex



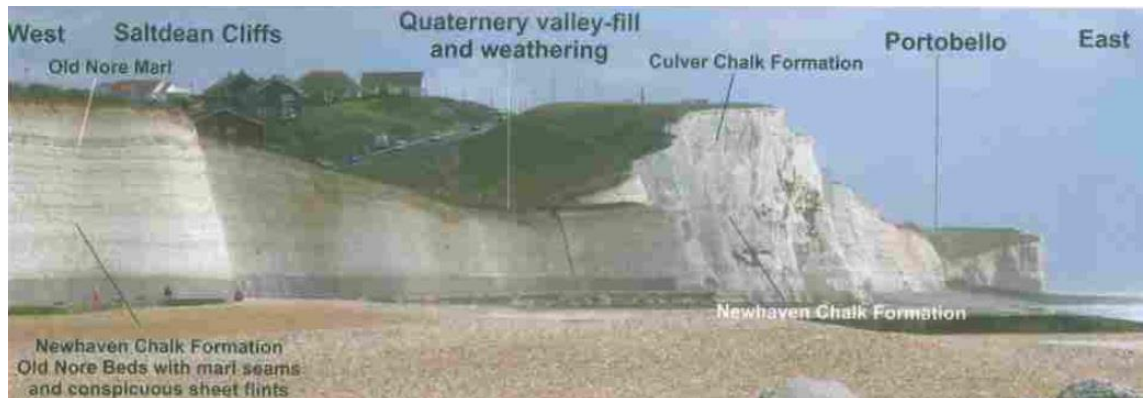
Source: Mortimore et al., 2004a.

The Late Cretaceous Chalk Group crops out largely in eastern and southern England, showing variation in strata thickness between 200 and 560 m, a product of post-

Cretaceous erosion and landform denudation. Chalk has been described as a very fine-grained calcareous limestone, but with significant variations in terms of clay content, texture, hardness, fossils and occurrence of flint (Aldiss et al., 2012; Mortimore, 2014). In addition, chalk is a fractured rock with types of fracturing distinctive to each formation (Mortimore, 2014). Regional and local differences in chalk lithofacies and lithostratigraphy as well as their geomorphological expressions have been attributed to various factors, such as tectonic settings, eustatic, climatic and tephrogenic pulses, as well as local history of erosion and weathering (Mortimore, 1997; Aldiss et al., 2012).

The modern Chalk group lithostratigraphy separates the southern England chalk into nine formations (Aldiss et al., 2012). In this context, the cliffs at Telscombe are composed principally of the Newhaven Chalk Formation with an overlying cap of the Culver Chalk on the highest hills (Figure 3). Both form part of the White Chalk Subgroup (Mortimore, 2014), and between Brighton and the study area, they dip gently to the south (Stravou et al., 2011).

Figure 3: Telscombe Cliffs formed of Newhaven Chalk, locally capped by Culver Chalk



Oblique view of the study site cliffs, showing the Newhaven Chalk capped by the Culver Chalk on the highest summits. In the photograph, the study area is located between the Quaternary valley-fill and Portobello. Source: Mortimore, 2014.

Between the cliffs of Brighton and Newhaven, which include the study site, the outcrop and structure of the Newhaven Chalk is characterised by gentle tectonic folds. These are the Friars Bay Anticline, Old Steine Anticline and the Newhaven Syncline, whose spatial distributions are shown in Figure 2. These tectonic folds exert an influence on the dip direction of the chalk and up to a point control the styles and scales of cliff collapses (Mortimore et al., 2004a; Stravou et al., 2011). The lithological characteristics of the Newhaven and Culver chalks and their properties related to cliff stability are described in Section 2.3.

2. LITERATURE REVIEW

2.1 DIGITAL PHOTOGRAMMETRY

This section reviews and summarizes the scientific basis of digital photogrammetry, which is relevant to understanding the photogrammetric processing undertaken in this research.

2.1.1 Principles of photogrammetric measurement

Photogrammetry is a three-dimensional measurement science based on the geometrical properties of images (Kasser and Egels, 2003). The fundamental aim of digital photogrammetry is to obtain three-dimensional geospatial information from two-dimensional digital or digitized images. Classically, this has been accomplished through the method of photogrammetric restitution, which involves four different stages that describe the typical photogrammetric workflow (Linder, 2006):

a) Interior orientation or camera calibration: in this stage the metric characteristics of a digital camera are defined/corrected as a requirement for photogrammetric processing (Schenk, 2005). This stage is further explained below, in Section 3.2.1 and in Appendix 2.1.

b) Relative orientation: the principal aim of this stage is to restrict corresponding conjugate rays to make sure that they intersect singularly in space in order to generate a 3D stereomodel. The relative orientation of one image relating to the other is necessary to allow stereo viewing in epipolar planes (Konecny, 2014). The concepts of photogrammetric stereomodel and epipolar planes are defined below.

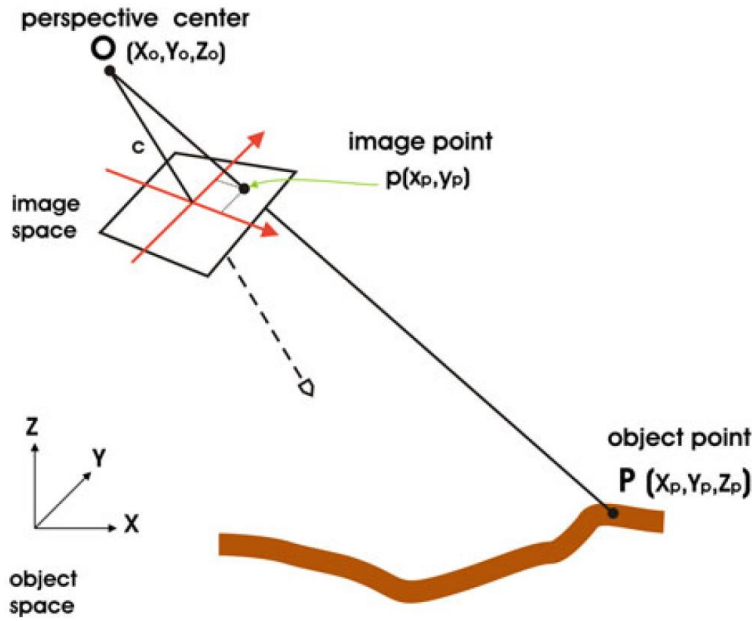
c) Absolute and exterior orientation: a 3D stereomodel created during relative orientation has an arbitrary position, rotation and scale. Here, it is defined as the transformation of the local/arbitrary coordinate system into a global/world coordinate system using ground control points (Linder, 2003).

d) Aerotriangulation / Bundle Block Adjustment: for a photogrammetric project that includes many digital images, it is required to connect/match them in one automatized and common mathematical solution. In this stage, a bundle block adjustment is used, which is a method that permits the simultaneous calculation of all unknown object space (terrain surface) coordinates, in addition to calculating the components of the interior and

exterior orientation parameters (Kasser and Egels, 2003). Bundle adjustment is further described in Sections 3.2.1 and 3.2.2.

An essential mathematical model in digital photogrammetry is the 'central perspective projection'. This model defines the spatial relationship between the object space (i.e. terrain surface) and the image space (Awange and Kiema, 2013). According to the central projection, the object point P, perspective centre O and equivalent image point p all lie on a straight line, expressed by the vector OP (Figure 4).

Figure 4: Principle of central perspective projection



Source: Awange and Kiema, 2013.

The central projection in space is described mathematically through the collinearity equations (Eq. 1.1 and 1.2) which are the fundamental equations of analytical and digital photogrammetry (Awange and Kiema, 2013). The mathematical expression follows the form (Linder, 2003; Clifford et al., 2004; Luhmann et al., 2013):

$$x_p = x' = x_p - c \frac{r_{11}(X_P - X_0) + r_{12}(Y_P - Y_0) + r_{13}(Z_P - Z_0)}{r_{31}(X_P - X_0) + r_{32}(Y_P - Y_0) + r_{33}(Z_P - Z_0)} + \Delta x' \quad (1.1)$$

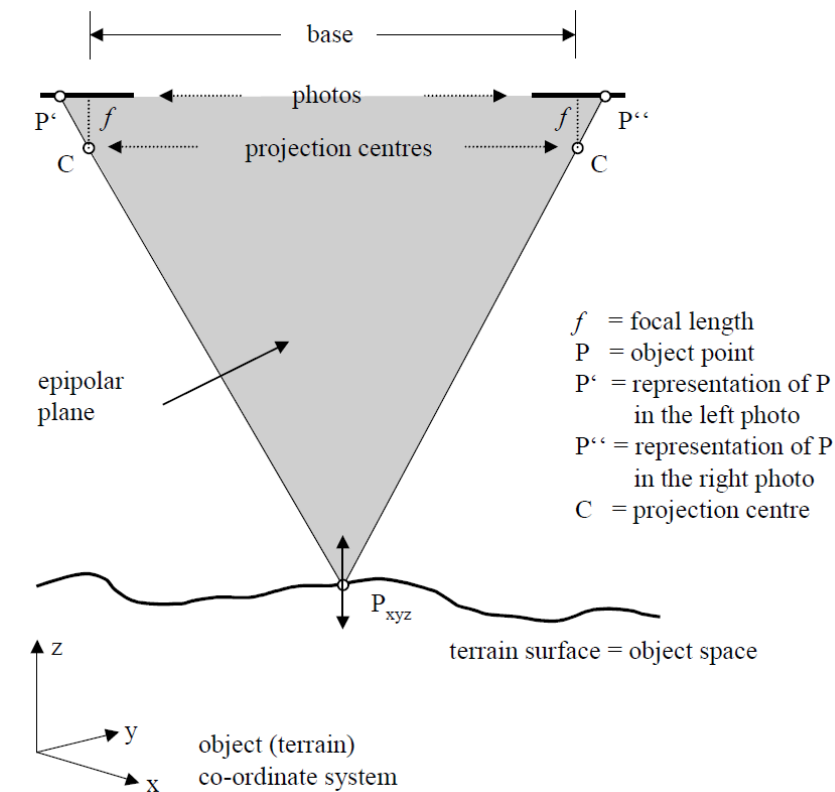
$$y_p = y' = y_p - c \frac{r_{21}(X_P - X_0) + r_{22}(Y_P - Y_0) + r_{23}(Z_P - Z_0)}{r_{31}(X_P - X_0) + r_{32}(Y_P - Y_0) + r_{33}(Z_P - Z_0)} + \Delta y' \quad (1.2)$$

Where $(x_p, y_p$ or $x', y')$ are the coordinates of the image point (p); $-c$ is the calibrated focal length; (X_0, Y_0, Z_0) indicating the coordinates of the perspective centre (O), and (X_P, Y_P, Z_P) are the coordinates of the object point (P); r_{ij} for $i, j = 1, 2, 3$ representing

the components of an orthogonal rotation matrix (R) including the three angles (ω, φ, κ). Within this formula, the five parameters $x_P, y_P, -c, \Delta x, \Delta y$, indicate the elements of the interior orientation. They determine the spatial location of the camera's perspective centre, the principal distance and the position of the principal point (Luhmann et al., 2016). The interior orientation components are defined in Appendix 2.1. The six parameters ($X_0, Y_0, Z_0, \omega, \varphi, \kappa$) represent the elements of the exterior orientation, which determine the camera orientation and location in a global object coordinate system (Schenk, 2005). The components of the rotation matrix (ω, φ, κ) are discussed below (section 1.2).

The location and shape of an object space are modelled by reconstructing bundles of rays. All image rays can be established in three-dimensional object space on the assumption that the geometrical properties within the camera and the position of the imaging system in object space are known (Luhmann et al., 2013). Beginning with the intersection of a minimum of two homologous and spatially distanced image rays, it is possible to locate an object point in three dimensions. While in stereo photogrammetry at least two images are utilized to accomplish this (Figure 5), in multi-image photogrammetry the set of images that can be used is unlimited (Luhmann et al., 2013).

Figure 5: Geometry in an oriented stereo pair model



Source: Linder, 2006.

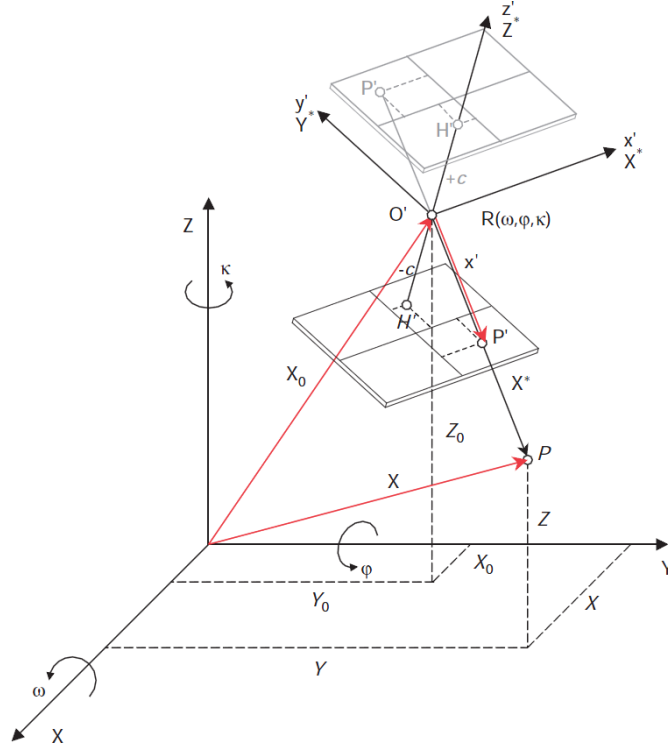
As illustrated in Figure 5, which represents the standard geometrical configuration in stereo photogrammetry (i.e. uses two or more images of the same object but taken from different camera locations), by setting up the equations of the rays ($P' \rightarrow P$) and ($P'' \rightarrow P$) calculating their intersection, it is plausible to determine the pixel three-dimensional coordinates (x, y, z) of the object point P in the left and the right image using the Eqs. 1.1 and 1.2 (Linder, 2006). Furthermore, Figure 5 shows that the base b (i.e. the distance between the projection centres of neighbouring images) and the projected rays CP determine the epipolar plane, defined by the projection/perspective centre of both images and the actual location on the object space (Linder, 2003). The significance of epipolar geometry is that an image point P'' in the right image, correspondent to P' in the left image, must lie on the epipolar plane. As a result, the search space for matching homologous/corresponding points between images can be considerably decreased (Luhmann et al., 2011).

Overall, the importance of collinear equations relies on the fact that every object point is projected into a single image point, if they are not blocked by other object points. In addition, it has been demonstrated that Eqs. 1.1 and 1.2 efficiently model image creation inside a camera through the central projection geometry. Because of that, they are utilized to numerically model other key processes in digital photogrammetry, such as spatial intersections, space resection and bundle adjustment and to generate orthophotograph and stereo plotting systems (Luhmann et al., 2013).

2.1.2 Coordinate transformations between image and terrain

For photogrammetric processing, the transformation of 3D-dimensional object coordinates in 2D-dimensional image coordinates as well as from 2D-dimensional image to 3D-dimensional object coordinates is elemental (Konecny, 2014). The following methodological concepts and mathematical models are based on Kasser and Egels (2003), Konecny (2014) and Luhmann et al. (2013).

The fundamental relationship between image coordinates and local Cartesian object coordinates (Figure 6) can be specified as 3D vectors between the following points:

Figure 6: Image and object coordinate systems

Source: Luhmann et al. (2011).

Where O is the origin of the Cartesian object coordinate system (X, Y, Z) ; P , the object point with its coordinates (X, Y, Z) described by the vector X . O' represents the perspective centre with its coordinates (X_0, Y_0, Z_0) , defined by the vector X_0 (This vector also defines the spatial location of the image coordinate system). With the vector X and X_0 , the vector $O'P$ (X^*) creating a spatial triangle.

The image point P' (image vector x') can be defined by the coordinates x', y', z' . However, essential for the perspective transformation is that the origin of the image coordinate system is associated with the projection centre of the perspective centre (O').

In addition, the image coordinate system requires a transformation using an orthogonal rotation matrix (R) which expresses the angular orientation in space and the change of system coordinates from the object space O, X, Y, Z to the image space O', x', y', z' (i.e. a combination of three independent rotations ω, ϕ, κ to the coordinates X, Y, Z , respectively). This transformation also indicates a scaling change factor m between the object coordinates and the image measurements. Thus, the image vector x' may be transformed into object space by the rotation of the matrix R and m .

Therefore, the projection of an image point into a correspondent object point is given by:

$$X = X_0 + m.R.x' \quad (2.1)$$

With its coordinate components (Luhmann et al., 2013):

$$\begin{pmatrix} X \\ Y \\ Z \end{pmatrix} = \begin{pmatrix} X_o \\ Y_o \\ Z_o \end{pmatrix} + m \cdot \begin{pmatrix} R\omega & R\varphi & R\kappa \end{pmatrix} \cdot \begin{pmatrix} x' \\ y' \\ z' \end{pmatrix} \quad (2.2)$$

$$\begin{pmatrix} X \\ Y \\ Z \end{pmatrix} = \begin{pmatrix} X_o \\ Y_o \\ Z_o \end{pmatrix} + m \cdot \begin{pmatrix} r_{11} & r_{12} & r_{13} \\ r_{21} & r_{22} & r_{23} \\ r_{31} & r_{32} & r_{33} \end{pmatrix} \cdot \begin{pmatrix} x' \\ y' \\ z' \end{pmatrix} \quad (2.2)$$

The object coordinate system X, Y, Z is a local Cartesian coordinate system that must be associated with the geodetic coordinate system based on a reference framework for the country or region of interest. The relations between geodetic coordinates are available in specific geodetic references (Konecny, 2014).

2.1.3 Space intersection

2.1.3.1 Normal stereo model case

According to Konecny (2014) and Luhmann et al. (2011) for the normal case of an oriented stereo pair model, in which two cameras have parallel exposures looking in equal direction at right angles to the stereo base (Figures 5), object point coordinates (P) XYZ can be calculated from the relations shown in Figure 7 as follows:

Parallel to the image plane:

$$X = \frac{h}{c} \cdot x' = m \cdot x' \quad Y = \frac{h}{c} \cdot y' = m \cdot y' \quad (3.1)$$

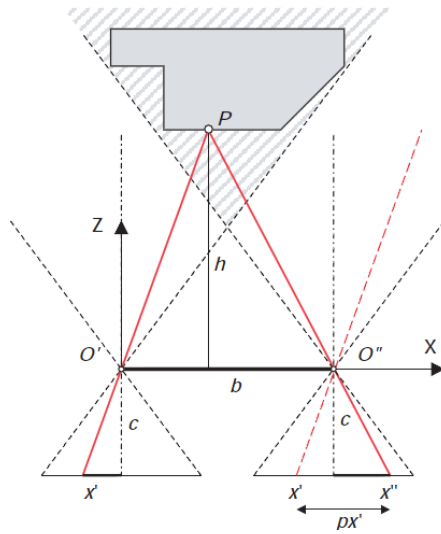
In the viewing direction:

$$m = \frac{h}{c} = \frac{b}{x' - x''} \quad (3.2)$$

and it follows that:

$$Z = h = \frac{b \cdot c}{x' - x''} = \frac{b \cdot c}{px'} \quad (3.3)$$

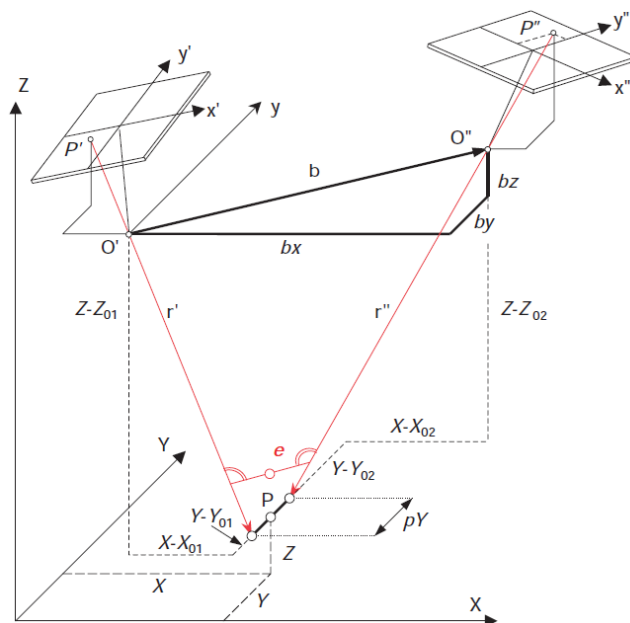
Where x' , y' and x'' , y'' image point coordinates in the left and right images respectively; h : height from object point coordinates to image plane; c : principal distance; m : image scale; b : base (distance between the projection centres of neighbouring images); and px' : horizontal parallax.

Figure 7: Normal case of stereo photogrammetry

Source: Luhmann et al. (2011).

2.1.3.2 General stereo pair case

For the calculation of spatial coordinates in the general stereo case, in which averted and convergent camera exposures are used, object coordinates XYZ can be determined by spatial intersection of the rays r' and r'' (Figure 8) if the components of interior and exterior orientation have been previously calculated. r' and r'' are calculated by the measured image coordinates, transformed by the orientation parameters (Luhmann et al., 2011).

Figure 8: Spatial intersection for the general stereo case

Source: Luhmann et al. (2011).

The space intersection can be determined as follows (Albertz and Kreiling, 1989; Luhmann et al., 2011):

a) Transformation of image coordinates in both images (i.e. setting up the equations of the rays ($P' \rightarrow P$) and ($P'' \rightarrow P$)):

$$\begin{pmatrix} X' \\ Y' \\ Z' \end{pmatrix} = \begin{pmatrix} X_{o1} \\ Y_{o1} \\ Z_{o1} \end{pmatrix} + R_1 \cdot \begin{pmatrix} x' \\ y' \\ z' \end{pmatrix} \quad \begin{pmatrix} X'' \\ Y'' \\ Z'' \end{pmatrix} = \begin{pmatrix} X_{o2} \\ Y_{o2} \\ Z_{o2} \end{pmatrix} + R_2 \cdot \begin{pmatrix} x'' \\ y'' \\ z'' \end{pmatrix} \quad (4.1)$$

b) Stereo base components:

$$\begin{aligned} bx &= X_{o2} - X_{o1} \\ by &= Y_{o2} - Y_{o1} \\ bz &= Z_{o2} - Z_{o1} \end{aligned} \quad (4.2)$$

Thus, the oblique rays intersect XY plane at elevation Z of the object point P, giving place to two possible solutions:

$$X = X_1 = X_2 ; Z = Z_1 = Z_2 ; \text{ where } Y = \frac{(Y_1 + Y_2)}{2} \quad (4.3)$$

c) The two equations with the largest coordinate differences bx and by may be utilized to solve the unknown scale factors λ and μ , which are used for the transformation of image coordinates:

$$\lambda = \frac{bx \cdot (Z'' - Z_{o2}) - bz \cdot (X'' - X_{o2})}{(X' - X_{o1}) \cdot (Z'' - Z_{o2}) - (X'' - X_{o2}) \cdot (Z' - Z_{o1})} \quad (4.4)$$

$$\mu = \frac{bx \cdot (Z' - Z_{o1}) - bz \cdot (X' - X_{o1})}{(X' - X_{o1}) \cdot (Z'' - Z_{o2}) - (X'' - X_{o2}) \cdot (Z' - Z_{o1})} \quad (4.4)$$

d) With λ and μ known, the coordinates of the intersected point P (XYZ):

$$\begin{aligned} X &= X_{o1} + \lambda \cdot (X' - X_{o1}) & Y_1 &= Y_{o1} + \lambda \cdot (Y' - Y_{o1}) \\ Z &= Z_{o1} + \lambda \cdot (Z' - Z_{o1}) & Y_2 &= Y_{o2} + \mu \cdot (Y'' - Y_{o2}) \\ Y &= \frac{(Y_1 + Y_2)}{2} & \text{Y-parallax: } pY &= Y_2 - Y_1 \end{aligned} \quad (4.5)$$

For the case of images with relative orientations, the corresponding 3D point P is chosen to be the mid-point of the closest and equidistant point e between r' and r'' . In addition, pY gives a quality estimator of the 3D relative location (Paparoditis and Dissard, 2002).

2.1.3.3 Multi-image processing

In this case, the spatial intersection deals with image coordinates taken from multiple images, along with their known internal and external orientation parameters in order to determine the spatial point coordinates XYZ (Luhmann et al., 2011). Here, the standard mathematical model is based on Eqs. 1.1. and 1.2, which are utilized as observation equations in a least-squares bundle adjustment as follow (Schenk, 2005; Luhmann et al (2011):

$$x'_i + vx'_i = F(X_{0j}, Y_{0j}, Z_{0j}, \omega_j, \varphi_j, \kappa_j, x'_{0\kappa}, c_\kappa, \Delta x'_\kappa, X_i, Y_i, Z_i) \quad (5.1)$$

$$y'_i + vy'_i = F(X_{0j}, Y_{0j}, Z_{0j}, \omega_j, \varphi_j, \kappa_j, y'_{0\kappa}, c_\kappa, \Delta y'_\kappa, X_i, Y_i, Z_i) \quad (5.2)$$

Where i : index of 3D object coordinates for each new point.

j : exterior orientation of each image. Where X_0, Y_0, Z_0 : spatial location of image coordinate system from the perspective centre O' ; ω, φ, κ : orthogonal rotation matrix (R). κ : interior orientation of each camera. Where x'_0, y'_0 : coordinates of the principal point H' ; c : Principal distance; $\Delta x', \Delta y'$: correction values for errors in the image plane. X_i, Y_i, Z_i are three unknowns. To calculate these, a minimum of three observations (image coordinates) are needed.

2.1.4 Image matching

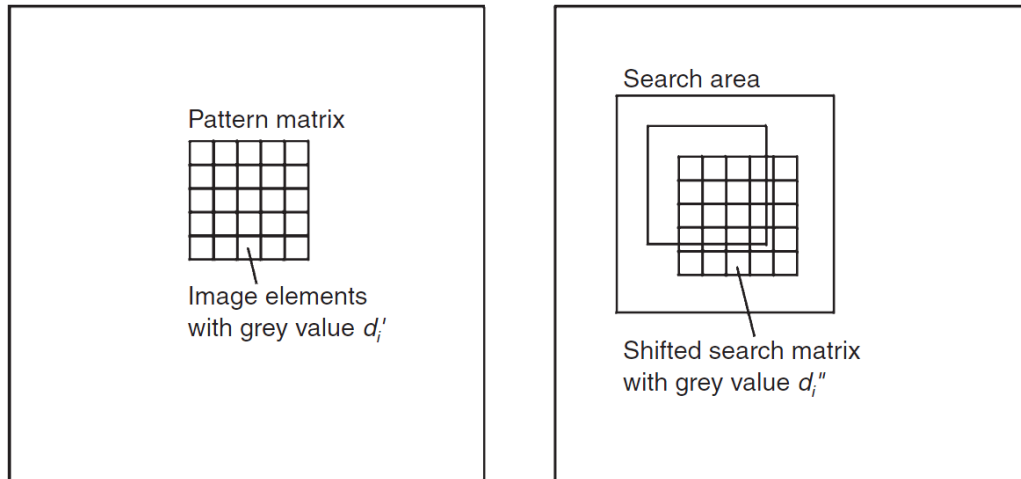
This is the central process around which automation has revolutionized digital photogrammetry. Image-matching processes are utilized to automatically determine identical object features (points, patterns, edges) in two or multiple stereo images (Awange and Kiema, 2013). Two fundamental image-matching processes can be distinguished:

2.1.4.1 Area-based matching

In this procedure a search pattern is defined for the feature to be matched through the comparison of the cross correlation coefficient between the images to be matched. Here, a pattern matrix of a restricted size of one image with grey values d'_j is compared with a similar sized matrix of a second image with grey values d''_i . This pattern is moved over a search window in the second image, with the goal of determining pixels with similar digital composition (Figure 9). The outcome is a matrix of cross correlation coefficients and their largest value is the x and y shift of the best match. It is considered that a

successful match has been obtained if the maximum coefficient is greater than 0.7 (Vosselman et al., 2004). Specific procedures for calculations can be found in Konecny (2014) and (Vosselman et al., 2004).

Figure 9: Cross correlation coefficients for area-based matching



The left and right images represent the image pattern and the search window, respectively. Source: Konecny (2014).

2.1.4.2 Feature-based matching

Area-based matching algorithms can be sensitive to variations in perspective between different images and in changes of illumination. Matching imagery at a feature scale instead of using grey values is often more robust (Vosselman et al., 2004). This method is based on the detection and classification of image features that have distinct grey value characteristics, either collectively or individually (Awange and Kiema, 2013), such as discontinuous features (e.g. rivers, roads). Feature-based matching uses interest operators. Interest operators are mathematical models used for the extraction of distinct image points that are possibly appropriate candidates for image-to-image matching. Appropriate candidates for corresponding points are pixel value image patterns (i.e. features) which, as far as possible are unique in a constrained region and likely to have a similar aspect in the corresponding image. For each pixel, interest operators define one or more parameters to calculate an interest value that can be utilized for posterior feature matching (Vosselman et al., 2004). Specific criteria for selecting candidate features and the calculus related to different interest operators (Drescher, Deriche, Förstner) can be found in Vosselman et al., (2004).

2.2 ROCK SLOPE DISCONTINUITIES AND KINEMATIC ANALYSIS

The term ‘discontinuities’ refers to natural planes of separation (breaks) in rock masses, effectively having zero tensile strength. They have no specific or generic connotations (Selby, 1993). The importance of discontinuities to the study of slope stability is that they form surfaces of weakness within the much stronger, intact mass of rock. Consequently, slope failures tend to take place preferentially along these planes (Hoek and Bray, 1981). This is because they cause concentration of stress, control the movement of groundwater within the rock mass, and allow weathering to penetrate and weaken the rock body (Selby, 1993). The most common types of discontinuities are joints, faults, bedding planes, foliation, cleavage, schistosity and fracture (ISRM, 1978; Hack, 2009).

2.2.1 Mechanisms of formation of discontinuities

Hillslopes created on rocks are practically never formed under conditions in which the intact strength of the rock is the principal control of the resistance of the rock to failure. It is the strength along discontinuities which influences the evolution of the hillslopes (Terzaghi, 1962). The material forming intact rocks has been subjected in most cases to millions of years of mechanical, thermal and chemical processes and its related stress states (Hudson and Harrison, 2000). The normal stresses acting along discontinuities are generated by the weight of the overburden (Selby, 1993). During this process, a rock mass may also be prone to faulting and folding. These mechanisms frequently result in the stresses within the rock exceeding its strength several times, causing the rock to fracture and creates joints and faults (Wyllie and Mah, 2004).

Based on Davis and Reynolds (1996) and Wyllie and Mah (2004), Figure 10 illustrates the development of joints during burial-uplift processes, which is controlled by the rock strength in comparison to the applied stress. The vertical stress, which represents the major principal stress σ_1 , is equal to the weight of the overlying mass of rock, which is described by:

$$\sigma_1 = \gamma H \quad (6.1)$$

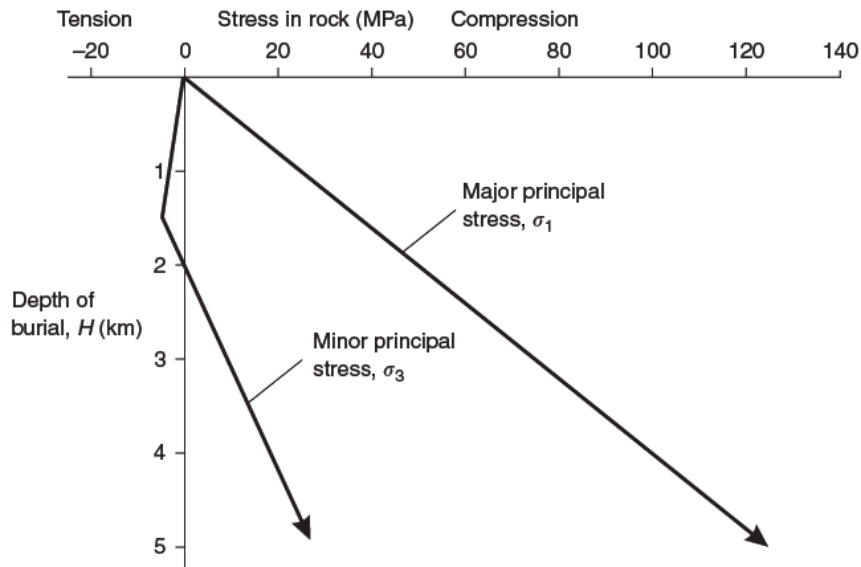
Where: γ represents the unit of weight of rock (kN/m^3) and H is the depth of burial. In addition, the horizontal stress, which is the minor principal stress σ_3 , also rises with the

depth of the burial because of the effect of the Poisson' Ratio μ , and any temperature increment that takes places. In exemplary conditions, σ_3 is associated with σ_1 as follows:

$$\sigma_3 = \left(\frac{\mu}{1-\mu} \sigma_1 \right) + \left(\frac{E}{1-\mu} \varepsilon \Delta T \right) \quad (6.2)$$

Where: E represents the modulus of deformation of the rock; ε is the coefficient of thermal expansion; ΔT represents the increment in the temperature. The left component of Eq. (6.2) indicates the value of the horizontal stress due to gravitational loading. In Figure 10, the value of σ_1 is determined by Eq. (6.1), and the value of σ_3 changes with depth as follows: The stress of σ_3 is tensile at depths less than 1.5 km where the sediments have not been consolidated into rock, and below this depth, σ_3 rises as determined by Eq. (6.2), assuming that there is no water, thermal or tectonic pressures acting on the rock mass.

Figure 10: Formation of joints due to burial and uplift of a rock mass



Source: Adapted by While and Mah (2004), from Davis and Reynolds (1996).

Further, according to Selby (1993), an unjointed rock mass will be stable against failure under the compressive overburden load as long as that load does not overcome the strength of the rock (σ_c). In a condition for failure, $\sigma_c = \sigma_1$. Thereby, the critical depth or height (H_c) for failure is given by:

$$H_c = \sigma_c / \gamma \quad (6.3)$$

According to Aydan and Kawamoto (1990) and Selby (1993), the most relevant mechanisms or processes which are responsible for discontinuity creation are discontinuities caused by tensile stresses, shear stresses, during sedimentation and metamorphism.

In the specific case of the chalk, the types of primary discontinuities are sedimentary-tectonically controlled in origin and are not produced by weathering. However, if chalk has been subjected to cold-climate Quaternary glacial and periglacial weathering mechanisms, as in Northwest Europe, the fracture frequency increments towards the ground surface (Mortimore, 2014). In this sense, it has been considered that the nature of the discontinuities in chalk are principally driven by three factors: a) past tectonic activity that caused the palaeostress events/phases that fractured the rock body; b) the lithology of the intact rock that controls how the rock responds to applied tectonic stresses; and c) the extent of post tectonic processes such as weathering (Mott MacDonald, 2005).

Such post tectonic weathering is mainly related to periglacial processes that have produced both fracturing and chemical weakening of the chalk as a consequence of freeze-thaw cycles in saturated ground, alternating seasonally between permafrost and melting during the cold periods of the Quaternary (Lautridou et al., 1986). In addition, early fractures in the chalk developed as sliding displacements occurred along local décollement horizons, comprising marl seams and slump beds. Further, inclined conjugate joints formed part of the network that resulted from these bed-sliding movements (Mortimore, 2014).

2.2.2 Properties of discontinuities relative to the slope instability

While the orientation of discontinuities has been considered to be the principal geological/geometric factor influencing rock slope stability and so used to perform stereographic kinematic stability analysis, other parameters such as persistence, spacing, roughness and infilling are important as well (Selby, 1993). Based on ISRM (1978) and Hudson and Harrison (2000), the principal properties or parameters of the discontinuities controlling slope stability are defined. These properties are illustrated in Figure 11.

1) *Orientation*: attitude of a discontinuity. This is described as the dip and dip direction or dip azimuth of the discontinuity plane. Dip is the maximum angle that a discontinuity or a slope face forms with a horizontal plane (ψ). Dip direction is the direction of the horizontal trace of the line of dip, measured clock side from north (α). An example of standard notation for orientation is dip / dip direction ($025^\circ/75^\circ$). A complementary method of measuring the direction of a discontinuity is the strike, which is defined as the

geographical direction of a line created by the intersection of a plane and the horizontal reference plane.

2) *Spacing*: Perpendicular distance between adjacent discontinuities. Usually it refers to the mean spacing of a set of joints. Categories of spacing range from extremely wide (>2m) to very narrow (<6 mm). The more closely spaced discontinuities are the weaker the rock body, therefore the opportunity for water pressures and weathering to weaken the rock mass is greater. This property is important as it provides a measure of the size and shape of rock blocks prone to slide.

3) *Persistence*: Discontinuity trace length observed in an exposure. Categories of persistence range from very high (>20 m) to very low (<1 m). This property may give a crude measure of the extent or penetration length of a discontinuity. Furthermore, together with spacing, this parameter is useful to estimate the size of the blocks and the length of potential sliding planes.

4) *Roughness*: Intrinsic surface roughness and waviness of the surface of a discontinuity. The degrees of roughness and waviness contribute to the shear strength, particularly where the discontinuity is undisplaced and interlocked. The degree of roughness may be estimated either by reference of standard charts or mathematically.

5) *Wall strength*: Equivalent compressive strength of the adjacent rock surface of discontinuity. This property may be lower than the rock block strength due to weathering and alteration of the walls. Wall strength may be defined either by referring to standard charts using a geological hammer, or by applying Schmidt hammer tests.

6) *Aperture*: Perpendicular separation between adjacent rock walls of a discontinuity, in which the intervening space is water or air filled. Aperture is relevant to mass strength since it controls the frictional strength along a discontinuity as well as the flow of water and the rate of weathering of a wall of rock. Usually, classes of aperture range from cavernous (>1 m), to very tight (<0.1 mm).

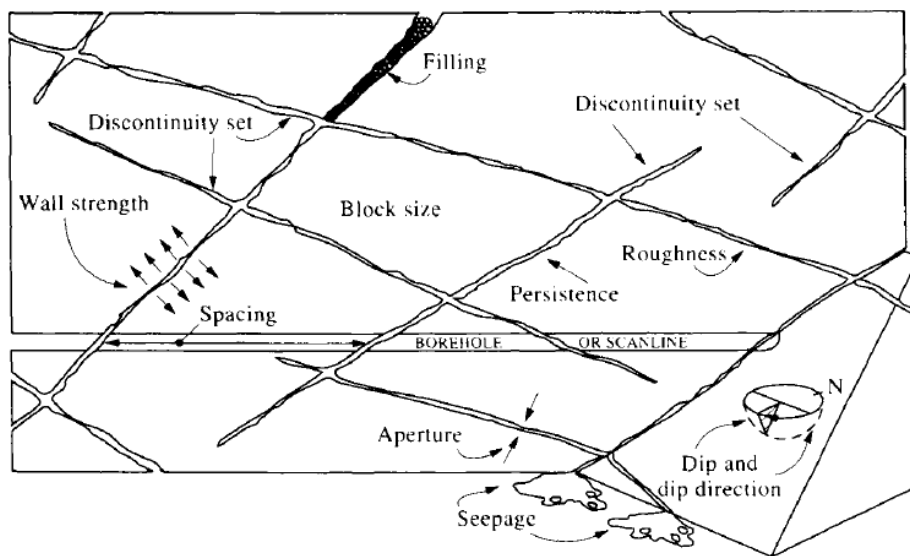
7) *Filling*: Material that separates the adjacent rock walls of a discontinuity and that is commonly weaker than the parent rock. Common filling materials are sands, silt, clay, breccia, gouge, mylonite.

8) *Seepage*: water flow and free moisture observable in individual discontinuities or in the rock body as a whole. Pore water in joint filling materials and in the pores of intact rock contributes to weathering and solution, and reduces cohesive and frictional strength.

9) *Number of Sets*: The number of discontinuity sets that intersect one another. This property will have an effect on the extent to which the rock body can deform without failure of the intact rock. As the number of sets increases and the rock block size decreases, the greater the opportunity for blocks to translate, rotate and crush under applied loads.

10) *Block size*: rock block dimension and shape resulting from the mutual orientation of intersecting discontinuity sets, and resulting from the spacing and persistence of the individual sets. Block shapes comprise blocky, tabular, shattered and columnar.

Figure 11: Geometrical properties of discontinuities controlling slope stability



Source: Hudson and Harrison (2000).

2.2.3 Kinematic analysis

Kinematic analysis determines which modes of slope failure (planar, wedge, toppling) are possible in a jointed rock mass. Angular associations between the orientation of the discontinuities and slope faces are analysed to examine the potential for and mechanisms of failure (Kliche, 1999). Kinematic analysis involves mapping the orientations of penetrative discontinuities within a rock slope in order to identify those that are oriented unfavourably for slope stability given the shear strength along the discontinuity surfaces (Richards et al., 1978).

However, kinematic analysis is based solely on the geometric conditions of rock slopes, that is, it does not locate the discontinuity in space, or give specific references to their size, or considers the influence of ground water circulation on slope stability, and internal

strength due to the cohesion (Lara and Sepulveda, 2008). For these reasons, even in if a kinematic analysis indicates failure, this does necessary mean that failure will take place (Rocscience, 2016b). Hence, the common rock mechanical design procedure is to utilize kinematic analysis to assess possible unstable rock blocks, followed by a detailed stability analysis based on the calculation of the factor of safety (Hoek and Bray, 1981).

The structural geometrical conditions related to rock slopes that generate block slide failures and the specific stereonet techniques used to recognize them are shown in the chapter Methodology (Section, 3.4).

2.2.4 Stereographic analysis of discontinuity data


The assessment of the orientation of structural geology data implies plotting poles which indicate the dip and dip direction of discontinuities. This is executed with the aim of identifying clusters or sets of discontinuities, for which average dip and dip direction can be determined. The following procedure is to plot great circles showing the average orientation of each set, principal discontinuities of interest, and dip/dip direction of the slope face (Hoek and Bray, 1981).

2.3 GEOLOGY, GEOMORPHOLOGY AND CLIFF STABILITY AT THE STUDY SITE

2.3.1 Stratigraphy

Stratigraphic characteristics of chalk have been demonstrated to have an important control on its engineering properties, specifically the intact dry density, weathering and style of fracturing, and cliff morphology (Mott MacDonald, 2005). The stratigraphic characteristics of the Newhaven and Culver Chalk formations can be seen in Figure 12.

Figure 12: Chalk stratigraphy of Newhaven and Culver Chalk formations



Age	Formation	Beds	Marker Horizons	Approximate Thickness (m)	
Lower Campanian	Culver Chalk	Spetisbury and Tarrant Members (Undifferentiated)	Castle Hill Flints	Culver Chalk is up to 10m thick in Cliffs at Friars Bay	
			Castle Hill Marls		
	Newhaven Chalk	Bastion Steps	Telscombe Marls	10.0	
		Meeching	Meeching Marl	8.0	
		Peacehaven	Peacehaven Marl	5	
Upper Santonian		Old Nore	Old Nore Marl	26	
		Splash Point	Brighton Marl	13.5	
			Buckle Marls		

Sources: Geological column extracted from Mott MacDonald (2005) after Mortimore (1997). Approximate thickness for the coastal section between Brighton and Newhaven from Mott MacDonald (2005).

The lithological characteristics, members and boundaries of both Newhaven and Culver Chalk formations (Fm) are described below according to Mortimore (1986) and Mortimore (2014).

2.3.1.1 Newhaven Chalk Formation

1) *Lithological description*: constituted of soft to medium-hard, blocky smooth white chalk with regular marl seams and numerous flint bands. The formation is known to include distinct phosphatic chalks of limited lateral extent.

2) *Age range*: Santonian Age (KS) – Campanian Age (KC).

3) *Lower and Upper boundary*: the key lower boundary marker is at the base of Buckle Marl 1 in the Sussex succession, which indicates the end of the upper Seaford Chalk, that is, the change from chalk with tens of metres with no marl seams and much flint (Seaford Formation) to marly chalk with various marl seams and regular, but fewer bands of flint (Newhaven Formation). This change is usually recognised by the appearance of a distinct assemblage of bioclastic debris, and coincides with a negative break of slope, which has been assumed to mark one or more persistent marl seams. The Newhaven Formation has five members: Splash Point, Old Nore, Peacehaven, Meeching and Bastion Steps. The internal markers are Brighton Marl, Old Nore Marl, Peacehaven Marl and Meeching Marls, respectively. Splash Point and Old Nore have less flint than those above. In contrast, there are numerous flint bands in the Peacehaven Member. The upper boundary is located at the top of Castle Hill Marl 2, which indicates the beginning of Culver Chalk Formation. The Newhaven Formation has a thickness of 45 to 75m, and is limited by sub-Palaeogene erosion over large areas of southern England.

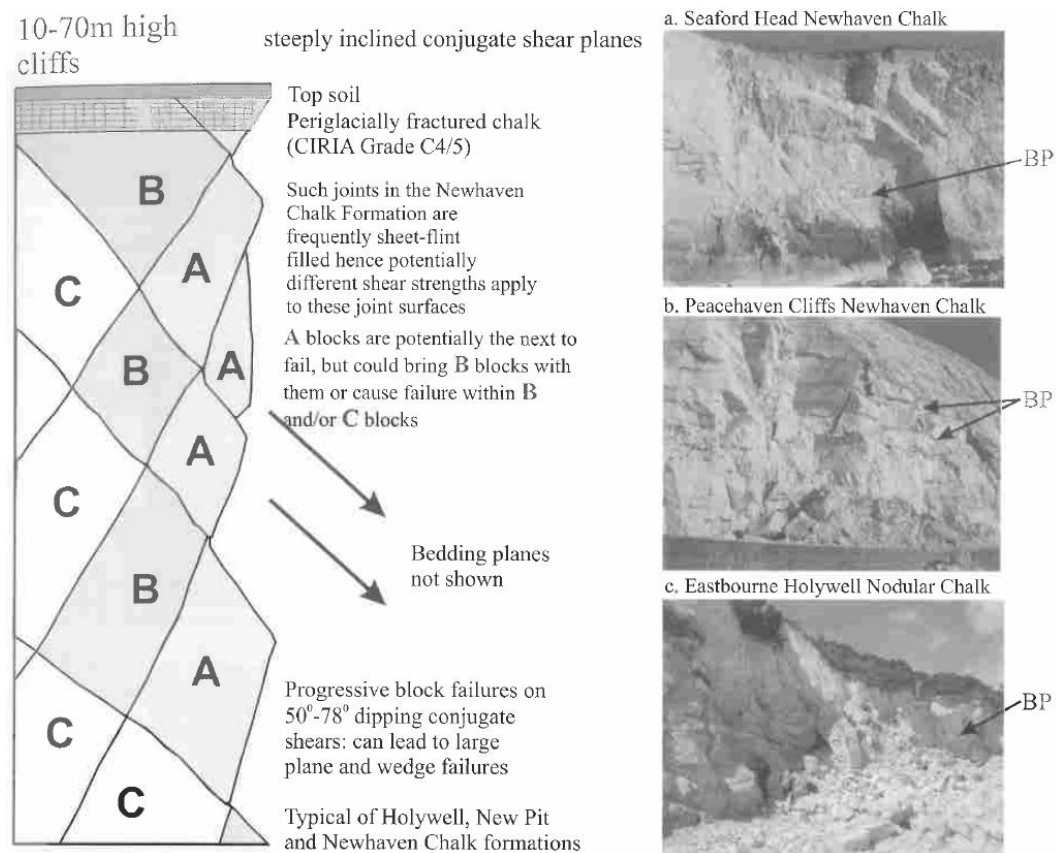
4) *Engineering properties and cliff instability*: this formation has a remarkable structural feature characterized by persistent steeply inclined conjugate shear joint sets, small faults and fractures, commonly slickensided and frequently containing sheet flints (Mortimore et al., 2004a). In addition, the Newhaven Chalk has more sheet flint on both sub-horizontal and sub-vertical fractures than any other chalk formation. Furthermore, sub-horizontal sheet flints have a significant effect on groundwater flow and the related inclined conjugate shears influence the rock mass mechanical properties (Mortimore, 2014). In this sense, layers of flint that infill inclined conjugate pairs of fractures and sets of fractures parallel to the bedding planes complement the characteristics of the Newhaven Chalk fracture style (Mott MacDonald, 2005).

These styles of discontinuities produce typical cliff failures of Newhaven Chalk, characterized by plane, wedge and progressive block failures on 50-78° dipping conjugate shears surfaces. These failures have been defined as 'Peacehaven type' by Mortimore et al. (2004a) (Figure 13). Slides across fracture surfaces that have increasingly lost shear strength due to weathering processes are also common (Mortimore et al., 2004a).

Although the Newhaven Chalk has been described as homogeneous white chalk, between sequences of marl seams there are beds of medium and high density, and locally very high density, hence low porosity blocks of chalk (Mortimore, 2014). Moreover,

according to Lord et al, (2002) and Mott MacDonald (2005), flints are a conspicuous feature of chalks created by very hard brittle siliceous material, so that represent beds of contrasting strength and character compared with the usually much weaker chalk. Hence, numerous modes of failure are seen to be driven by the presence of flint bands whether as fracture-fills or bedding layers. Flint strength may, therefore, be a significant component of some cliff failures (Mortimore et al., 2004b). Flints are commonly extremely strong, with strengths well in excess of 200MNm^{-2} , although strengths in excess of 600MNm^{-2} are not uncommon (Lord et al., 2002; Mott MacDonald, 2005).

Figure 13: Newhaven to Brighton cliffs. The Peacehaven type of failures



Source: Mortimore et al., 2004a.

Intact dry density (IDD) and degree of saturation (natural moisture content/NMC) are critical factors for assessing cliff instability (Mortimore et al., 2004b). Table 1 summarises the Newhaven Chalk beds IDD, NMC and Undrained Triaxial (UT) strength behaviour (saturated and dry):

Table 1: Summary of physical properties of the Newhaven Chalk

Member	IDD (Mg/m ³)	NMC (%)	Definition	Results of UT tests
Old Nore Beds	1.55 - 1.8	18 - 26	Very soft to medium-hard Chalk	Old Nore, Peacehaven and Meeching members, in dry samples tested at 2000, 4000 and 6000 kN/m ² elastic properties were dominant. Those tested at 8000 and 10000 kN/m ² showed very slow initial stress increment, followed by a sudden increase in stress and then by ductile failure. Most samples failed by formation of conjugate failure planes associated with some crushing. In the Splash Point member, stress strain curves for samples tested at low confining pressure exhibited low ductility. Samples tested at 2000 and 4000 kN/m ² had linear stress strain curves. Samples tested at 6000, 8000 and 10000 kN/m ² showed an initial curve, suggesting porosity collapse. Failure planes followed marl seams structures.
Meeching Beds	1.6 – 1.8	18 - 24	Soft to medium-hard Chalk	

Source: Mortimore et al., 2004b.

Based on the analysis of index properties of density, natural moisture content and porosity tests, Mortimore et al. (2004b) concluded that there are several influences of porosity differences on cliff instability. Soft, high-porosity chalk, which is the case of some samples obtained from the Newhaven Formation, can lose and gain water quickly. Thus, they are prone to cause changes in the physical conditions in cliffs more readily than higher-density chalk. As a consequence, cycles of wetting and drying associated with the weather will cause cyclic changes in bulk density and hence cyclic loading in the cliff. This process, combined with expansion and contraction cycles, not only produces the loss of the rock mass but also concentrates stress at specific points, making these cliff lines highly unstable. The uniaxial compressive strength of the chalk at specific stress concentration points, in combination with rock mass discontinuity patterns, will partially define the modes and scales of slope failures.

2.3.1.2 Culver Chalk Formation

1) *Lithological description*: Homogeneous and soft fine-grained white chalk, relatively marl free, with some very strongly developed nodular, horn and semi-tabular flint.

2) *Age range*: Campanian Age (KC) – Campanian Age (KC).

3) *Lower and upper boundary*: the key lower boundary marker is conformable, and located at the base of Castle Hill Marls, which indicates the end of the upper Newhaven Chalk Formation. Thus, it marks the change from firm white chalk with common marl seams (Newhaven Formation) to soft white chalk with no or few marl seams (Culver Formation). The Culver Chalk has two members; the Tarrant Chalk Member and the Spetisbury Member. The upper boundary is comfortable as well, and located at the

Portsmouth Marl, which is the base of the overlying Portsmouth Chalk Fm. This boundary indicates the change from very soft white chalk with large potstone flint to white chalk with grey marl seams and nodular flint bands (Portsmouth Formation). The thickness of this unit has a range of 65 to 75m.

4) *Engineering properties and cliff instability*: In this chalk formation, the fracture type changes from dominantly inclined conjugate joints and shears (Newhaven Chalk) to regular sets of sub vertical and vertical joints with a general absence of sheet flints (Mortimore, 2014). Seaford and Culver Chalk formations are characterized by being very-soft and low-density chalk (high porosity) with predominantly clean, vertical joint sets, more closely spaced than in the other formations. Consequently, Mortimore et al. (2004b) concluded that the weakest Chalk materials are found in these two formations. The aforementioned rock-mass character has a marked impact on the failure mechanisms, that is, simple vertical collapses, type 1a according to Mortimore et al. (2004a), in which failures involve the gradual opening of the tension cracks sub-parallel to the cliff face. The load of the collapsing stack overcomes the shear strength of the remaining chalk attached to joint surface at some point down the tension crack. Commonly, the collapse surface extends vertically down to the cliff toe, shaping a vertical slab. In addition, joints perpendicular to the cliff face or faults control the lateral boundaries of the failures.

Table 2, summarises the Culver Chalk IDD, NMC and UT strength behaviour conditions (saturated and dry):

Table 2: Summary of physical properties of the Culver Chalk

Member/site	IDD (Mg/m ³)	NMC (%)	Definition	Results of UT tests
Downend Portsmouth	1.5 – 2.1	10 - 30	Extremely soft to very-hard Chalk	Ductile failure took place at high confining pressure (4000kN/m ²). A sample tested at 10000kN/m ² failed at very low stress and showed an initial curve indicating that porosity failure is a significant factor, which corresponds with the soft (low-density) character of this Chalk.
Cotes Bottom, Lambley's Lane, Charmandean	1.45 – 1.6	- - -	Extremely soft to soft Chalk	Further, most of the failure planes followed pre-existing fabrics, such as marly wisps and burrow structures.

Source: Mortimore et al., 2004b.

2.3.2 Geomorphological and environmental processes

Chalk cliffs at East Sussex retreat as a consequence of wave abrasion and undercutting, but are also influenced by solution, bioerosion and rock falls due to freeze-thaw processes and groundwater discharge (Bird, 2004). According to Robinson and Williams (1983), cliff erosion between Brighton and Eastbourne is produced by the synergic action of rain, frost and salt, and the frequent pounding of the sea at the foot of the cliffs. It is concentrated in the winter months, especially during thaws following severe frosts, and during storms, when wave attacks are more intense and the chalk above is saturated and heavy. Furthermore, the cliffs are especially vulnerable after dry summers when vertical fissures develop behind the cliff base. In addition, cliff retreat is intermittent as short stretches of cliff collapse and the debris accumulates on the beach, temporarily protecting the foot of the cliffs from wave action.

The opening of joint-guided fissures within the chalk has a key influence on cliff instability. This is produced due to: a) cracking and joint widening occurring in dry weather, followed by an increase in pore water pressure of cracks and joints; b) increase in weight of the chalk through water absorption occurring during wet weather; c) freeze-thaw events cause shattering and disintegration of the chalk surface; and d) weathering and breakdown by salt crystallization resulting from periodic cycles of wetting and drying by sea spray. These have been considered as possible factors that may trigger chalk cliff failure processes (Robinson and Williams, 1983; Robinson and Jerwood, 1987a,b).

Relative rates of erosion by marine or subaerial processes, in addition to the position of more resistant strata exert a control on the general convexity or concavity of sea cliff profiles. Concave, steep or undercut cliffs as at Telscombe cliffs tend to be developed in marine-dominated environments and convex profiles where subaerial processes dominate (Emery and Kuhn, 1982).

Even when the role of the different factors and processes that control cliff retreat are put into perspective, Dornbusch (2015) concluded that in cliffs exposed to marine action, waves have a key environmental role in cliff retreat of the chalk coasts of the English Channel through their influence on: a) abrasion at the base in combination with beach and shore platforms materials; b) creating impact pressures into set of joints; and c) removing any debris protection at the cliff's bottom.

Overall, the stability of chalk cliffs is controlled at the same time by both subaerial and marine processes, as well as geomorphological and geological settings, which control

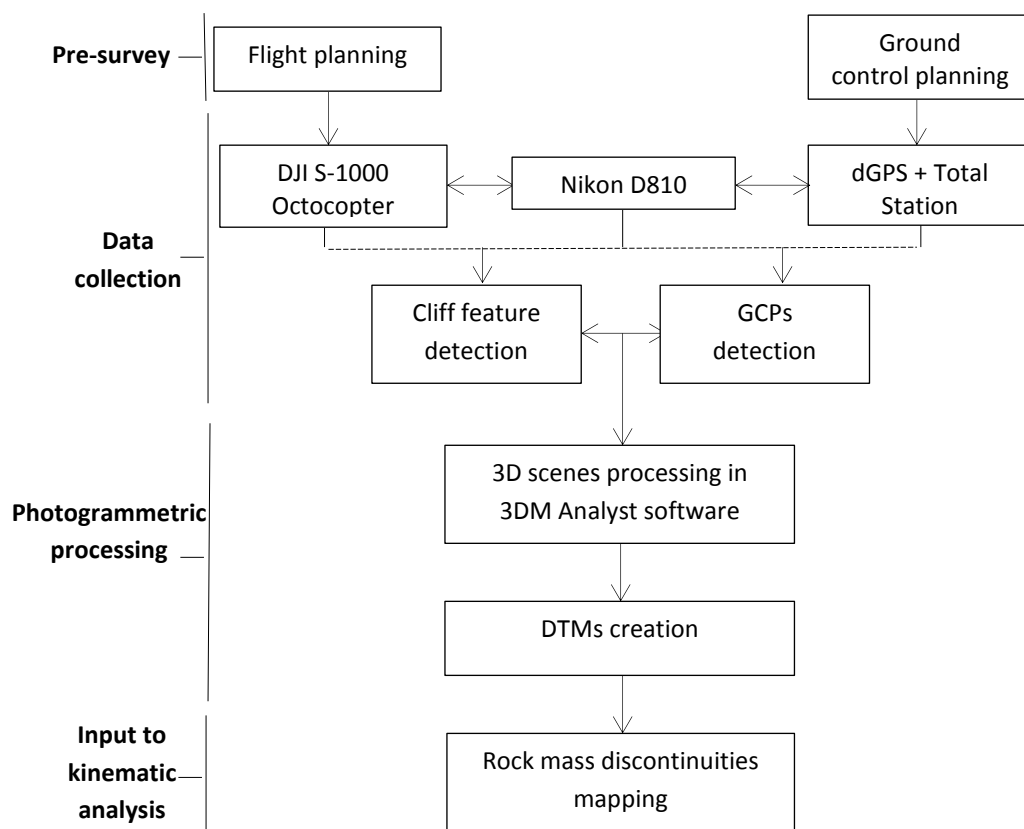
the mechanical behaviour of the rock (lithology, structure, fracture pattern). The morphodynamic conditions of the cliff, from stability to failure, depend on variations that take place in the rock mass, for instance the development and opening of fractures, which also depend on the strength of the rock mass which control the deterioration rate as a consequence of the infiltration of water. These internal changes are produced by external forces of meteorological/environmental origins (e.g. frost, drying), softening and stress relief at the cliff face and by forces of marine origin (e.g. wave action, tidal conditions, the presence or absence of deposits at the cliff base, vertical erosion of the shore platform) (Duperret et al., 2002; Brossard and Duperret, 2004; Duperret et al., 2005).

3. METHODOLOGY

3.1 DATA COLLECTION

Geomorphological feature detection of Telscombe cliffs has been accomplished using UAV photogrammetry to map rock mass discontinuities and extract information about their dip, dip direction and exposed persistence. These data were used to perform a kinematic analysis of slope stability. The overall technique for data collection involved installation of a Nikon D810 digital camera on board an octocopter. Ground control for the survey used a combination of dGPS and total station surveying to produce a network of ground control points (GCPs) on the cliff face and shore platform. Linking GCPs and a bundle adjustment numerical method, the digital photogrammetry image processing was undertaken in 3DM Analyst Mine Mapping Suite software (Figure 14).

Figure 14: General methodological workflow

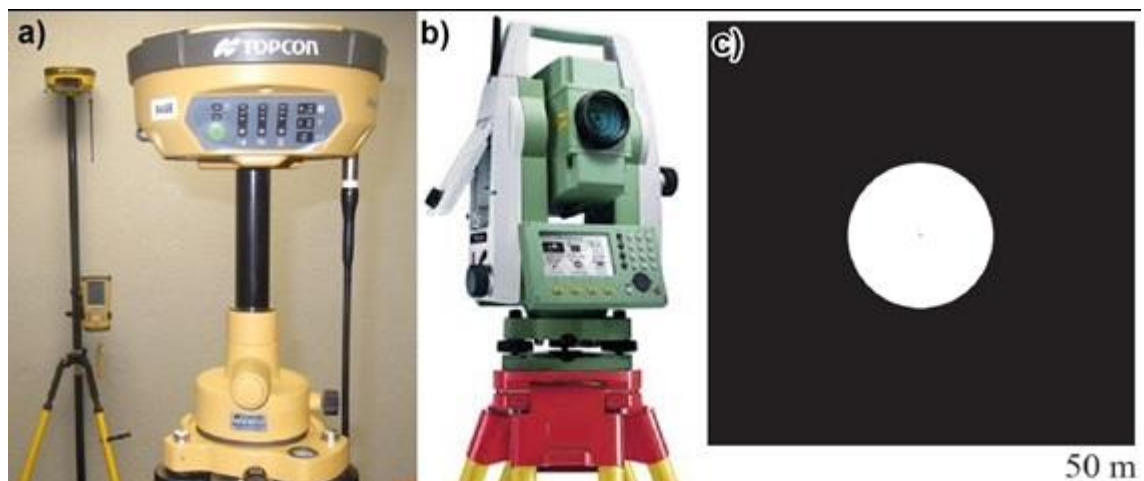


3.1.1 Topographic survey

The topographic survey was accomplished using the technique of differential GPS (dGPS) and total station surveying, which were fundamental for the acquisition of coordinates for the photogrammetric processing, since these supplied GCPs for the DTM's absolute orientation.

The master GPS's receiver (Figure 15a) was installed on a coordinate known point (base station location), which was located 17 m back from the cliff top of the study area. Using post processing kinematic (PPK) operation mode, a transportable second receiver (rover) was used to collect five coordinates on the cliff top and four coordinates on the shore platform with a logging rate of 20 Hz and an occupation time of 20 seconds. The distance between the coordinates on the top was from 105 to 190 m, providing a regular spatial distribution. The coordinates obtained on the shore platform were used to set and orientate the total station (Figure 15b).

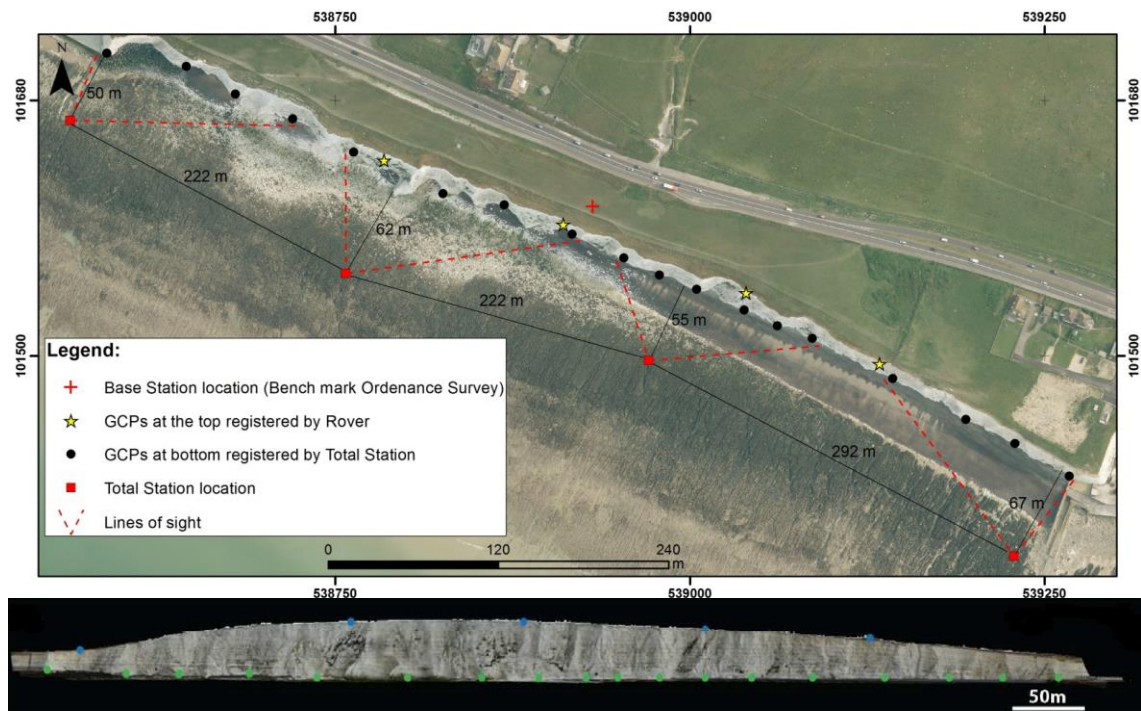
Figure 15: Equipment and targets used for the topographic survey



a) dGPS model: Topcon HiPER II dGPS Receiver with Master's GPS receiver at the front and Rover at back. b) Total Station model: Leica FlexLine TS09. c) Circular targets.

The coordinates obtained with dGPS were then corrected in the Topcon Tools v.8 software by post-processing procedures, which are discussed by Awange (2012) and Awange and Kiema (2013). The acquired values of coordinates position dilution of precision (PDOP), which are used as an expression of the quality (i.e. accuracy) of the satellite geometry at the moment of the survey, were between 1.2 and 1.5, thus suitable to determine the DTM's absolute orientation since according to Awange and Kiema (2013) PDOP values of less than 2 are indicative of good satellite geometry for computing a position.

Figure 16: Topographic survey map and view of the cliff face with GCPs



Source: Aerial imagery courtesy of Channel Coastal Observatory – CCO. Blue points: 5 GCPs installed on the top. Green points: 18 GCPs installed at the cliff base.

In complex terrain morphologies (i.e. high-hillslope) poor sky satellite visibility above the horizon can severely compromise the accuracy of a computed position (Young, 2012). Therefore, a Leica FlexLine total station (Figure 15b) was used to register coordinates at the cliff bottom. Cylindrical prisms (Leica GMP-111) were located in reachable and flat surfaces at the cliff base to provide an equidistant spatial distribution of coordinates (18 points). The total station was installed on four locations on the shore platform since the accuracy for computing coordinates decreases with distance from the base (Young, 2012) and to avoid occlusion within the line-of-sight created by concavities and convexities of the cliff base. The distance between each station was from 222 and 292 m, and between 50 and 67 m to the cliff face. With this spatial distribution, between four and six coordinates were registered within each line-of-sight (Figure 16).

On the points with the registered coordinates, ground control survey markers (circular targets) with a white circle on a black background were installed (Figure 15c). The contrast between the black background and the white circle permit the automatic registration of the images to within 1/10 of a pixel. The size of the markers was determined based on the distance between the cliff face and the camera, and the desired pixel size (ADAM Technology, 2010).

3.1.2 Unmanned aerial vehicle for photogrammetric survey

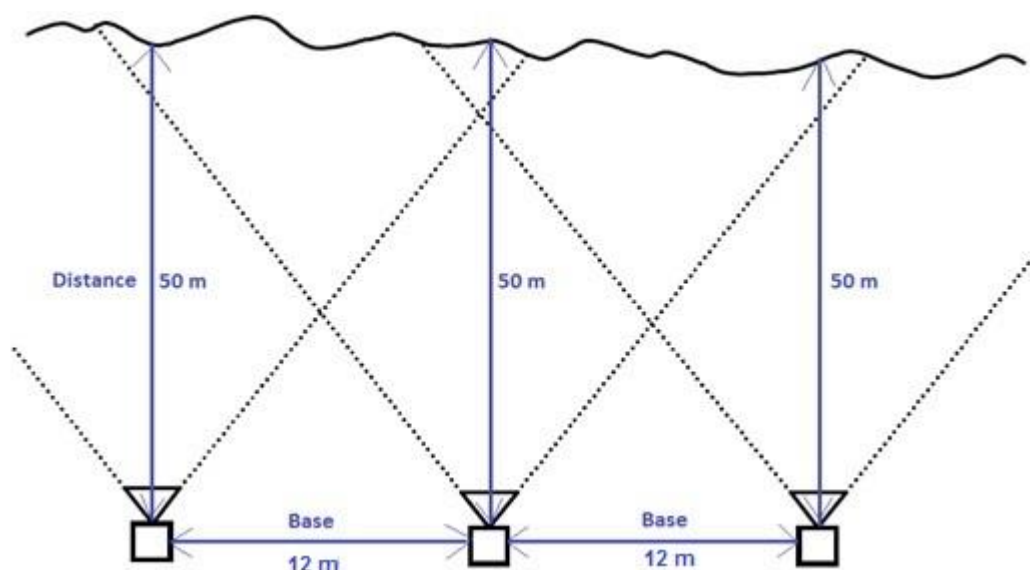
3.1.2.1 Photogrammetric project design and flight plan

Planning a photogrammetric rock cut survey should be based on three fundamental principles (Sturzenegger and Stead, 2009a):

- Definition of the area to be mapped taking into account physical constraints.
- Specification of the accuracy and precision required for mapping.
- Specification of required resolution (i.e. ground pixel size).

Due to the morphological characteristics of Telscombe cliffs, namely, a length of about 750 m and a maximum altitude of 49 m (giving an estimated hillslope area to be covered of 32,000 m²), a strip survey was selected as the technique for image acquisition in order to encompass the entire cliff length (Figure 17). In this method, sequences of parallel and not oblique images facing towards the object with large overlap (commonly 60%) are acquired (ADAM technology, 2010). The essential advantage of strips is that the large degree of overlap among images permits orientation information to be reliably and accurately passed between models, decreasing the number of ground control points needed for a given job without losing accuracy. Furthermore, this technique is best utilized for mapping a long stretch of a rock cut from a short distance and a short focal length (Birch, 2006). Hence, suitable for Telscombe's project design.

Figure 17: Strip of models with actual distance and base used for the project design



Source: Adapted from Birch (2006).

In order to obtain wider ground coverage in each image in addition to a low flight height, a short focal length (24 mm) was used. These are suitable settings for geo-engineering mapping purposes: on the one hand, shorter focal lengths (e.g. $f = 20 - 50$ mm) permit capture of the whole rock cut utilizing a practical number of images (Sturzenegger and Stead, 2009a); on the other, a low flight height contributes to increasing the resolution since it has a direct influence on the accuracy and image scale (Hussain and Bethel, 2004). Consequently, to ensure that the entire cliff height is detected, an object distance of 50 m (i.e. between the aircraft and the cliff face) was chosen by flying the UAV at approximately mid cliff height of 22 m. This photogrammetric design resulted in one flight path needed to cover the study site.

Images were set to automated capture at a time interval of three seconds, with the UAV flying at a constant speed of 3.7 m/s^{-1} , resulting in an image capture of about 12 m following a strip plan (i.e. base, Figure 17). This resulted in 70 images captured for photogrammetric processing with a horizontal overlap of around 70%, and a ground coverage per image of 74.8×50 m. Total flight time for the survey was 7.2 minutes.

Related to the required resolution to accomplish the second objective of this research, which is mapping rock slope discontinuities, a fine scale (cm) resolution permits mapping of stratigraphical contacts, meso-scale tectonic and sedimentary structures, or weathering and other surface processes (McCaffrey et al., 2005). Moreover, close-range digital photogrammetry (CRDP) allows the characterization of sub-vertical slopes if a fine (cm) to very fine (mm) resolution is obtained (Sturzenegger and Stead, 2009b). Therefore, a ground pixel size of $10 \text{ mm} \times 10 \text{ mm}$, together with an expected image accuracy of 0.5 pixels were selected to accomplish the geotechnical mapping. Such a level of detail makes it possible to measure and map low to extremely high persistence of discontinuities (ISRM, 1978; Sturzenegger and Stead, 2009a,b). In addition, 0.5 Pixels of image accuracy is considered as a good conservative value for engineering photogrammetric planning (Birch, 2006).

3.1.2.2 UAV survey

The UAV survey was accomplished on 27/05/2016. The aircraft used for data capture was a DJI S-1000 octocopter, which is a small multi-rotor-wing platform. Its principal characteristics are summarized in Table 3 and Figure 18.

Table 3: DJI S1000 octocopter characteristics

UAV model	DJI S-1000 octocopter
Maximum take-off weight	10.89 kg
Maximum operation wind conditions	10 m/s
Maximum operating altitude	1000 m
Maximum flight time	30'
Motors and type	8 motors, model 4114-11, manufactured by DJI-innovations
Batteries	Lithium polymer
Flight modes	Manual or GPS aided navigation
Advantages	Vertical take-off and landing, more stable in the air compared to other UAV systems, secure against system crashes, due to the redundancy of multiple motors. Flexible camera orientation and rotation: downward, forward and oblique.
Disadvantages	Short flight time, low capacity to carry larger payload.

Advantages and disadvantages taken from Eisenbeiss, 2009.

Figure 18: DJI S1000 octocopter and Nikon D810 FX DSLR camera

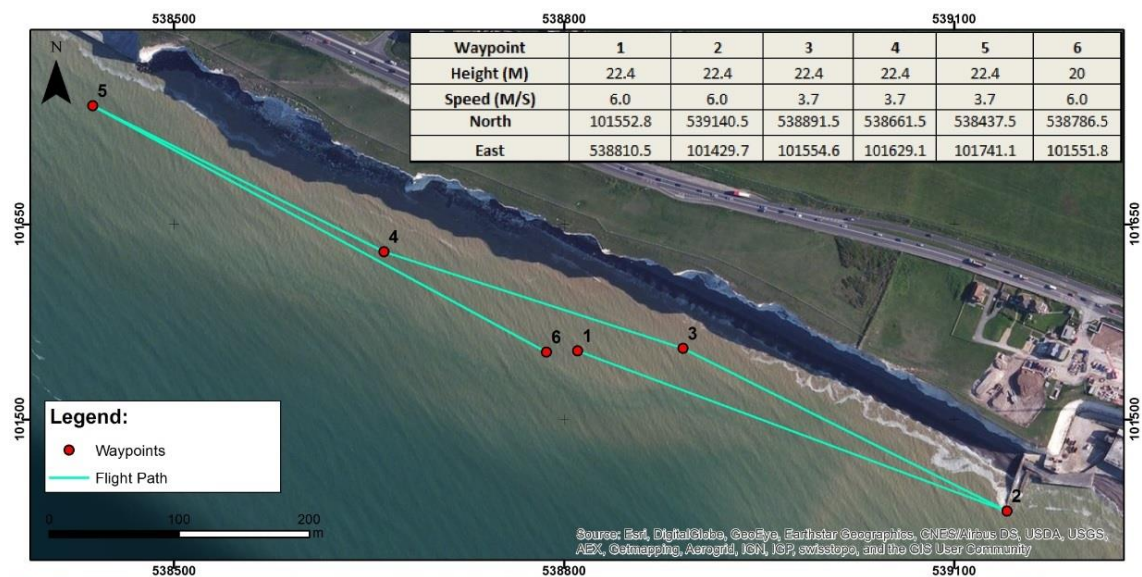


Prior to the survey a flight file was created, which included information to drive the UAV in an automatic flight mode from a laptop running a flight monitoring software. This file contained information about six waypoints to be followed, their coordinates, height and flight speeds, which together defined the flight path (Figure 19).

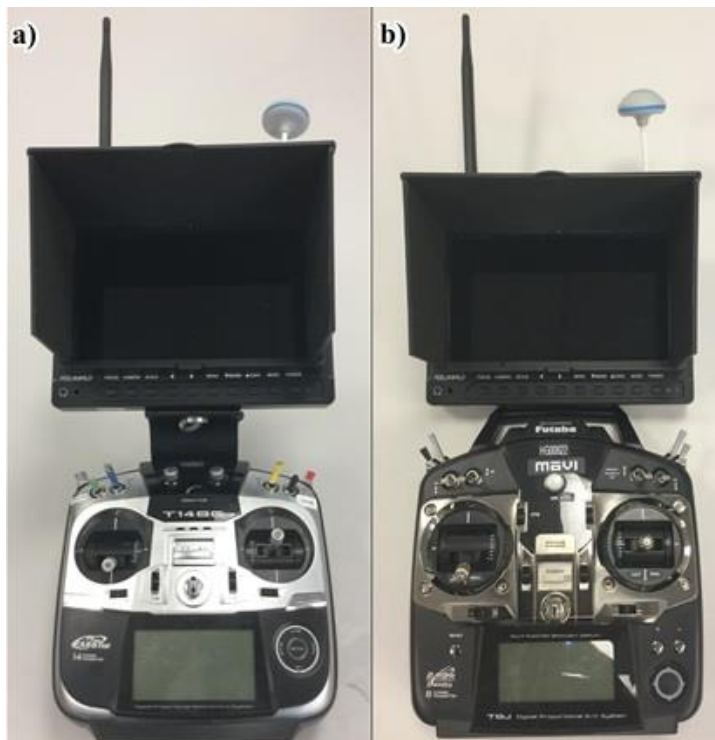
The survey was carried out by installing a Nikon D810 FX DSLR 36 mega-pixel digital camera on a Movi M5 gimbal platform. After take-off, using the Movi M5 gimbal the camera orientation was maintained orthogonal to the cliff face and directed at the mid-cliff height through live stream video from another camera installed on the UAV.

After the manual take-off from the shore platform, the UAV flew automatically for the total duration of the mission, taking images at the pre-configured time interval and coming back to the take-off place on completion of the mission. During this stage, the UAV was continually monitored from the ground station. The take-off was executed using the aircraft's remote control (Figure 20a), while the camera orientation was controlled using the gimbal remote control (Figure 20b).

Figure 19: UAV flight path



Source: Aerial imagery courtesy of Esri, DigitalGlobe, GeoEye. The strip plan was defined between waypoints two and five. Waypoints one and six represent the sites of take-off and landing, respectively.

Figure 20: UAV remote controls and its screens

a) Aircraft's control; b) Gimbal's control

3.1.2.3 Camera properties and settings

The camera's principal characteristics and settings were optimised for lighting conditions and aircraft flight speed as follows (Table 4):

Table 4: Nikon D810 properties and settings used for capturing scenes

Camera type	Nikon D810 FX Digital Single-Lens Reflex
Lens mount	Nikon F mount
Number of pixels (maximum)	7360 x 4912
Image sensor dimensions	35.9 x 24 mm
Pixel size in CCD array	4.88 x 4.89 μm
Focal length	24 mm
Aperture	f/8
ISO / shutter speed	1250 / 0.002 (1/500)
Depth of field	6.43 m - infinity
Hyperfocal distance	7.4 m

The light-transmitting capacity of a lens is commonly known as aperture. It is set via f/number , which is defined as the focal length f of the lens divided by the diameter d of

the entrance pupil ($N = f/d$) for infinity focus (Ray, 2000a). Smaller apertures increase the depth of field, and thus help to keep objects in focus. The recommended range is $f/5.6$ to $f/11$, with $f/8$ normally being the most convenient setting for photogrammetric purposes (ADAM technology, 2010).

The sensitivity of the sensor (the ISO speed) is determined by the camera type and characteristics. Together with the aperture, ISO speed has a direct influence in the image's luminance. Selection of an appropriate combination depends of the specific scene and lighting conditions (Bilissi et al., 2010). An ISO speed of 1250 was selected in order to increase the luminance of the scenes, since this was reduced due to the presence of clouds at the time of the UAV survey. Also, a very high shutter speed was used.

Parameters that must be taken into account for the calibration of the camera and capturing the scene during the UAV survey are depth of field and hyperfocal distance, since they have the role of maintaining the scenes in a sharp/optimum or acceptable focus zone towards infinity (Ray, 2000c).

Hyperfocal distance is defined as the focus distance on which the maximum depth of field is achieved. The hyperfocal distance is principally controlled by the focal length chosen during the photogrammetric flight planning, the aperture utilized and the camera model (Ray, 2000b). Depth of field is defined as the distance in front of and behind of the focus point that appears clearly in a photograph (Allen, 2010). For a given aperture, the maximum depth of field is extended from half of the defined hyperfocal distance value to infinity (Ray, 2000b).

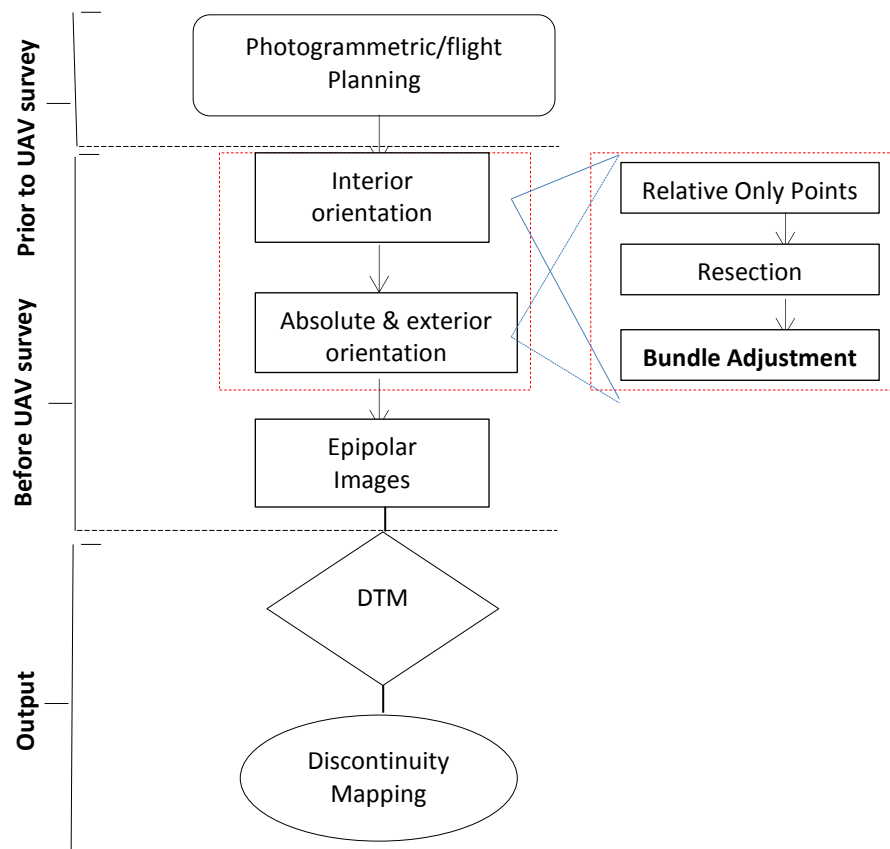
Consequently, by selecting a Nikon D810 digital camera, a focal length of 24 mm, a minimum circle of confusion of 2 pixels (that controls the blurriness at a given depth of field), and a standard aperture of $f/8$, an hyperfocal distance of 7.4 m and a depth of field of 6.43 m to the infinity were used. These parameters were obtained using an object distance calculation spreadsheet (ODCS) provided by ADAM technology (Appendix 1).

3.2 PHOTOGRAMMETRIC PROCESSING

The digital image processing was undertaken in the software 3DM Analyst Mine Mapping Suite, which is a digital photogrammetric system provided by ADAM technology, that uses a bundle adjustment numerical method as the axiomatic mathematical model to perform the interior, exterior, relative and absolute orientation of its photogrammetric products.

The interior orientation (inner or camera calibration) was executed in the software 3DM Calib Cam, while the creation of digital terrain models (DTMs) was executed using DTM Generator. Both software packages were designed to be utilized with 3DM Analyst as part of its program package. Exterior and absolute orientations, and discontinuity mapping were performed in 3DM Analyst. The following sections present the standard mathematical models that were executed during the principal stages of the photogrammetric processing (Figure 21).

Figure 21: Photogrammetric workflow executed in 3DM Analyst Mine Mapping Suit



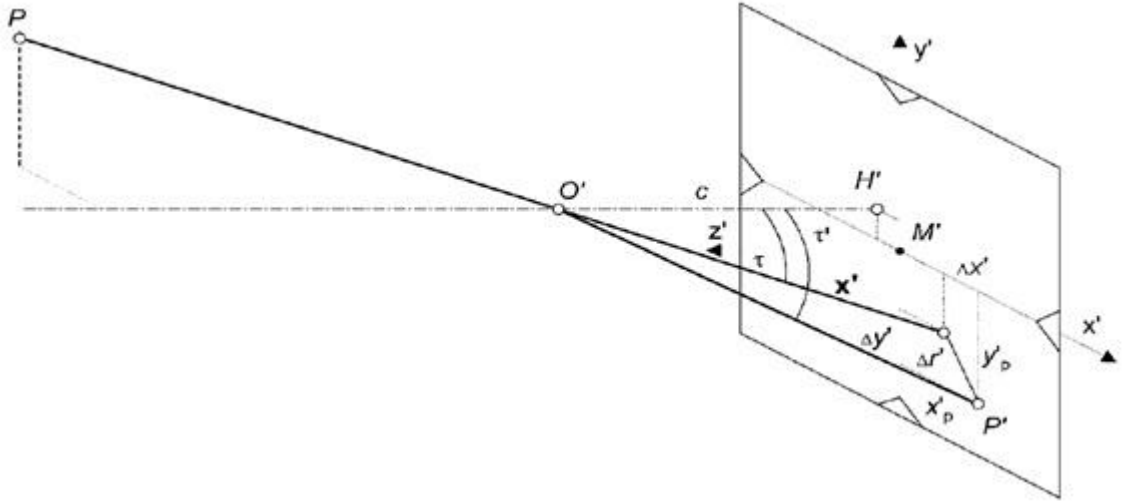
Source: modified from 3DM ADAM technology, 2010. Relative Only Points creation, Resection and bundle adjustment stages (highlighted in red dash line) are automatically executed during both interior and exterior orientation.

3.2.1 Interior orientation: camera calibration

3.2.1.1 Self-calibrating bundle adjustment

The parameters of the interior orientation include: principal distance, $z' = -c$ (C), principal point offsets H' (x_p, y_p), radial distortion $\Delta r'$, decentring distortions (P1, P2), and scaling factors (B1, B2) (Luhmann, 2016). They are defined in Appendix 2.1. As shown in Figure 22, the sense and magnitude of these parameters show an indication of by how much the geometry of the image creation inside the utilized camera deviates from an exact central perspective projection. Hence, the objective of correcting the image rays inside the camera was to ensure that the line from the object space (P) crossing to the perspective centre (O') to the image space (P') forms a straight line, thus fulfilling one of the elemental principles of the collinearity conditions, as shown in Eqs. 1.1 and 1.2.

Figure 22: Schematic interior orientation and its principal parameters



Source: Luhmann et al., 2011.

Here, the fundamental mathematical model solves a 2D transformation using collinearity equations (Schenk, 2005). According to Luhmann et al. (2016) they are used as observation equations in the self-calibrating bundle adjustment (BA), which was modelled using the standard BA equation:

$$x' = x_p + -c \cdot \frac{R_{11}(X - X_0) + R_{21}(Y - Y_0) + R_{31}(Z - Z_0)}{R_{13}(X - X_0) + R_{23}(Y - Y_0) + R_{33}(Z - Z_0)} + \Delta x' \quad (7.1)$$

$$y' = y_p + -c \cdot \frac{R_{12}(X - X_0) + R_{22}(Y - Y_0) + R_{32}(Z - Z_0)}{R_{13}(X - X_0) + R_{23}(Y - Y_0) + R_{33}(Z - Z_0)} + \Delta y' \quad (7.2)$$

Where: principal distance ($-c = -z$); principal point offsets H' (x_p, y_p); parameters compensating for total correction, namely, radial and decentring distortion effects in addition to scaling factors ($\Delta x, \Delta y$); object point $P(X, Y, Z)$; projection centre $P_0(X_0, Y_0, Z_0)$; image point $P'(x', y')$; rotation matrix components (R).

3.2.1.2 Interior orientation: output report

Because of that the interior orientation should be representative of the actual scene to be measured in addition to providing enough surface texture and depth content to the image calibration process (Luhmann et al., 2013), the actual cliff face of the study site was selected as the proper surface to perform the calibration. Strip Interior orientation (i.e. using all the images captured during the UAV survey) was used to produce the camera calibration file. This was undertaken by digitizing the location of the 23 targets in all applicable images, using centroiding algorithms. Relative only points, resection and bundle adjustment were then executed. These stages are numerically described in Appendix 2. The interior orientation report is shown in the Appendix 3.

Since the pixel accuracy and the precision of the coordinates were the same for those obtained from the exterior orientation report, the parameters obtained from the interior and exterior orientations are described in the Section 4.1. Table 5 presents the correlation matrix of the interior orientation.

Table 5: Camera calibration correlation matrix

Parameter	C	X _p	Y _p	K ₁	K ₂	K ₃	P ₁	P ₂	B ₁	B ₂	Max	
C	1	0	0.01	-0.01	0	0	-0.01	0	0.09	-0.01	-0.34	Image 42 _y
X _p		1	0	0	0	0	0.03	0	0.02	0.11	0.48	Image 48 _x
Y _p			1	0	0	0	0	-0.04	-0.1	0.01	0.25	Image 37 _z
K ₁				1	-0.94	0.88	0.06	0.15	0.04	-0.01	-0.94	K ₂
K ₂					1	-0.98	-0.05	-0.04	-0.01	0.01	-0.98	K ₃
K ₃						1	0.05	0.04	0	-0.01	-0.98	K ₂
P ₁							1	0.08	-0.01	-0.16	-0.48	Image 28 _ω
P ₂								1	-0.08	-0.02	0.8	K ₁
B ₁									1	0.01	-0.77	Point 104 _z
B ₂										1	0.71	Point 104 _x

It is well known that the assessment of the camera correlation matrix is focused on the dependency and non-dependency of parameters (Honkavaara et al., 2006). Here, low correlation in this group is given between the principal distance (c), and principal point ($Y_p = 0.01$), radial distortion ($K_1 = -0.01$) and decentring distortion ($P_1 = -0.01$). Other sets

of low correlation are given between principal point, decentring distortion and scaling factors (B). Some of the parameter exhibit non-dependency among them (e.g. C and K_2 , K_3 , $P_2 = 0$) as well. According to Luhmann et al. (2013), these groups of low correlation are normal and not of concern, since higher correlation coefficients indicate linear dependency between parameters. They should be avoided particularly because the bundle adjustment solution can become numerically unstable. On the other hand, the largest correlations in this matrix is given among radial distortions parameters, ranging from -0.94 to -0.98, for which high correlations are normal (Honkavaara et al., 2006).

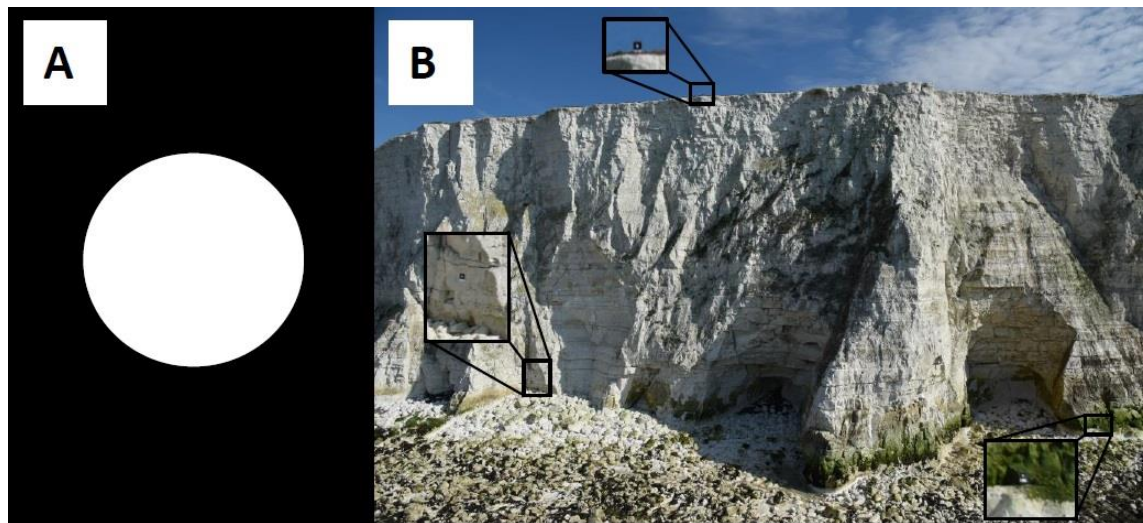
By examining the final value (pixel) table (Appendix 3), the largest deviation of any pixel from the expected location is created by radial distortion parameters K_{1-3} (418, -304 and 93 pixels, respectively). Based on the definition of this parameter, this suggest errors created by variations in refraction at each component lens within the camera's compound lens, that may be associated with the fact that no-fixed lens was used for capturing images and/or due to vibrations of the lens during the flight. Overall, these results suggest non-systematic errors of the camera performance in terms of deviations created by the camera lens to create an exact central perspective projection.

3.2.2 Absolute and exterior orientation

3.2.2.1 Digitising ground control points on Images

The ground control points obtained during the topographic survey (Figure 23) were digitized in all applicable images in order to perform an absolute orientation of the model. They were manually entered by digitizing the location of the 23 control points on the corresponding circular targets. This was accomplished using a centroiding algorithm (Appendix 2.2) that helped to locate the centre of each circular target accurately (to 0.1 of a pixel).

Figure 23: Survey target markers and example of the its placement on the cliff face

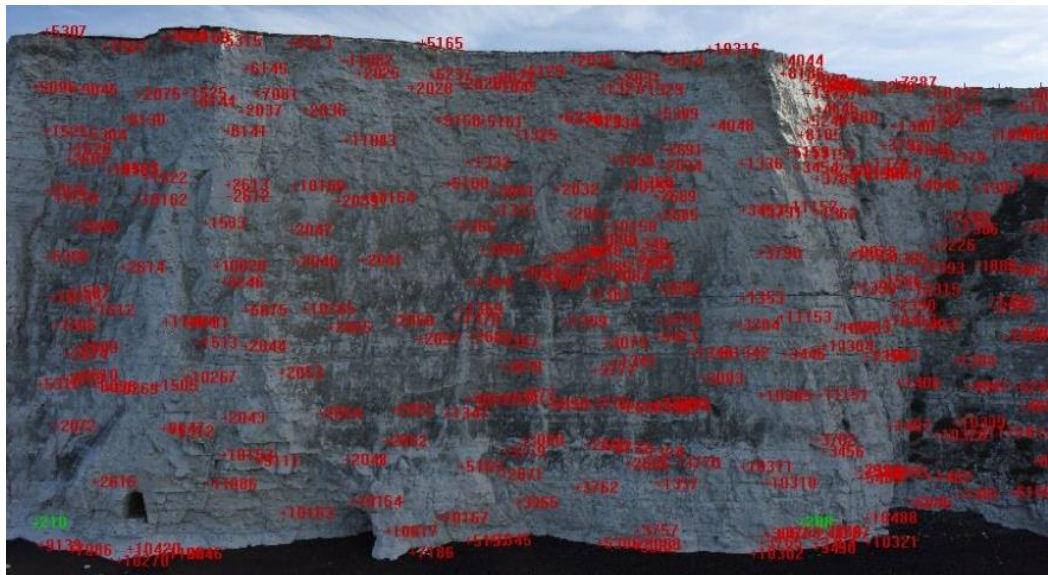


(A) Circular survey target marker. (B) Example of the target's placement on the cliff face taken from an image captured from an UAV survey (13/04/2016).

3.2.2.2 Relative only points generation

Relative only points (ROPs) are matching points with unknown 3D coordinates (Birch, 2006) which were used to connect the images used during the interior and exterior orientation stages (Figure 24). Further, they help to define the relationships between the triangulated camera positions with respect to each other within arbitrary coordinate system (i.e. relative orientation). Based on the least-square matching (LSM) method, ROPs search for matching points in each image (ADAM technology, 2004). The objective of LSM is to reduce the square sum of grey level differences between a pattern matrix of pixels (i.e. from a reference image) and a geometrically transformed matrix corresponding to a search image (Konecny, 2014). The reference image is a rectangular template window or image patch in a real image (i.e. area-based method, Section 2.1.4), which must be connected in a corresponding stereo partner image (Paparoditis and Dissard, 2002). The standard mathematical models of LSM methods are shown in Appendix 2.3.

Figure 24: Generation of ROPs during the exterior orientation process



From LSM 37,790 ROPs were obtained, with an average of 555 per image. These numbers do not consider bad ROPs, which were previously removed by setting a residual threshold greater than 0.5 pixels. Red points are ROPs. Green points are GCPs.

During the interior and exterior orientations, two techniques were applied for removing bad residuals from ROPs. The first was by manually deleting bad ROPs using 3D View and so, cleaning the model (commonly, they were found on the beach surface, buildings and sky). The second was based on the size of the residuals. In this case, there were examined images that had high residuals by examining a residual report. During this process, a threshold value of 0.5 pixels was selected. By applying this technique, the project was scanned iteratively removing only those ROPs from the aforementioned threshold (without removing digitized control points). Overall, ROPs are fundamental in the imaging matching process not only during the interior orientation but also for the exterior orientation since insufficient ROPs reduce the matching tolerance and vice versa (ADAM technology, 2006).

3.1.2.3 Image resection

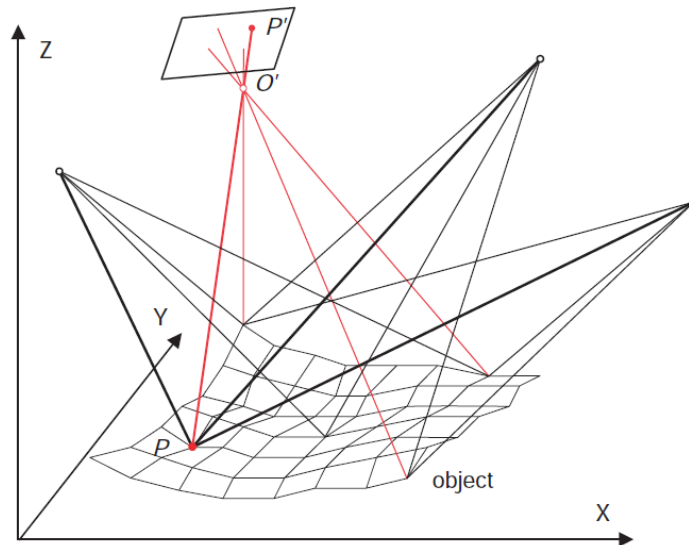
Resection is the process of calculating and deriving the initial camera exterior orientation based on image relative or absolute coordinates of object points (Linder, 2003). The bundle adjustment method is able to find the optimal solution in a least-squares context, but uniquely if it is given initial estimated values that are already approximately correct. An image resection was utilized to find that initial approximation, which is automatically and implicitly executed before each bundle adjustment performed in 3DM Analyst (Birch,

2009). In this stage, GCPs (i.e. absolute coordinates) were used to execute the image resection. The conventional numerical model of resection is shown in Appendix 2.4.

3.1.2.4 Multi-image processing by bundle adjustment

Bundle adjustment (BA) is the method for refining a visual reconstruction to generate jointly optimal 3D models and viewing parameter (camera calibration and/or location) calculations. The name refers to the bundles of light rays leaving each 3D model and converging in each camera's perspective centre O' (Figure 25), which are optimally adjusted to the object and camera location (Triggs et al. 1999).

Figure 25: Schematic multi-image triangulation using bundle adjustment



Source: Luhmann et al., 2013.

At this stage, the GCPs and ROPs created were used to orientate and merge (respectively) the 68 digital images into a global 3D model since BA uses photogrammetric measured image points, survey observations and an object coordinate system (Luhmann et al., 2013). Further, BA is directly useful for both interior and exterior orientation (Clifford et al., 2004). The standard mathematical model used during this stage of the photogrammetric processing was based on the collinearity equations, which follow the Eqs. 7.1 and 7.2 shown in the self-calibration BA of the interior orientation (Section 3.2.1.1). At this point, these equations defined within one simultaneous calculation the interior orientation parameters ($x'_0, y'_0, c, \Delta x', \Delta y'$) and exterior orientation parameters ($X_0, Y_0, Z_0, \omega, \varphi, \kappa$) of each image. To reduce the residuals of the model, several resections and then BA iterations were executed by replacing the computed

image accuracy values obtained in each previous BA. These iterations were performed until find the report with the lowest RMS residual and posteriori variance factor to build DTMs.

3.2.3 Epipolar images and DTM generation

Using the DTM generator tool, DTMs were created directly from epipolar images. These images were created based on a photogrammetric process known as epipolar resampling. Its aim is to generate epipolar stereopairs (also called normalized stereopairs), created by rectifying the original stereomates into an epipolar orientation. This technique eliminates y-parallax, while leaving x-parallax unsolved, thus it may be interpreted as differences in elevation. Further, this epipolar rectification requires rotations of one or both images so that horizontal lines of the set of images shown on the screen are epipolar lines (Agouris et al., 2004). In the process of construction of the DTMs, points are sampled from epipolar images to be automatically modeled with a certain accuracy, density and spatial distribution (Li et al., 2004). In this case, a mean spacing per point of 0.1 m was defined before running the creation of the DMTs. Figure 26 shows an example of an actual epipolar image creation obtained from the applied photogrammetric procedure.

Figure 26: Example of epipolar images of the photogrammetric processing



3.3 DISCONTINUITY MAPPING

The digital discontinuity mapping was accomplished by manually fitting planes on individual recognizable chalk surfaces or traces on digital terrain models utilizing the 3D view of 3DM Analyst Mine Mapping Suite. In the software codes, discontinuities are represented as a circle, the size of which is dependent upon the size of the surface being digitized. In addition, dip and dip direction are derived from the direction cosines of the normals to the digitized plane (Sturzenegger and Stead, 2009a). By comparing the different sections of the digital model and the corresponding aerial images, representative discontinuities by each DTM were mapped. This allowed to check and correct the digitized surfaces. For each discontinuity, coordinates were extracted, in addition to their dip, dip direction and magnitude (the exposed trace length of the persistence), which were then plotted on stereonet and histograms. A discussion about the selection criteria used to reduce the subjectivity component related to the mapping of discontinuities whether using photogrammetric models, TLS models, mapping windows or scanline survey is shown in Chapter 5.1.

Following the methodological approach described in Mathis (2011), an approximate distance to the model of 0.5 m was used for mapping, which was variable depending on the rock exposure and the quality of the model in some areas (due to shadows and blurred areas). Further, two main criteria for mapping were applied:

- a) Fresh chalk surfaces were selected. Adopting the weathering grades of ISRM (1981), a fresh rock mass (grade I) is characterized by no visible signs of weathered material; perhaps slight discoloration can be present (i.e. white chalk, without vegetation or degraded surfaces);
- b) Smooth, flat and non-roughened chalk surfaces, thus prone to sliding.

An example of both approaches for mapping can be seen in Figure 27.

The different types of mapped discontinuities (joints, faults and bedding planes) were differentiated by coloured disks in order to facilitate the spatial analysis: joints were represented by blue disks, faults by red disks and bedding planes by green disks (Figure 27). The disk sizes are proportional to the extent of the points digitized. Hence, they indicate the relative magnitude of the discontinuity (i.e. exposed persistence)

The persistence of a discontinuity can be mapped as the areal extent of each discontinuity (ISRM, 1978). However, persistence is one of the most difficult rock slope

characteristics to measure because often only a small section of the discontinuity is exposed in the slope face (Wyllie and Mah, 2004). For that reason, the approximate persistence of discontinuities was mapped considering their exposed trace length on a specific area of the face (Pahl, 1981; Priest and Hudson, 1981; Wyllie and Mah, 2004). In addition, adopting the approach applied by Sturzenegger and Stead (2009a), the diameter of the circular discontinuity was considered as the exposed trace length.

Figure 27: Example of mapped joints based on a DTM



Blue disks: joints that do not belong to a set; Yellow disk: Joint Set 1 (JS1); Orange disks: Joint Set 2 (JS2).

3.4 KINEMATIC ANALYSIS

The kinematic slope stability assessment takes into account the relative attitude of the discontinuities and the slope face, in addition to the friction angle along the discontinuity surfaces (Eberhardt, 2003). In order to examine the kinematic possibility of planar, wedge and toppling failure, the discontinuity data were assessed utilizing stereonet. This was undertaken using the stereographic projection Dips 7.0 software (Rocscience, 2016a).

3.4.1 Identification of modes of slope instability

The following sub-sections, presented the structural geometrical conditions related to rock slopes that generate block slide failures and the specific stereonet techniques used to recognize them based on Richards et al. (1978), Goodman (1989), Hoek and Bray (1981), Hudson and Harrison (2000), and Wyllie and Mah (2004). These geometric conditions for slope failure are implicit in the dips codes, being relevant to understanding the kinematic analysis undertaken and associated outputs.

3.4.1.1 Geometrical conditions for plane failure

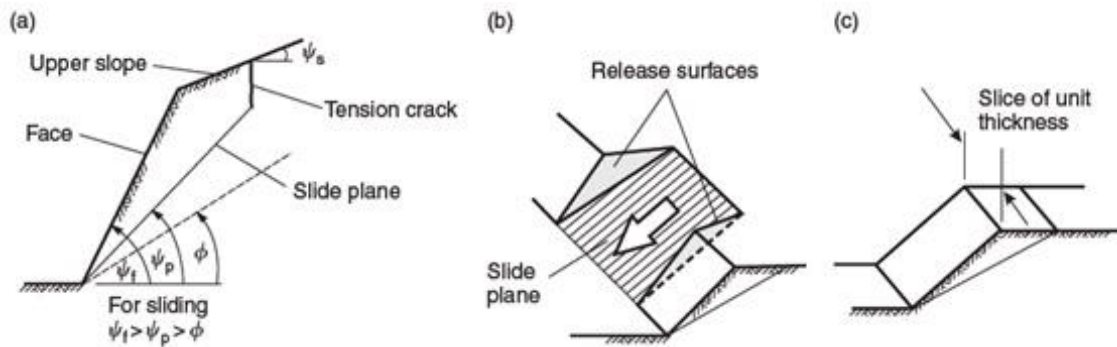
Figure 28 shows the geometry of a planar failure in which a block tends to slide on a single plane surface dipping out of the face. In this case, the block will slide down the slope parallel to the dip of the weak plane (Goodman, 1989). To consider the kinematic possibility of plane failure occurring, the following criteria must be satisfied (Figure 28):

- a) The dip direction of the sliding plane should be within a range of $\pm 20^\circ$ with respect to the dip direction of the slope face. This is an empirical condition which results from the observation that plane slides tend to take place when the released blocks slide more-or-less straight out of the slope face, rather than at a very oblique angle (Hudson and Harrison, 2000).
- b) The dip of the slope face must be greater than the dip of the potential slip plane. With this, the sliding plane intersects in the slope face ($\psi_p < \psi_f$).

- c) The dip of the potential slip plane must be such that the strength of the plane is reached. In the case of friction-unique planes, this means that the dip of the discontinuity must be greater than the friction angle ($\psi_p > \phi$).
- d) The upper end of the potential slip plane either terminates in a tension crack, or intersects the upper slope.
- e) Release surfaces that provide low resistance to sliding must exist within the rock mass to define the lateral boundaries of the slide. Or, a slide can occur on a failure plane passing across the convex nose of a slope.

In addition, it should be noted that the assessment of planar failure can be influenced by the presence of water pressure (pore pressure) along the failure surface. This can cause sliding even if the friction angle is higher than the dip direction of the discontinuity (Lara and Sepulveda, 2008).

Figure 28: Geometrical conditions of a slope showing plane failure

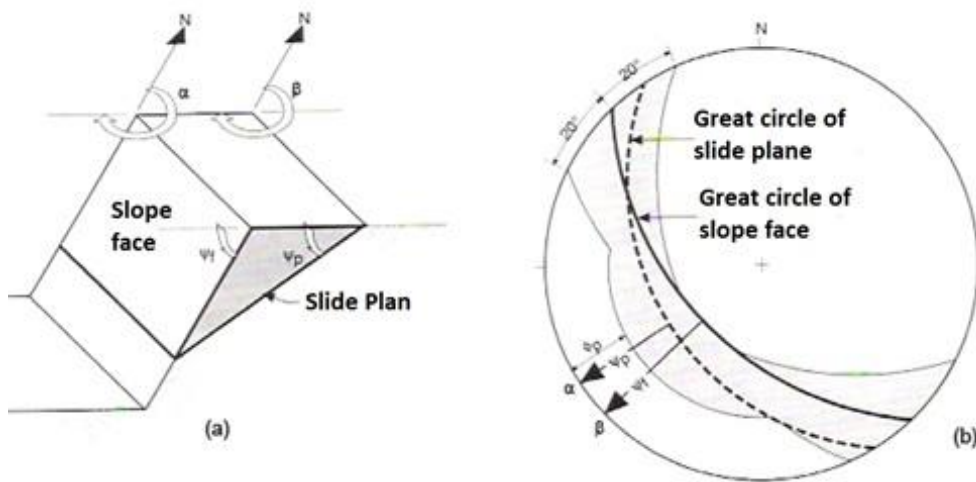


Source: Wyllie and Mah (2004). a) cross-section showing the aforementioned criteria; b) schematic release surfaces controlling the boundaries of the sliding surface; c) unit thickness slide utilized for stability analysis.

The conditions a), b) and c) can be seen in the schematic stereonet of the Figure 29b. Here, the kinematic requirements for planar sliding are satisfied if the dip vector of a possible plane of sliding plots lie within the grey region above the great circle of the slope face, in which $\psi_f > \psi_p > \phi$ (Goodman, 1989).

Based on the aforementioned criteria, in the codes of the utilized software, the critical region for planar failure is defined as outside the cone that represents the friction angle (which, in the case of pole vectors, is measured from the centre of the stereonet towards its perimeter) and inside the daylight envelope (whose external boundary is determined by the position of the pole plot that represents the slope face). Hence, any pole that lies within this zone of the stereonet represents planes prone to slide (Rocscience, 2016b).

Figure 29: Stereographical depiction of structural conditions for planar failure



Source: Modified from Lara and Sepulveda (2008).

3.4.1.2 Geometrical conditions for wedge failure

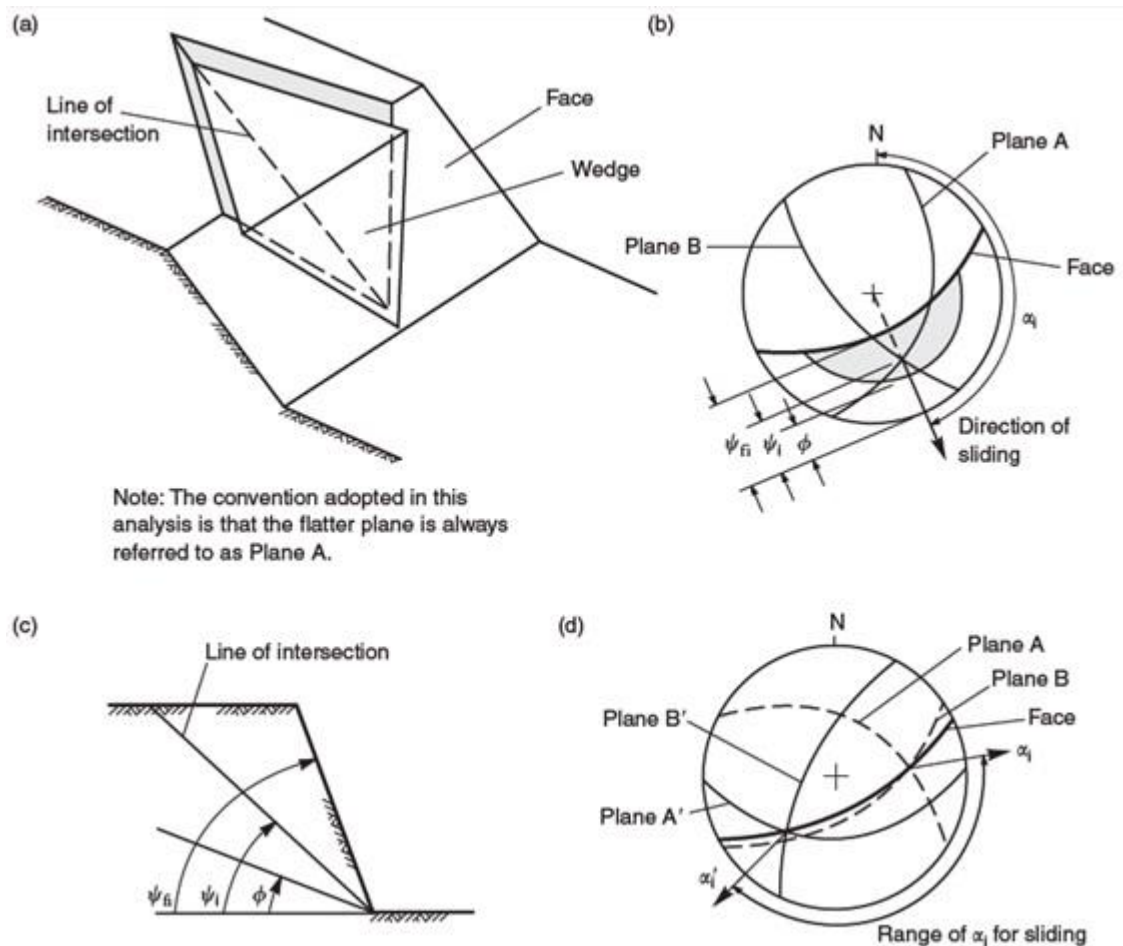
Wedge failure can be understood as a variation of plane failure, in the sense that the sliding zone takes place on two discontinuity surfaces (Figure 30). The resultant sliding direction is assumed to be in a direction common to both surfaces, namely, along their line of intersection (Hudson and Harrison, 2000). The geometrical conditions to consider a kinematic feasibility of wedge failure are as follows. They are shown in Figure 30.

- The dip of the slope must be greater than the dip of the line of intersection. With this, the sliding plane intersects in the slope face ($\psi_{fi} > \psi_i$).
- The dip of the line of intersection of the discontinuity planes must be such that the strengths of the two planes are reached. In the case of friction-only planes, each possessing equal angle friction angle, the dip of the line of intersection must be greater than the friction angle ($\psi_i > \phi$). In the case of friction angles where both planes are very different, the mean of both friction angles are considered.
- If the dip of the discontinuity planes is less than both dip direction of the slope face and dip direction of the line of intersection, the sliding will occur in the plane with the greater dip; otherwise the sliding will take place along the line of intersection.

Further, it should be noted that the planar failure condition associated with the $\pm 20^\circ$ variation in sliding direction is not required for wedge instability, since the sliding direction is solely determined by the line of intersection (Hudson and Harrison, 2000).

On the stereonet (Figure 30b), the line of intersection is depicted by the point in which the two great circles of the planes intersect, and the orientation of the resulting lines is determined by its trend (α_i) and dip/plunge (ψ_i). Furthermore, the line of intersection must dip in a direction out of the slope face for wedge instability to be possible. In this sense, the possible range for the trend of the line of intersection is between α_i and α'_i (Figure 30d). Sliding will take place if the intersection point between the two great circles of the planes lies within the grey area of Figure 30b (Wyllie and Mah, 2004). This region is known as daylight envelope area of the stereonet. Any intersection that lies within this zone is in the critical zone for wedge sliding (Richards et al., 1978). Since for wedge instability intersection pole plots are used on the stereonet, the region of instability is on the same side as the considered dip direction of the slope face (Hudson and Harrison, 2000).

Figure 30: Geometrical conditions of a slope showing wedge failure



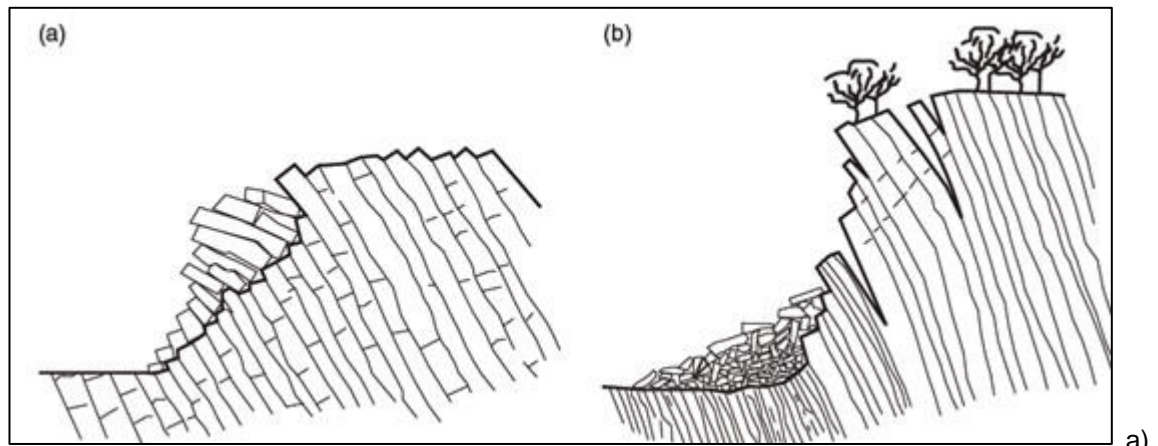
a) schematic view of wedge instability; b) stereonet displaying orientation of the line of intersection and daylight envelope region; c) cross-section showing the aforementioned criteria; d) stereonet displaying the range in the trend of the line of intersection (α_i) where wedge instability is possible. Source: Wyllie and Mah (2004).

Based on the aforementioned criteria, in the codes of the utilized software, the primary critical zone for wedge instability is the region inside the friction cone (measured from the perimeter of the stereonet towards the centre) and outside the great circle of the slope face. The secondary critical zone is the region between the slope face great circle and a great circle inclined at the friction angle value. Critical intersections lie in this region that represent wedges which slide on one discontinuity plane. In this case, the second discontinuity surface acts a release plane (condition c). In the primary critical zone fail wedges that slide both along the line of intersection and/or on a single discontinuity surface (Rocscience, 2016b).

3.4.1.3 Geometrical conditions for flexural toppling

Figure 31b depicts a schematic flexural toppling failure, in which continuous columns of rock, divided by steeply dipping discontinuities (into the slope face), break in flexure as they bend forwards. Here, orthogonal jointing is not well developed, hence the basal plane of a flexural toppling is not as well determined as a direct toppling (Wyllie and Mah, 2004). Interlayer sliding must take place before flexural deformations can develop (Goodman, 1989).

Figure 31: Scheme of direct and flexural toppling



a) Direct toppling, characterized by basal orthogonal joints. b) Flexural toppling, with joints dipping steeply into the slope face. Source: Wyllie and Mah (2004).

The geometric assessment and related conditions for inter-layer sliding occurring are utilized for the kinematic feasibility analysis for flexural instability. As demonstrated by Hudson and Harrison (2000), the geometric condition for inter-layer slip to take place is:

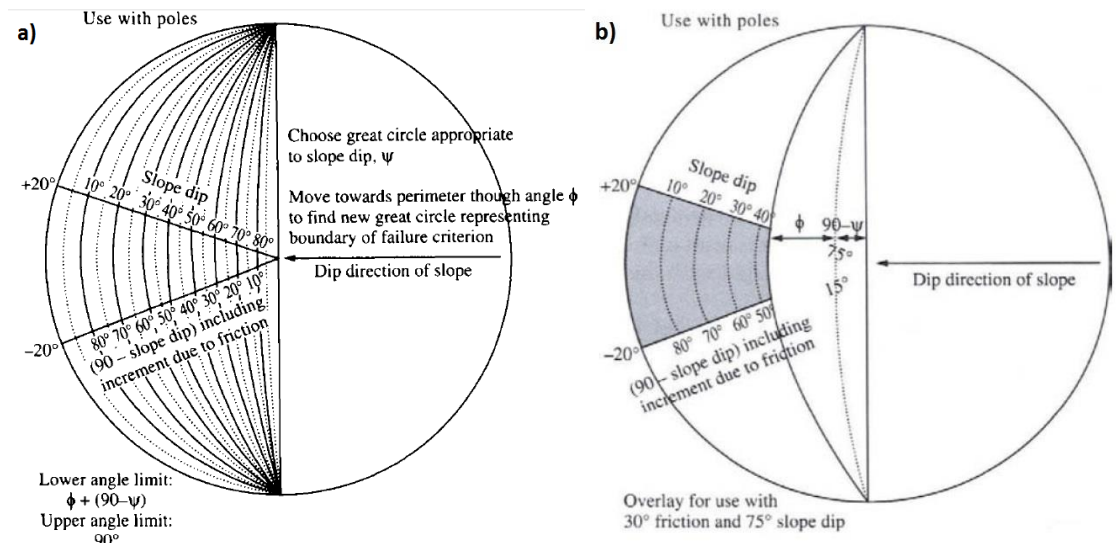
$$\beta \geq \phi + (90 - \psi) \quad (8.1)$$

Where ψ is the slope face dip, ϕ is the angle of friction related to the discontinuities, and β represents the dip of discontinuities. In terms of the stereographic projection overlay analysis, it is important to assess the location of the discontinuity pole plots on the projection, which show the potential for inter-layer sliding (Hudson and Harrison, 2000). The conditions to consider a kinematic feasibility of flexural toppling failure are as follows:

- a) The dip direction of potential slip surface must lie approximately parallel to the slope face, namely within a range of $\pm 20^\circ$ with respect to the slope. This is an empirical condition since inter-layer slipping tends not to take place when discontinuities occur obliquely to the slope face.
- b) The dip of the potential discontinuities to generate flexural failure (β) must lie in the opposite direction with respect to the dip of the slope ψ (i.e. dipping into the slope). Conditions a) and b) mean that the difference between the dip direction of β and the dip direction of the slope must lie within a range of $160^\circ - 200^\circ$.
- c) The line of the normal to the potential plane of flexural failure ($90 - \beta$) must be lower than the slope face dip (ψ) minus the friction angle (ϕ):

$$(90 - \beta) \leq (\psi - \phi) \quad (8.2)$$

Based on the aforementioned conditions, the stereonet overlay of flexural toppling is created from great circles showing the plane of the slope, and pole plots to determine the areas of instability related to the dip of the discontinuity planes. In Figure 32a, the radial solid line orientated to the left represents the slope face direction and the great circles indicate planes corresponding to both the slope and the friction angle of the slipping discontinuity planes. Figure 32b shows the zone of instability. From this, it can be seen that the dip angle of the dotted great circle (depicting the slope face) is ψ , and the complement of this angle (i.e. the angle to the vertical) is $90 - \psi$. Inter-layer slip will solely take place for discontinuities dipping at an angle of friction ϕ greater than this, resulting in a zone of instability outside the solid great circle. Finally, utilizing the condition a), the shaded instability region is produced (critical zone) for superimposition on discontinuity pole plots (Hudson and Harrison, 2000). In the utilized software codes, the region between the solid great circle or slip limit (slope face angle – friction angle = 45°) and the perimeter of the stereonet determine the critical zone for flexural toppling. Any pole on that area indicates a hazard due to flexural instability (Rocscience, 2016b).

Figure 32: Construction of stereonet overlay for flexural toppling

Source: Hudson and Harrison (2000).

3.4.1.4 Geometrical conditions for direct toppling

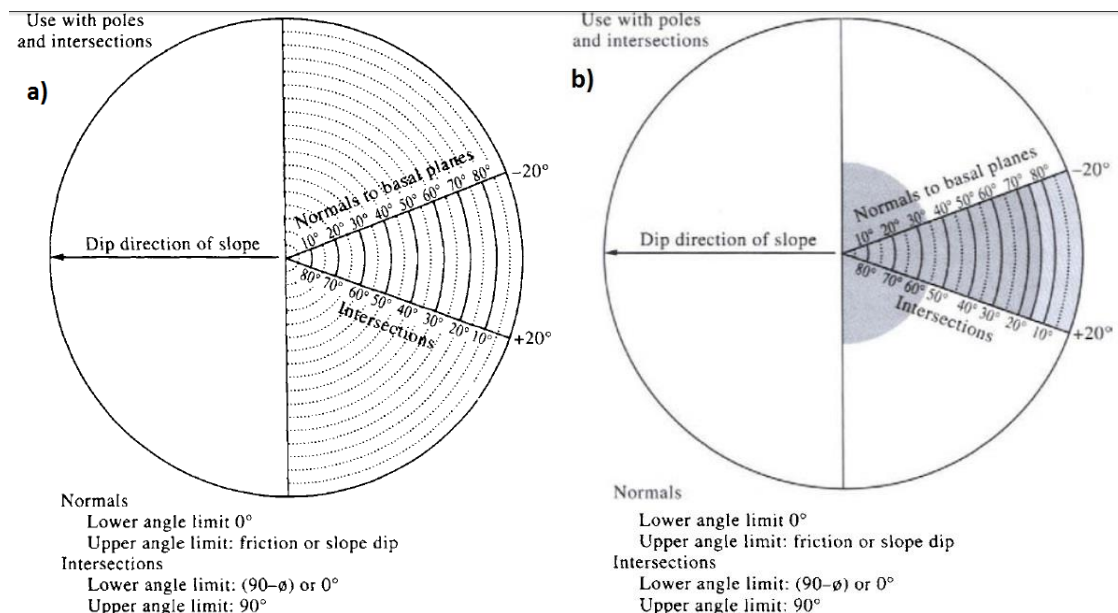
Direct or block toppling (Figure 31a) takes place when individual columns of strong rock are composed by a set of discontinuities dipping steeply into the slope face, however, in the case of toppling, a second basal set of orthogonal discontinuities determines the column height (Wyllie and Mah, 2004). For the case of instability, the kinematic feasibility condition will solely relate to the geometry of the rock mass, rather than geometrical conditions plus strength parameters (Hudson and Harrison, 2000). Hence, the two conditions required to trigger direct toppling are as follows:

- There are two sets of discontinuity surfaces whose intersections dip into the slope face. This permits the creation of discrete rock blocks.
- There is third set of near horizontal discontinuity surfaces that conform the basis of the toppling block. This set acts as release surfaces for the discrete blocks.
- The criteria a) for flexural toppling has been empirically observed for direct toppling as well ($\pm 20^\circ$), except for very steep slopes where lateral boundaries can be significantly enlarged.

Due to condition a) a stereonet overlay for intersections points is needed; from condition b) an overlay for pole plots must be used. Here, intersections and pole plots are superimposed and a composite overlay is utilized (Figure 33).

According to Figure 33a, the radial solid line orientated to the left represents the slope direction. Since the interest is in the angles between the vertical and the plunge of the lines of intersection and the dip of the basal discontinuities, the overlay technique will be formed by concentric circles. These circles are numbered from the equator of the stereonet inwards for intersections, and from the centre outwards for poles (since intersections lines are dipping into the slope face, whereas basal discontinuities dip out of the slope face). The two radial lines indicate the lateral boundaries. In Figure 33b it can be seen that the oblique toppling region for intersections do not fall within the critical zone of instability. This lateral zone is limited by the friction angle and the orientation of the slope face.

Figure 33: Construction of stereonet overlay for direct toppling



Source: Hudson and Harrison (2000).

Based on the aforementioned technique, in the codes of dips, the external limit of the direct toppling critical zone is defined by the slope face cone (measured from the centre of the stereonet to its perimeter) and the lateral boundaries. The oblique toppling region is defined by the friction angle cone (measured from centre of the stereonet as well). Any intersection falling in these regions is critical and represents potential for direct toppling.

3.4.2. Parameters used for modelling the kinematic analysis

3.4.2.1 Friction angle

The friction angle value utilized for running the kinematic modelling was based on the baseline geotechnical parameters provided by Ove Arup and Partners (1984) and Mott MacDonald (2009). In these studies, it was concluded that a peak friction angle of 35° for the in-situ Newhaven Chalk of Brighton Marina should be used as a safe design parameter. This friction angle has been considered useful for the modelling, as it represents the same geological formation, and is in close proximity to the study site (i.e. 5 km between Brighton Marina and Telscombe cliffs).

Since there is only one reported ϕ parameter and corresponding to in-situ chalk, hence, not directly exposed to environmental influences like the Newhaven Chalk forming the face of Telscombe cliffs, a kinematic sensitivity analysis (KSA) was executed in order to test and discuss the behaviour of the model with respect to other chalk formation friction angles provided by the literature.

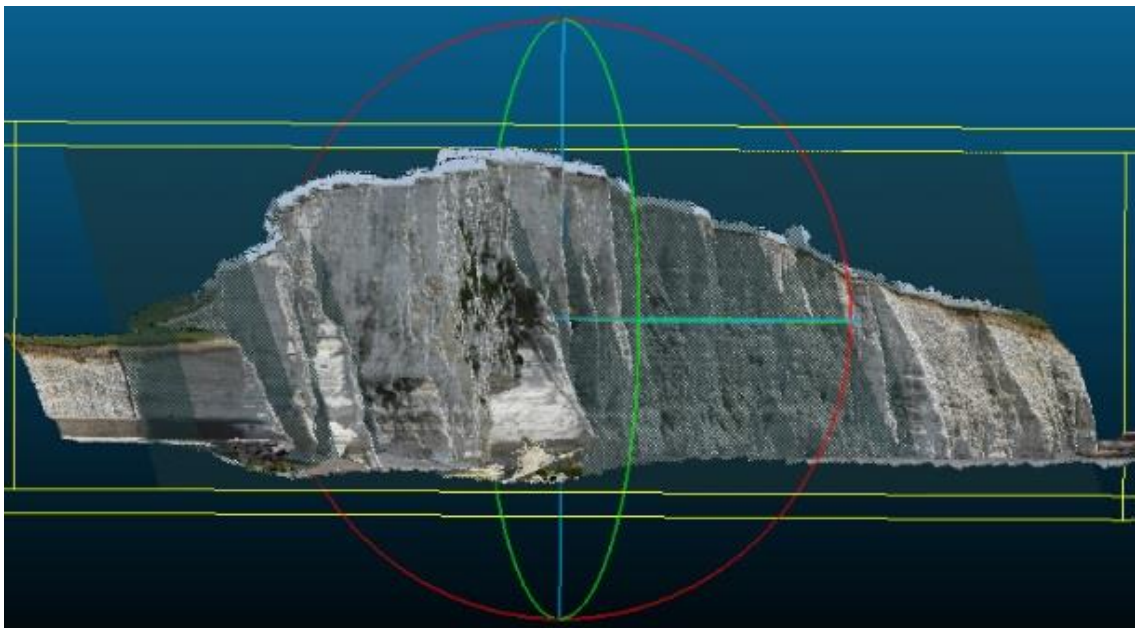
KSA consists of varying an input parameter (dip, dip direction, friction angle or lateral limits), while keeping others constant at their principal values (Richards et al., 1978). With this, the influence of one variable on the different modes of slope instability can be assessed, and how it relates with respect to other parameters and the actual distributions of pole plots and intersections points that generate instability.

The chalk is a rock that exhibits medium friction angle values, commonly ranging from 27° to 34° (Barton, 1973; Jaeger and Cook, 1976; Hoek and Bray, 1981). Further, Seaford Chalk ϕ has been reported to be 29° , while Lewes Nodular Chalk 33° (Taibi et al., 2009; Bedjaoui et al., 2010). For chalk putties, Jenner and Burfit (1974) in Bundy (2013) have reported consistent values of maximum 35° and an absolute minimum of 30° . Considering these, the KSA of ϕ was executed taking into account friction angles ranging from 29° to 35° .

3.4.2.2 Dip and dip direction

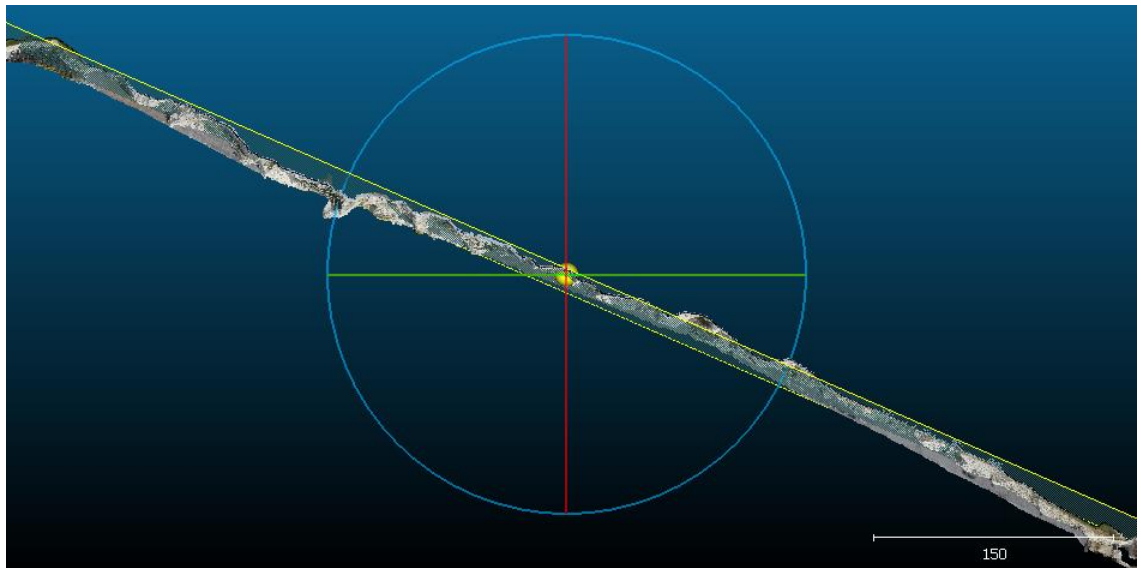
To determine the dip and dip direction of the cliff face, Cloud Compare software was used, which is a 3D point cloud and triangular mesh processing software. It has two automatized methods to specifically calculate the geological dip/dip direction parameters. The first, by determining the normals of cloud of points; the second, by fitting a plane on the feature of interest. Here, the second method was selected since it displays the axes to be considered for the calculus in addition to the plane from which dip/dip direction was defined. This plane corresponded to the average slope of the cliff face. Then, the dip of the cliff face was determined as the maximum inclination of the face below a horizontal trace. This trace was represented by a blue axis (Figure 34). Dip direction or dip azimuth was measured as the direction of the horizontal trace of the line of dip, measured clockwise from the north. From the zenith, the north was represented by a red line (Figure 35). Before doing this, the DTM was exported from the photogrammetric software as points. Then, the axis was defined from which the north (X), east (Y) and elevation (Z) was considered to orientate the models.

Figure 34: Determination of dip using Cloud Compare



The horizontal blue axis represents the horizontal trace above which the dip angle was calculated. The average slope face is depicted by the inclined rectangular plane. Dip = 76° for the entire cliff section.

Figure 35: Determination of dip direction using Cloud Compare



The red axis represents the horizontal trace from which dip azimuth was calculated. The plane of the average slope face is depicted in the inclined rectangular plane, whose boundaries are highlighted here with yellow. Dip direction = $203,8^{\circ}$ ($\sim 204^{\circ}$) for the entire cliff section.

3.4.2.3 Definition of cliff sections

In terms of the specific morphometry of the cliff per section, it can be noticed that it is not homogeneous in terms of the dip direction due to slight morphological changes in the general slope aspect of the cliff line. For this reason, and in order to assess possible variations on the modes of slope failure per each section of the cliff, the main morphometric misalignments were used with respect to the general aspect of the cliff line. By inspection of ortho-rectified aerial images, four principal morphological breaks points/changes within the cliff line were detected. Then, these points of misalignment were used as criteria to divide the cliff into five zones and extract their dip and dip direction (Figure 36).

Table 6 shows the results obtained from the division. According to the table, it can be seen that the dip ranges from 71° to 81° , while dip direction ranges from 199° to 207° ($\pm 3-5^{\circ}$ with respect to the general dip direction of 204°), with averages of 76° and 204° , respectively. Consequently, the aforementioned range of values were considered to execute a spatial kinematic analysis (section 4.3.3).

Figure 36: Definition of cliff sections

Black line shows general direction of the cliff face; Black points: points of principal misalignments; Colour lines: cliff sections.

Table 6: Ranges of dip and dip direction per cliff section

Cliff section (S)	dip (°)	dip direction (°)
S1	71	207
S2	75	204
S3	81	202
S4	80	199
S5	73	207
\bar{X}	76	203.8

-

4. RESULTS

4.1 DIGITAL TERRAIN MODELS

210 individual DTMs (Figure 37-42) with a computed image accuracy of 0.25 pixels and a 3DSE of 0.13m were used to accomplish the discontinuity mapping. The range of their principal characteristics are as follows (Table 7). Due to limited computer processing capabilities, it was not possible to create a merged DTM.

Table 7: Characteristics of the individual DTMs used for mapping

	Minimum DTM value	Maximum DTM value	Average
Number of Points	300,792	491,037	395,914.5
Number of triangles	601,559	982,052	791,805.5
Surface area (m ²)	2,155.42	3,461.56	2,808.49
Point density (points/m ²)	139.6	141.9	140.7
Mean spacing (m)	0.08	0.08	0.08

A summary of the accuracy obtained during interior and exterior orientation of the photogrammetric processing can be seen in Table 8. The entire report of the exterior orientation is shown in Appendix 4.

Table 8: Summary of model accuracy

Parameter	Meaning	Result
Posteriori Variance Factor (PVF) / Sigma	The Posteriori or empirical Standard Deviation SD (Sigma σ) is derived from the observation residuals and the redundancy given by repeated measurements (Luhmann et al., 2013). It is utilized to describe degree of correspondence of a set of observations with respect to standard deviations (ADAM Technology, 2010).	1.02
Computed Image Accuracy	Accuracy evaluates how close each measured value is to its associated true value (Sturzenegger and Stead, 2009). So, it describes the agreement between a measurement result and a measurement standard or accepted reference value (Luhmann et al., 2013).	0.25 pixels (x = 0.25, y = 0.26)
Control point residuals (m): (Ground co-ordinate residual)	Residual (deviation) is the difference between true and measured value (Sturzenegger and Stead, 2009a), in this case, between the control's point position and the bundle adjustment calculation (ADAM Technology, 2010).	X = 0.06, Y = 0.05, Z = 0.11
3D SE (m)	Accuracy is quantified by the mean error (ME), which is the sum of the residuals divided by their number. Precision quantifies the scatter, around ME, of repeated measurements on the 3D models. It is quantified by the standard deviation of error (SDE) (Sturzenegger and Stead, 2009a).	0.13

The posteriori variance factor obtained shows strong correspondence between the model and the residuals SD observations, since a value equal or smaller than 1 indicates that the data are as accurate as expected, meaning a value close to 1 shows correspondence (Birch, 2009). Hence, this parameter indicates that the spread of the data utilized is concentrated within the region of 1-sigma in the context of a Gaussian normal distribution. However, in many photogrammetric applications internal precision measures from adjustment results (e.g. sigma 0, RMS 1-sigma values) are shown as final accuracy values. In these cases, the performance of a model can easily be manipulated simply by increasing the number of observations (Luhmann et al., 2011). For that reason, the accuracy and precision of the achieved model is described here in complement with the rest of the parameters and further photogrammetric applications.

High accuracy in terms of the pixel size has been achieved, since the accuracy of any point location within the model is in a range of 0.25 pixels (RMSE). Using UAV photogrammetry for slope stability purposes, Francioni et al. (2015), reported RMSE between 0.60 and 2.2 pixels. Utilizing close-range terrestrial digital photogrammetry (CRTDP) with combination of DGPS and total station surveying for rock slope characterization purposes, Salvini et al. (2013) reported RMSE between 2.3 and 4.7 pixels. These values are notably higher compared with the computed image accuracy achieved in this research. Further, the achieved image accuracy of 0.25 is within a range of 0.1 and 0.5 pixels, which is an acceptable pixel accuracy result according to the photogrammetric software provider (ADAM technology, 2010). The achieved value is lower than the estimated image accuracy defined during the photogrammetric flight planning (0.5 pixels) as well. Thereby, the achieved level of pixel detail and accuracy permits the measurement of rock mass discontinuities using remote-sensing techniques (McCaffrey et al., 2005; Sturzenegger and Stead, 2009b).

Ground coordinate residuals of 0.06, 0.05 and 0.11 m were achieved for the x-axis (Eastings), y-axis (Northings) and z-axis (Elevation), respectively. In the case of x-axis and y-axis, the standard error is almost the same, since the maximum and minimum range of SE is relatively homogeneous, namely between +0.11 and -0.11m for both, coordinates that were measured utilizing dGPS and total station (this without considering an outlier of 0.15 for a GCP measured at the top in x-axis). In contrast, the SE of elevation is slightly higher, since higher individual SE values (around 0.19m) can be seen for all the coordinates that were measured at the cliff top using DGPS. A SE for elevation axis of about -0.09m was measured in 9 out of 18 points of the cliff base that were measured using Total Station. The aforementioned residuals yield an overall model's 3DSE of 0.13m.

Francioni et al. (2015), reported 3DSE values between 0.033 and 0.048m. Utilizing CRTDP Sturzenegger and Stead (2009b) and Salvini et al. (2013), reported 3DSE values between 0.2-0.02 m and 0.07-0.02 m, respectively. Excluding the mentioned 3DSE of 0.2m, the aforementioned values are more precise in comparison with the 3DSE achieved in this model, nonetheless, 0.13 m is slightly over (3mm) than the 0.1m usually achieved using LiDAR (Kumi-Boateng, 2012). Hence, according to Hussain and Bethel (2004) the centimetric 3DSE result is suitable for engineering photogrammetric purposes (e.g. around 15 cm).

Possible sources of uncertainty of the coordinate residuals could be associated with the dGPS and/or total station surveying, the variable focus lens used, unfavourable areas within the image configuration, the photogrammetric software in terms of matching points, extrapolation or resection stages (Birch, 2006; Beraldin, 2004; Boehler et al. 2003, El-Hakim et al., 2003; Johansson, 2003; Lichti et al., 2002). However, further research/analysis about the specific sources of uncertainty of the achieved coordinate residuals is not part of the objectives of this research.

With respect to the quantitative geomorphic assessment that can be derived from the DTMs, Figure 37 shows pyramidal cliff face profiles induced by steeply inclined conjugate sets of joints, which are inherent characteristics of the Newhaven Formation (Mortimore et al., 2004a). In addition, it shows the boundaries between cliff sections (1 to 5), and weathered chalk zones. Table 9 shows morphometric characteristics that were measured from the photogrammetric models, such as mean slope plane, aspect, height at the boundaries of each section, linear basal length and notch measurements.

Figures 38 to 42 show cliff sections with the spatial distribution of notch measurements. Regarding notch morphometry, the main criteria for the selection of notches for mapping was basal length greater than one meter. Then, their maximum height, depth and basal lengths were measured (Table 9). Nevertheless, it should be considered that these measurements are only valid for the date the aerial images were captured (UAV survey of 27/05/2016) as cliff failures are frequent at this undefended coastal section.

Cliff section one or S1 (Figure 38) is the longest (198m). However, it has the lowest mean slope plane (71°), and an average height of 29 m. Six notches were measured, ranging in height between 0.7 and 3.8 m, and in length between 1 and 6.1 m, with most no deeper than 0.5 m. At this section, the mean height, depth and length are 2.1, 0.6 and 3.2 m, respectively. By contrast, section two or S2 (Figure 39) is the shortest (87 m). However, it shows higher average slope (75°) as well as higher mean elevation (39 m). With respect to notch morphometry, the mean depth and length is 0.4 and 3.5 m, which are

almost the same measurements if they are compared with the average depth and length of S1 ($\pm 0.2/0.3$ m, respectively). However, the average notch height is slightly lower (1.4 m), when compared with the mean notch height of S1 (2.1 m).

Section three or S3 (Figure 40) is the second longest of Telscombe, with a basal length of 191 m. However, it shows the highest mean slope plane (81°), demonstrating that this section is almost vertical. The average elevation is the highest (43 m) as well. In terms of notch geometry, the height and basal length is notably higher when compared with S1 and S2, ranging in height between 3.5 and 8.3 m, and showing a basal length between 3.5 and 17.3 m. At S3 the average notch depth is 1.2 m, due to an outlier of 3.6 m (notch 6). Section four or S4 (Figure 41) shows a basal length of 145 m, but, similarly to S3, this section is near vertical (80°). On the other hand, although S4 shows an average elevation of 40.7 m, the highest height of Telscombe (49 m) is found around the centre zone of S4. Notches belonging to S4 are by far the most developed as a consequence of marine erosion. To illustrate, their heights range from 5.6 to 10.3 m, while the lengths are between 6.1 and 31.6 m. As a result, the average height, depth and length is 8.0, 9.6 and 15.6 m (respectively).

Section five or S5 (Figure 42) shows a linear basal length of 120 m, and the average slope plane declines to 73° . Similarly, the mean cliff elevation falls to about 27 m; therefore, S5 shows a similar morphometry in terms of mean slope of the cliff face and height, if compared with S1. Regarding notch geometry, the height ranges are from 1.0 to 6.6 m, the length ranges between 2.9 and 20 m, while the depth ranges are between 0.3 and 1.9 m. Given these results, the mean notch height and depth of S5 and S1 are similar.

Although all sections show the same aspect (SSW), these measurements not only show that S3 and S4 are the highest and steepest sections of Telscombe, but also that they are the most active or unstable sections due to evidence of higher marine basal undercutting, inducing deep and concentrated sequences of lateral notches. To summarize, this geomorphic unstable configuration is demonstrated by examining the mean notch heights, depths and lengths of S3 and S4, which are at least two or three times higher than notches belonging to S1, S2 and S5. Therefore, these measurements have the value of being indicative of marine erosion along a cliff base, being useful for coastal geomorphology assessment to determine critical basal zones prone to fail due to the lack of basal support.

Overall, the analysis of the aforementioned parameters indicates that strong network geometry and model precision was achieved, suitable for rock slope characterization and quantitative geomorphological analysis.

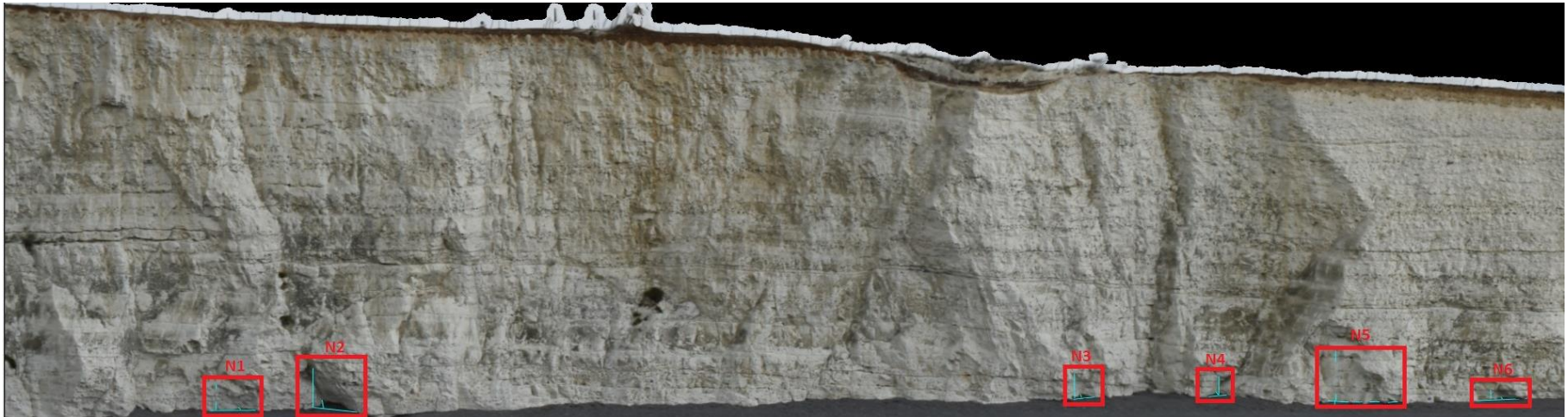
Figure 37: General view of Digital Terrain Models showing cliff sections

Lateral sequences of pyramidal profiles of the cliff face associated with steeply inclined conjugate joints sets as reported by Mortimore et al. (2004a). They can be seen across the entire length of the cliff. S1 to S5: cliff section 1 to section 5.

Table 9: Morphometric characteristics for cliff sections

Cliff section	Mean slope plane (°)	Facing direction	Height (Max/Min/Mean) (m)	Basal length (m)	Notch 1 (N1) (m)	Notch 2 (N2) (m)	Notch 3 (N3) (m)	Notch 4 (N4) (m)	Notch 5 (N5) (m)	Notch 6 (N6)	Notches (mean)
S1	71	SSW	36/23/29.5	198	Height: 2.0	Height: 3.0	Height: 2.0	Height: 1.5	Height: 3.8	Height: 0.7	Height: 2.1
					Depth: 0.5	Depth: 1.3	Depth: 0.5	Depth: 0.6	Depth: 0.6	Depth: 0.5	Depth: 0.6
					Lenght: 3.4	Lenght: 3.7	Lenght: 1.6	Lenght: 1.4	Lenght: 5.5	Lenght: 3.7	Lenght: 3.2
S2	75	SSW	41/36/39	87	Height: 2.4	Height: 0.6	Height: 0.2	Height: 2.0	Height: 2.3	Height: 0.9	Height: 1.4
					Depth: 0.5	Depth: 0.4	Depth: 0.3	Depth: 0.5	Depth: 0.3	Depth: 0.2	Depth: 0.4
					Lenght: 6.1	Lenght: 1.3	Lenght: 1.0	Lenght: 5.2	Lenght: 5.4	Lenght: 2.5	Lenght: 3.5
S3	81	SSW	45/41/43.5	191	Height: 6.3	Height: 4.0	Height: 3.5	Height: 5.4	Height: 4.7	Height: 8.3	Height: 5.3
					Depth: 0.5	Depth: 0.6	Depth: 0.9	Depth: 0.5	Depth: 1.0	Depth: 3.6	Depth: 1.2
					Lenght: 3.5	Lenght: 7.8	Lenght: 8.0	Lenght: 5.8	Lenght: 10	Lenght: 17.3	Lenght: 8.7
S4	80	SSW	45/36.5/40.7	145	Height: 5.6	Height: 9.4	Height: 10.3	Height: 8.3	Height: 8.9	Height: 5.8	Height: 8.05
					Depth: 2.5	Depth: 17.6	Depth: 15	Depth: 9.4	Depth: 7.7	Depth: 5.6	Depth: 9.6
					Lenght: 6.1	Lenght: 13	Lenght: 19.2	Lenght: 12.9	Lenght: 31.6	Lenght: 11	Lenght: 15.6
S5	73	SSW	36.5/19/27.7	120	Height: 6.6	Height: 1.0	Height: 1.8	Height: 2.1	Height: 1.1	Height: 2.2	Height: 2.5
					Depth: 1.9	Depth: 0.5	Depth: 1.3	Depth: 1.1	Depth: 0.3	Depth: 0.7	Depth: 1.0
					Lenght: 20	Lenght: 2.9	Lenght: 5.0	Lenght: 3.0	Lenght: 5.0	Lenght: 2.6	Lenght: 6.4

Figure 38: Cliff section 1 (S1), showing notch measurements



Red rectangles indicate position of notches; Blue lines show measurements of height, depth, and length.

Figure 39: Cliff section 2 (S2), showing notch measurements

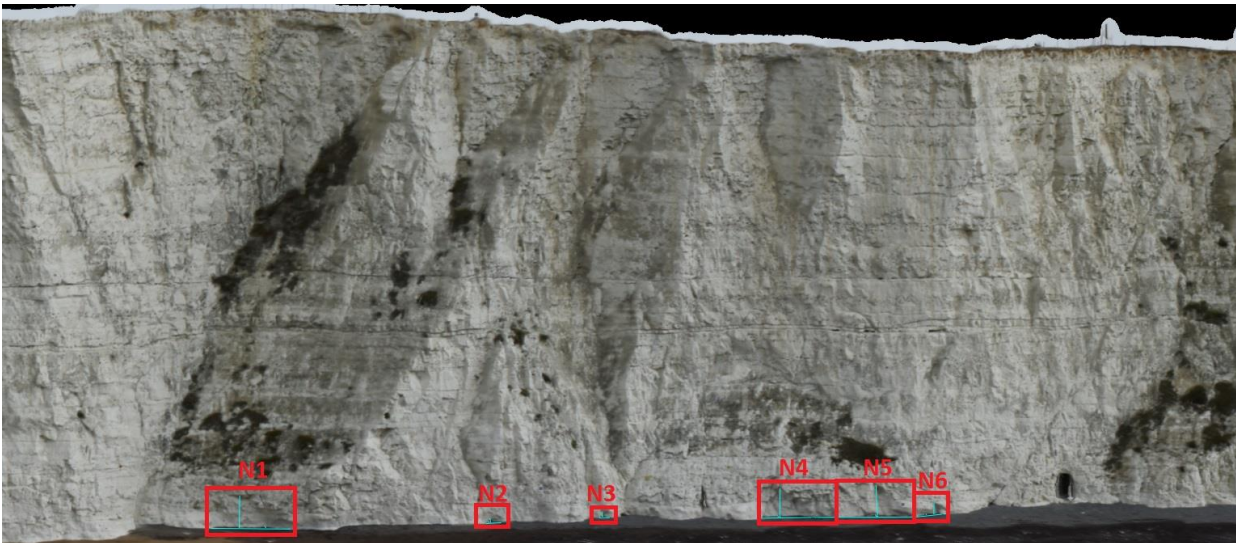
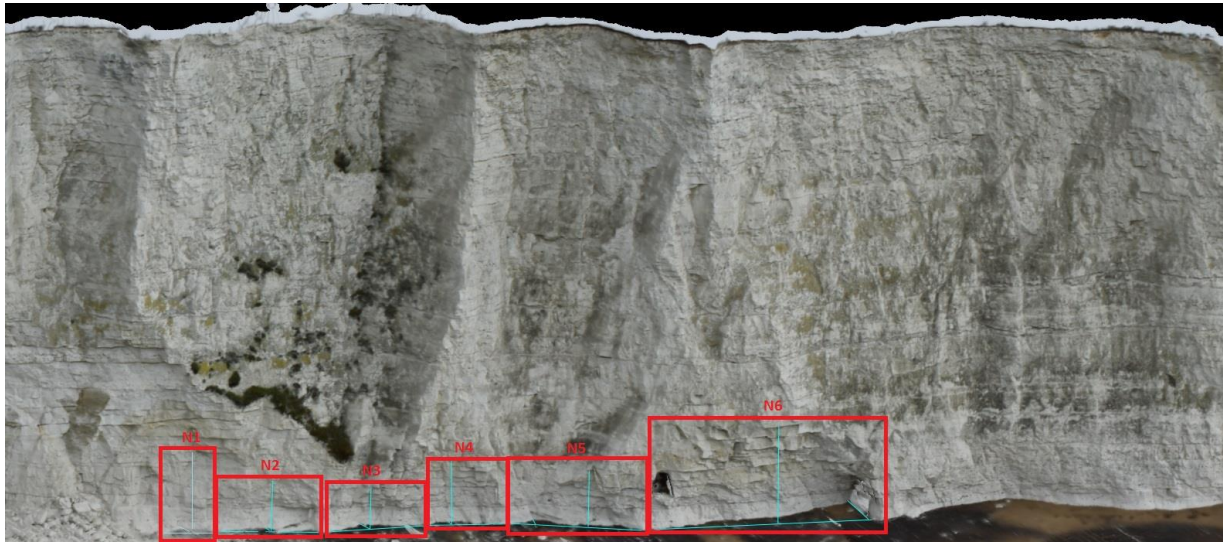
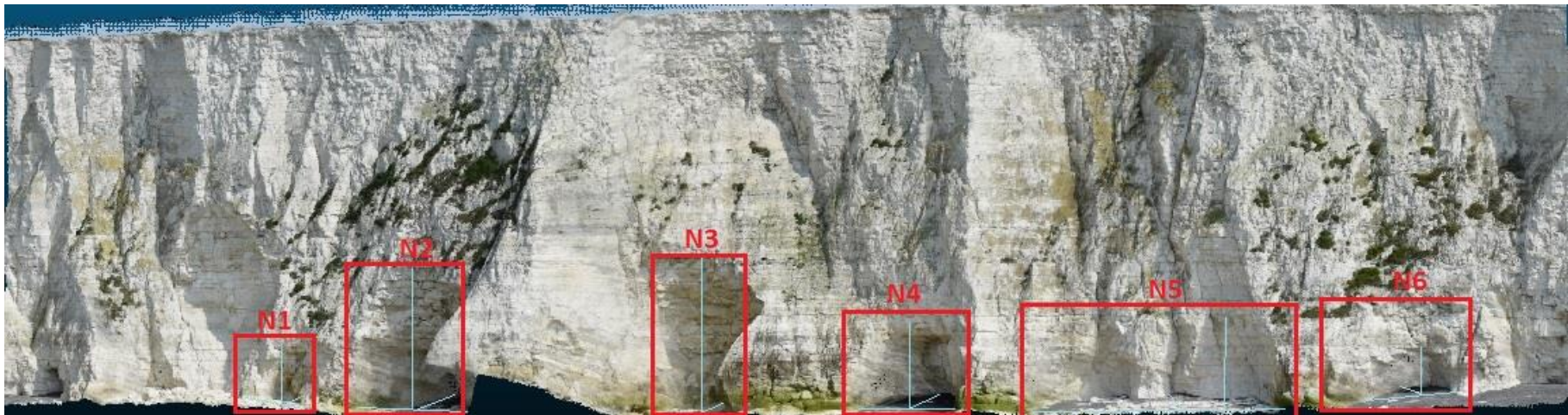


Figure 40: Cliff section 3 (S3), showing notch measurements



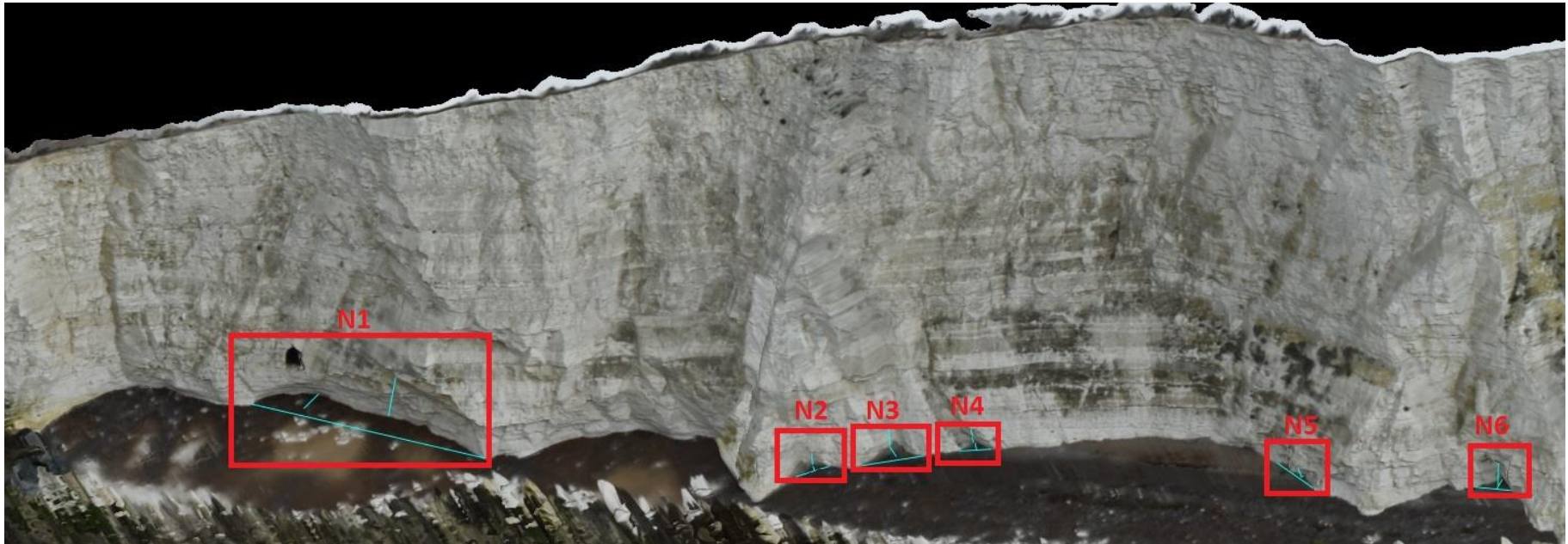
Red rectangles indicate position of notches; Blue lines show measurements of height, depth, and length.

Figure 41: Cliff section 4 (S4), showing notch measurements



Kinematic analysis of sea cliff stability using UAV Photogrammetry

Figure 42: Cliff section 5 (S5), showing notch measurements (oblique view)



Red rectangles indicate position of notches; Blue lines show measurements of height, depth, and length.

4.2 DISCONTINUITY MAPPING

From the structural geological mapping stage, 489 discontinuities were mapped along the cliff length (Figure 43). A summary of the data is presented in Table 10. Appendix 5 presents the input data used to accomplish the kinematic analysis.

Table 10: Summary of the data obtained from discontinuity mapping

Discontinuity type	Total number	Mean dip (°)	Mean dip direction (°)	Mean trace length (m)
Joints (total)	340	75.2	173.4	1.3
Joint Set 1 (JS1)	142	75.6	178.4	1.4
Joint Set 2 (JS2)	104	78.4	194.3	1.3
Faults	41	64.6	227.9	6.5
Bedding Planes	108	2.4	127	*

* No exposed trace length was measured.

For all joints, the mean dip/dip direction is 75.2°/173.4°, and the mean exposed trace length persistence is 1.3m. In this context, two main joint systems characterize Telscombe's cliff face: JS1 and JS2, which are classified as two different systems due to their differences in dip direction. JS1 presents slightly lower dip compared with JS2. However, both are steeply inclined, and present a variation of ± 10 cm with respect to the average joint trace length. These data support that reported by Lamont-Black (1995), Lawrence (2007), Mortimore et al. (2004a,b), since according to these authors, the style of fracturing of the Newhaven Chalk Formation between Brighton and Peacehaven is characterized by steep shear surfaces, dipping within an interval from 50° to 78°.

Mean dip angles of all joints and their two sub-systems tend to not correspond with those reported by Lemos de Oliveira (2013). Mean dip values of 67.5°, 52.4°, and 68.5° (average = 63°) were measured for the Newhaven Chalk of Brighton Marina, Peacehaven (Friar's Bay) and Newhaven (Castle Hill), respectively. However, the dip angles measured by Lemos de Oliveira (2013) represent undifferentiated discontinuities, which were measured at the base of the cliffs, using a scanline of 30 m of tape along the outcrop and a traditional compass clinometer. On the other hand, these values are still within the interval of 50-78°. Hence, due to the different applied methodologies (here, all the cliff face was considered, which means more statistical samples due to the advantages of using UAV photogrammetry), both approaches cannot be directly compared. In addition, according to Mortimore et al. (2004a), the chalk cliffs between Brighton and Newhaven have a general fracture direction, but vary from one area to

another due to some aspects like the number of fractures and concentration of a determined style of fractures in certain sections of the cliffs.

Another type of mapped discontinuity is associated with faulting processes, since Newhaven Chalk is commonly fragmented by normal and reverse faults due to the control exerted by the Friars Bay and Old Steine anticlines between Brighton and Saltdean. Moreover, these faults have an effect on the dip direction of the chalk and up to a point control the scale and type of cliff failures (Mortimore et al., 2004a; Stavrou et al., 2011). Faults tend to be located at the basal sections of the Telscombe cliffs (Figure 43). In some cases, opposite dip directions ($62^{\circ}/268^{\circ}$ v/s $64^{\circ}/105^{\circ}$) tend to form conjugate normal faults similar to those reported by Vandycke (2002) especially at the cliff base (Figures 44-48). The mean dip of faults is smaller than the mean dip of joints. However, faults have greater exposed persistence. The last confirms the tendency that faults usually have greater persistence and lower friction angle than joints (Hoek and Bray, 1981). On the other hand, the mean value of dip direction shown in Table 10 is only indicative, since it tends not to coincide with the principal cluster of faults shown on the stereonet (whose great circle has dip/dip direction = $61^{\circ}/291^{\circ}$), and also because the rest of the faults tend to show greater scatter in terms of their directions (see stereogram of Figure 58).

The third type of discontinuities are bedding planes (BP), which are represented by repeated layers of flints and marl seams, which are common in the Newhaven Chalk (Mortimore, 2014). As can be expected, the mean dip of BP is sub-horizontal. However, some of them present a degree of inclination (about 7°), probably due to the stress and pressures induced by the same regional tectonic forces that generated faulting. Indeed, BP with greater dip were found next to the different systems of mapped faults. No exposed frontal persistence associated with BP was measured since their length is as large as the entire cliff length, in fact extending beyond the study area, mainly interrupted/deformed by faulting systems and dry valleys. Hence, mapping their persistence requires further criteria to define their limits for mapping.

Figures 44-48 shows the mapped discontinuities for each section of the Telscombe cliffs.

Figure 43: Frontal view of all digitally mapped discontinuities

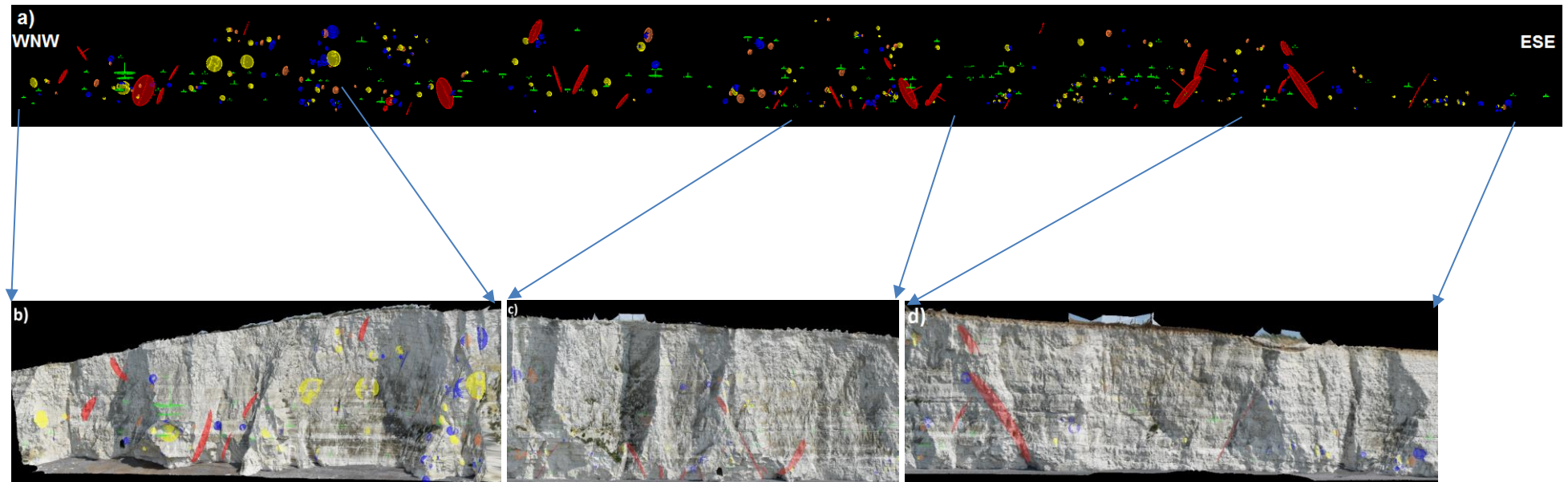


Figure 43a) Blue disks: undifferentiated joints; Yellow disks: JS1; Orange disks: JS2; Green disks: bedding planes; Red disks: faults. There are faults that tend to be concentrated at the cliff base, preferentially towards ESE of Telscombe. Representative discontinuity surfaces selected for mapping (i.e. fresh, smooth, non-roughened chalk surfaces, prone to slide) are distributed along the bottom, medium and upper sections of the cliff. Areas without mapped discontinuities did not meet the above requirements. They are located in some parts of the middle section of the cliff, and in the extreme WNW and ESE of the study area due to the presence of highly weathered chalk or patches with vegetation.

Figure 44: Discontinuities in the eastern section (S1: dip/dip direction = $71^{\circ}/207^{\circ}$). Number of mapped discontinuities: 71

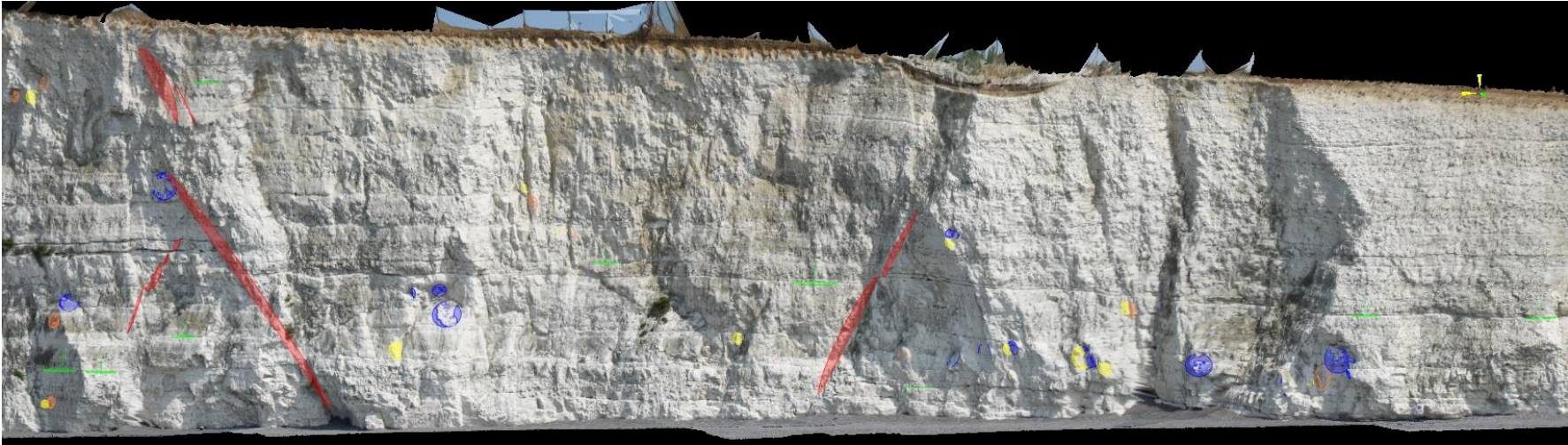


Figure 45: Discontinuities in central-eastern section (S2: dip/dip direction = $75^{\circ}/204^{\circ}$). Number of mapped discontinuities: 87.

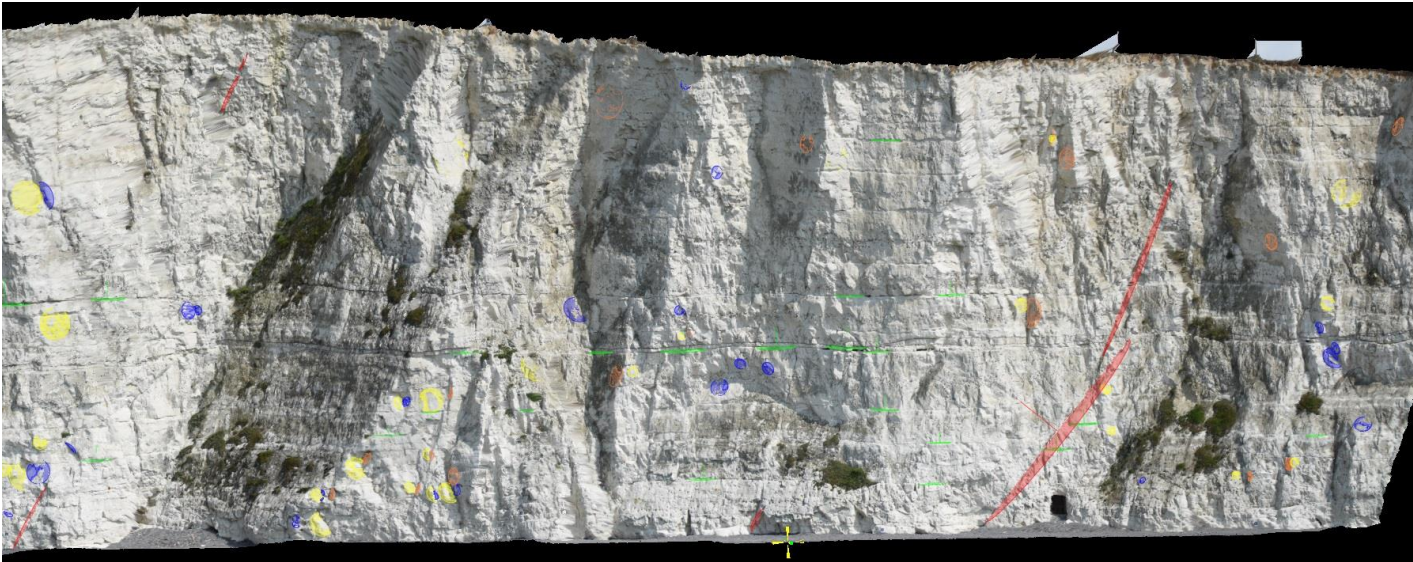


Figure 46: Discontinuities in the central section (S3: dip/dip direction = $81^{\circ}/202^{\circ}$). Number of mapped discontinuities: 143.

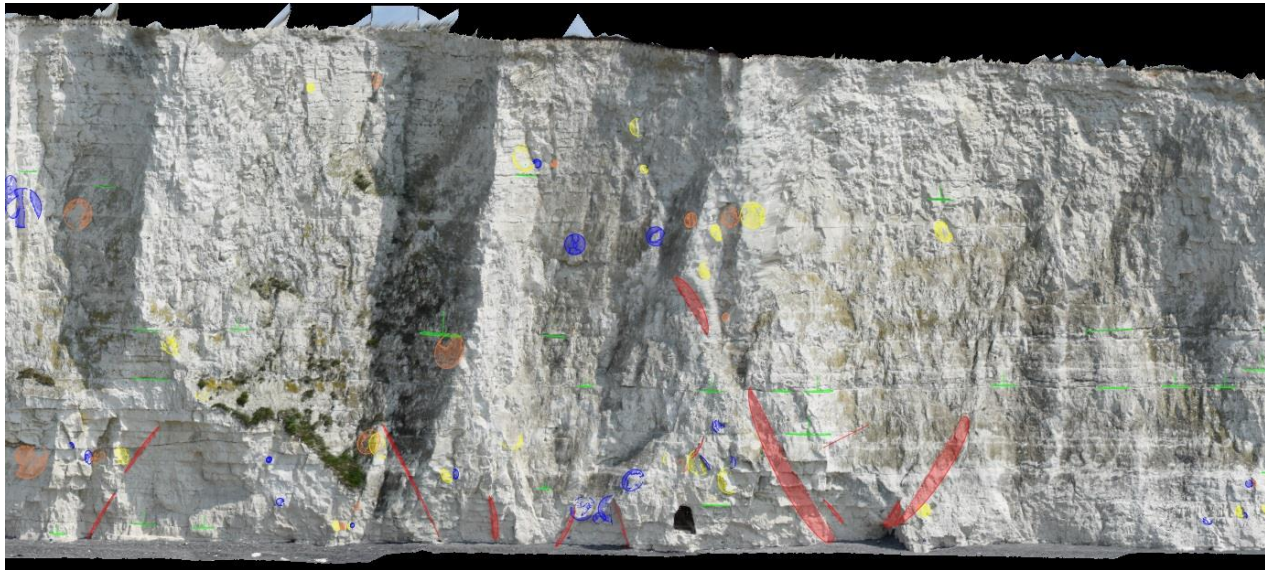


Figure 47: Discontinuities in the central-wester section (S4: dip/dip direction = $80^{\circ}/199^{\circ}$). Number of mapped discontinuities: 147.

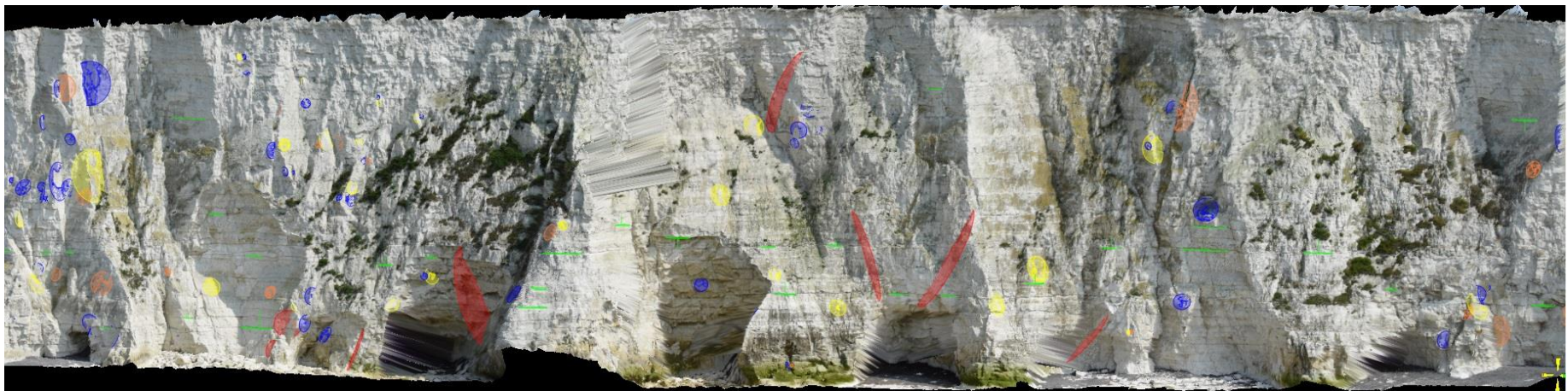
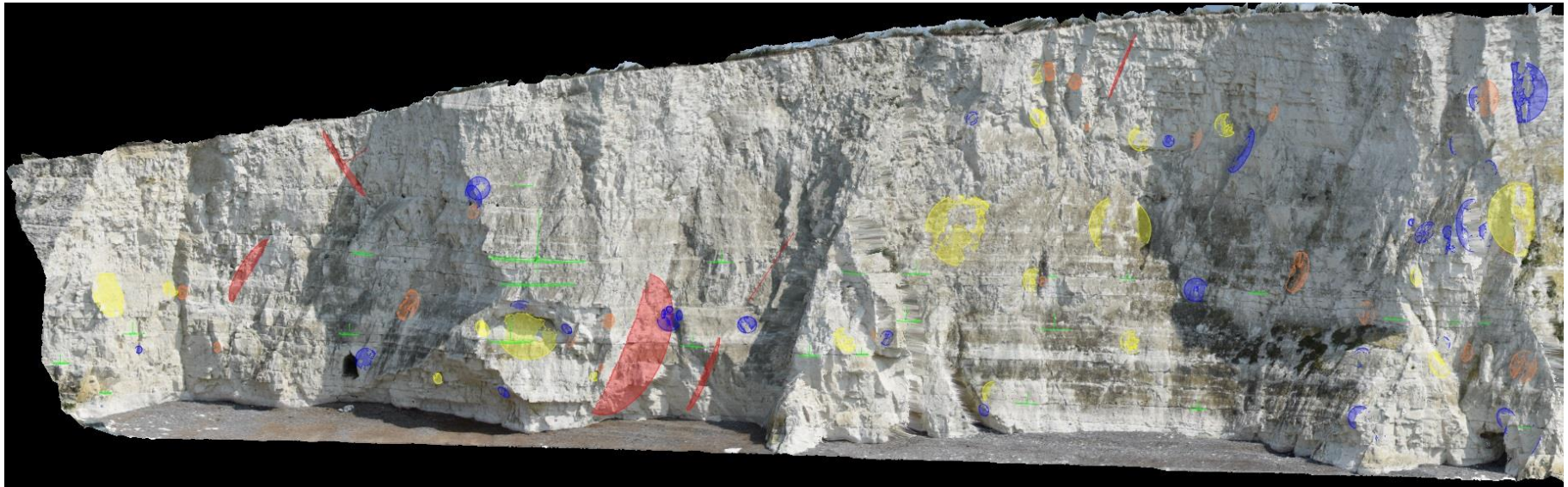


Figure 48: Discontinuities in the western section (S5: dip/dip direction = $73^{\circ}/207^{\circ}$). Number of mapped discontinuities: 41.

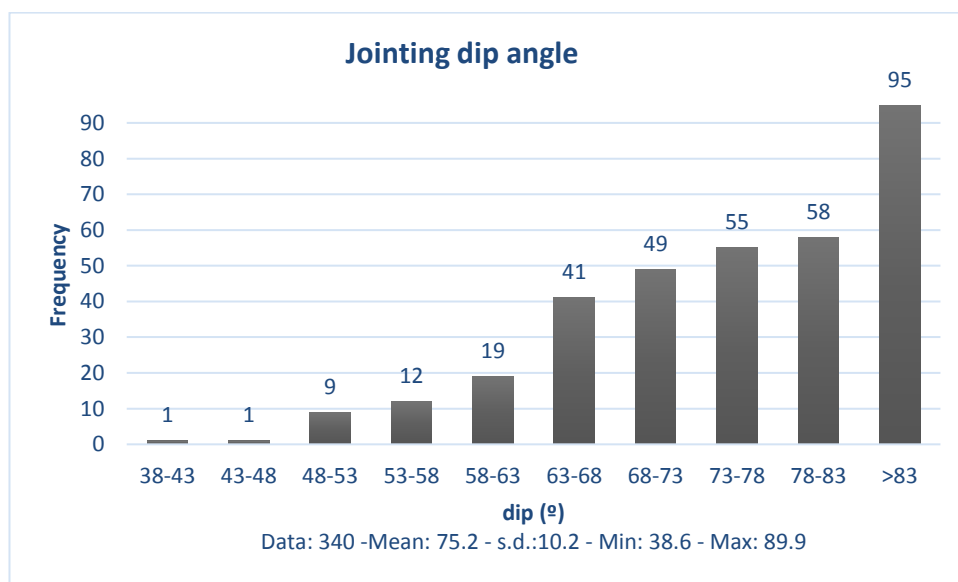


4.2.1 Frequency distribution of discontinuities

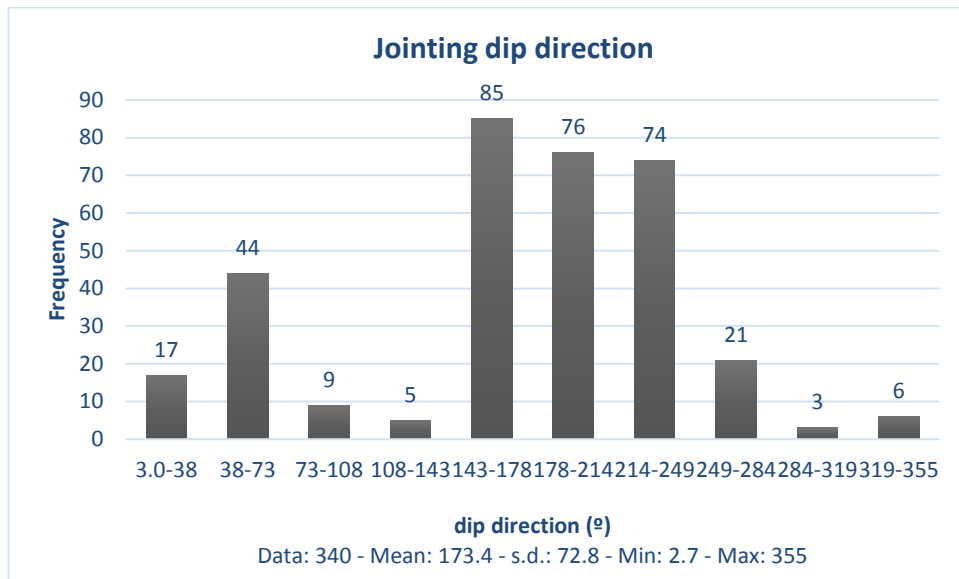
4.2.1.1 Joints

The histogram of the dip angle for all joints (Figure 49) shows a constant increase of the frequencies per interval as the dip angle increases. A range of 51.3° can be seen with an average of 75.2° , the mode is located at $>83^\circ$, and the shape of the graph suggest a left-skewed distribution of the data. Hence, these data show the predominance of highly inclined joints. Within this distribution, and considering that the mean cliff face has a dip of 76° , 132 joints have a lower dip than the interval that contains the mean dip of the face (73° - 78°), which means that these joints are prone to slide if they feature the other geometrical conditions for sliding.

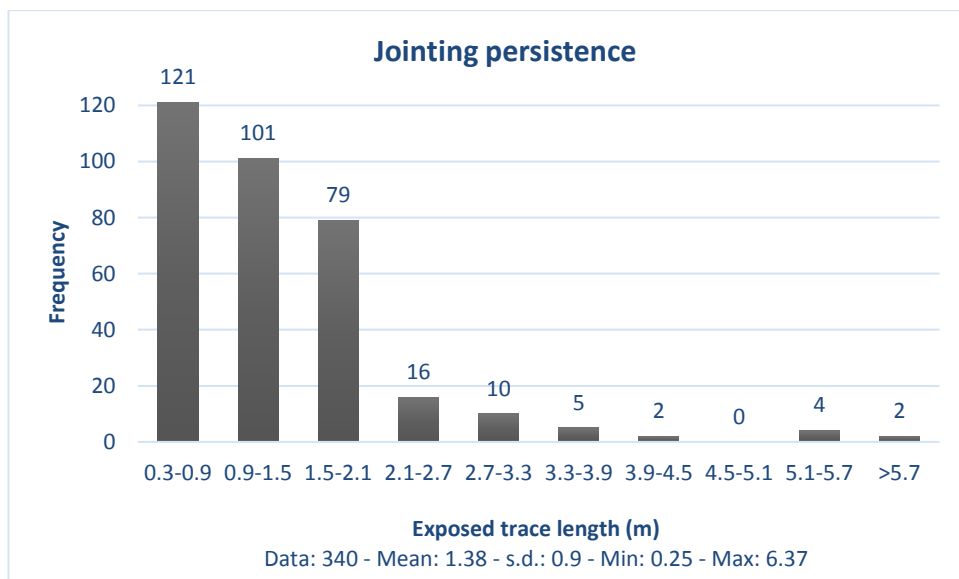
Figure 49: Histogram of jointing dip angle



In the case of jointing dip direction (Figure 50), most of the directions are concentrated between 143° and 249° , which matches with the direction of joint Set 1 and Set 2 (see rosette diagram and the general stereogram, Chapter 4.3.1). The range of the data is wide (352°), and the mode is located at 143° - 178° . By applying the criteria that the dip direction of the sliding plane should be within a range of $\pm 20^\circ$ with respect to the dip direction of the slope face (for study site = 204°), most of the joints in direction of sliding for planar and toppling failures are located within the interval 178° - 249° .

Figure 50: Histogram of jointing dip direction

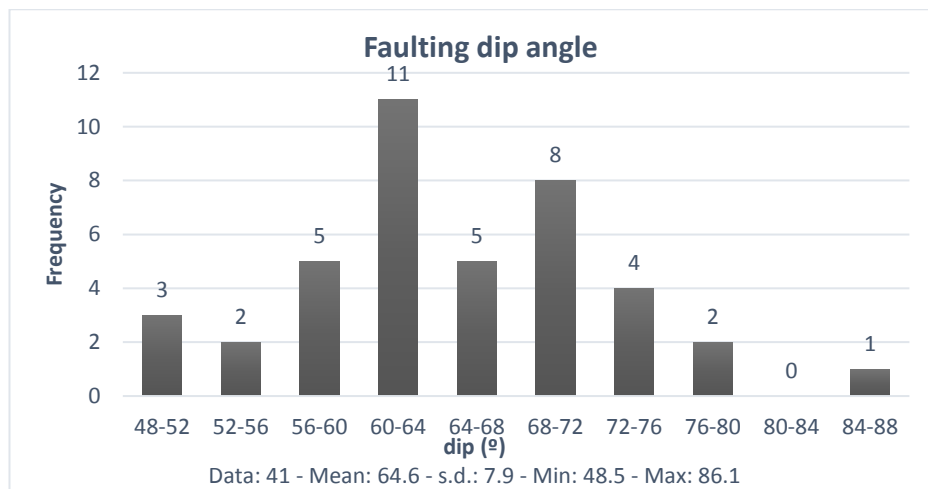
From the histogram of jointing persistence (Figure 51), a decrease of the frequencies when the exposed trace length rises can be seen, which suggests a right-skewed distribution of the data. The range of the data is 6.12 m, and the mode is located at the interval 0.3-0.9 m. Hence, based on the standard discontinuity persistence categories (ISRM, 1978), 121 joints have very low (<1m) persistence, while most of the data (~206 joints) represent low persistence (1-3m). This give an indication of the size of the blocks prone to slide if they are frictionally unstable.

Figure 51: Histogram of jointing persistence

4.2.1.2 Faults

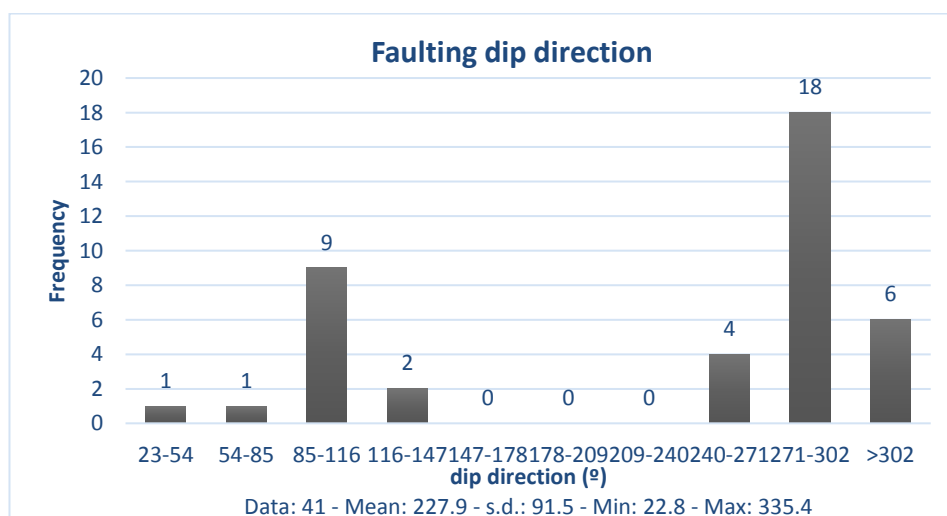
The histogram of the dip angle of faults (Figure 52) shows a clustering of the data around the average dip (64.6°). A range of 40° can be seen, and the mode is located in the interval 60° - 64° , which corresponds to the set 19 of faults shown on stereonet (see Chapter 4.3.1). 34 faults have lower dip than the interval that include the mean dip of the cliff face (76°), and thus, these faults can slide if they meet the rest of the geometric criteria for planar sliding.

Figure 52: Histogram of faulting dip angle



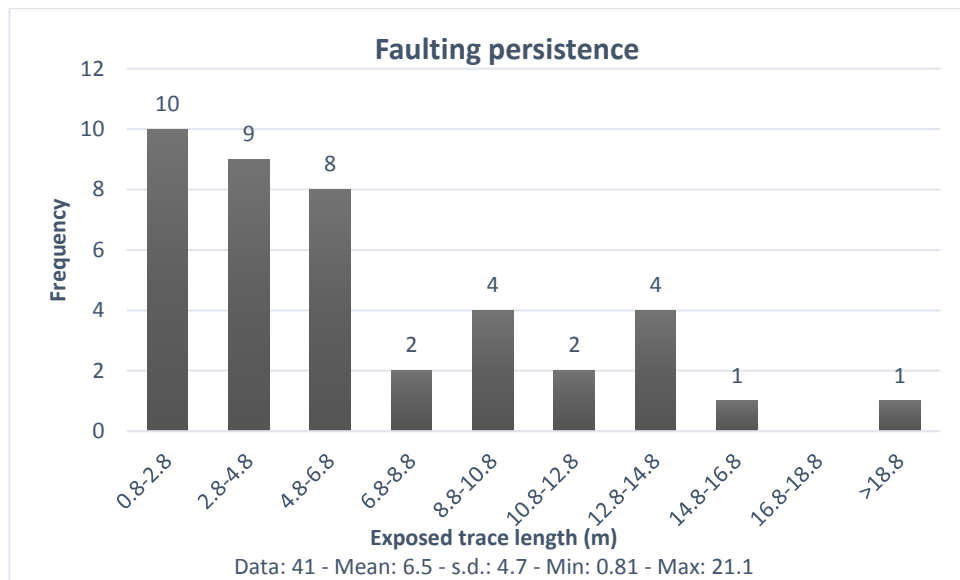
Regarding the frequencies of faulting dip direction (Figure 53), two opposite directions can be seen. The first is clustered within the interval 85° - 116° , that is, in the NW quadrant of the stereogram, while the second is located around the interval 271° - 302° (quadrant ESE), which corresponds to the aforementioned set of 19 faults (Figures 58-59).

Figure 53: Histogram of faulting dip direction



The shape of the histogram of faulting persistence (Figure 54) tends to show a right-skewed distribution of the data, with the mode located in the interval 0.8-2.8m (i.e. low persistence). In comparison with the jointing persistence, the shape of the graph suggests a similar pattern. However, according to ISRM (1978), 23 faults are characterized by medium persistence (3-10m). Moreover, there is an outlier of 21.1 m.

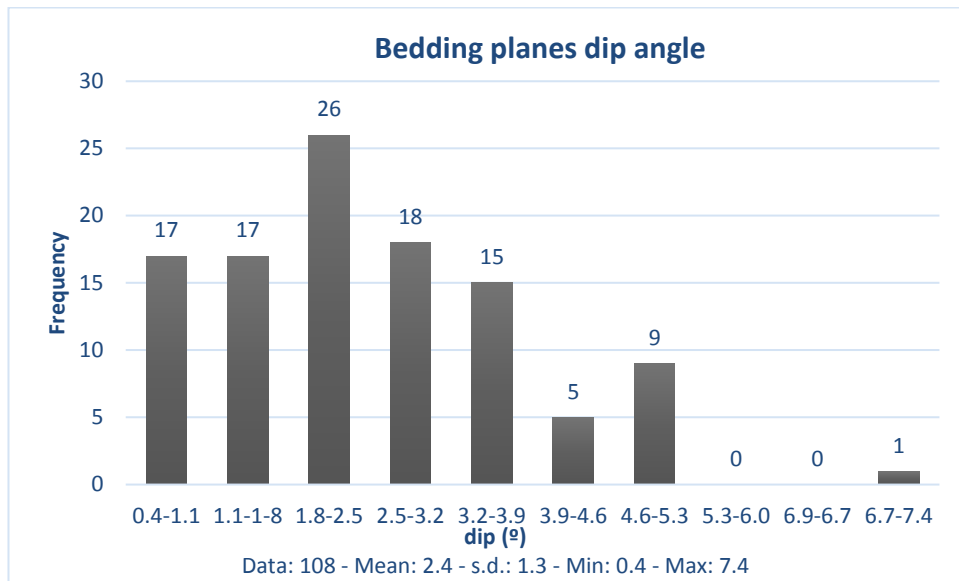
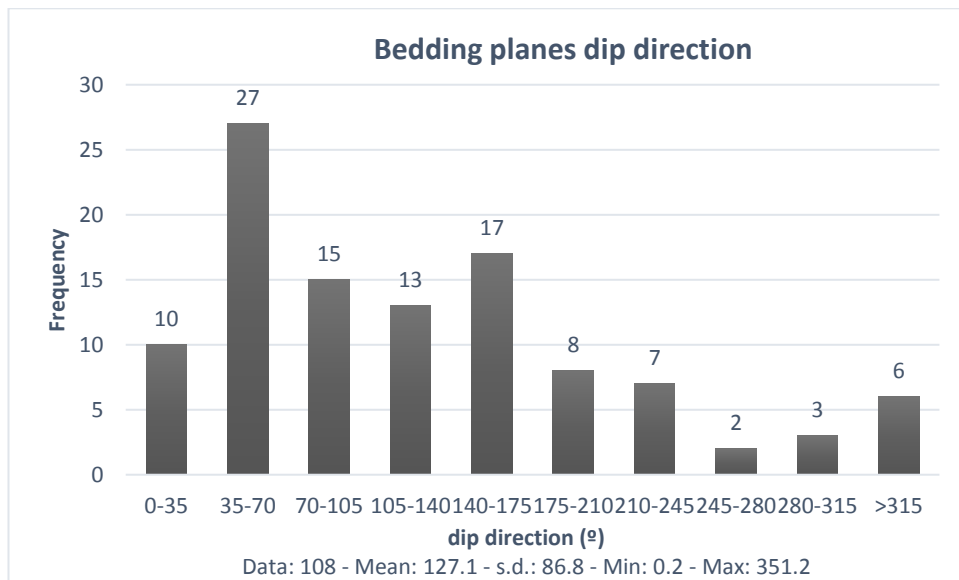
Figure 54: Histogram of faulting persistence



4.2.1.3 Bedding Planes

Contrary to the case of joints, the histogram of dip for bedding planes (Figure 55) suggests a right-skewed distribution of the data, since most of the data shows low dip angles. This is expected, if it is considered that bedding planes in the study area are near-horizontal. The mode is located within the interval 1.8° - 2.5° , which also includes the mean of the data. The range is 7° ; however, this must be taken with caution, since there is an outlier of 7.4° , which is representative of inclined BP located near faulting structures. Otherwise, the range would be around 4.9° .

The frequencies associated with BP dip direction (Figure 56) tend to show a heterogeneous distribution, since the mode is located within the interval 35° - 70° , the mean is included within the interval 105° - 140° , and there is a wide range of the data (351°). These suggest that bedding planes dip in almost all directions, and that they do not match with most of the dip directions of joints and faults, which is demonstrated in the general stereogram (Figure 68).

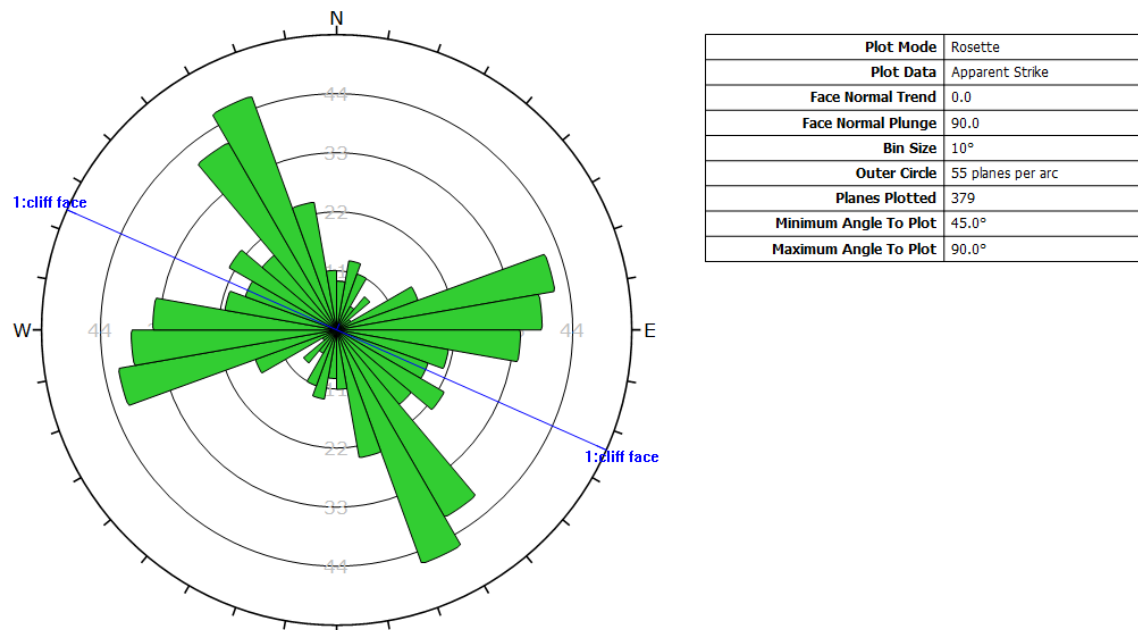
Figure 55: Histogram of bedding planes dip angle**Figure 56: Histogram of bedding planes dip direction**

4.3 KINEMATIC ANALYSIS

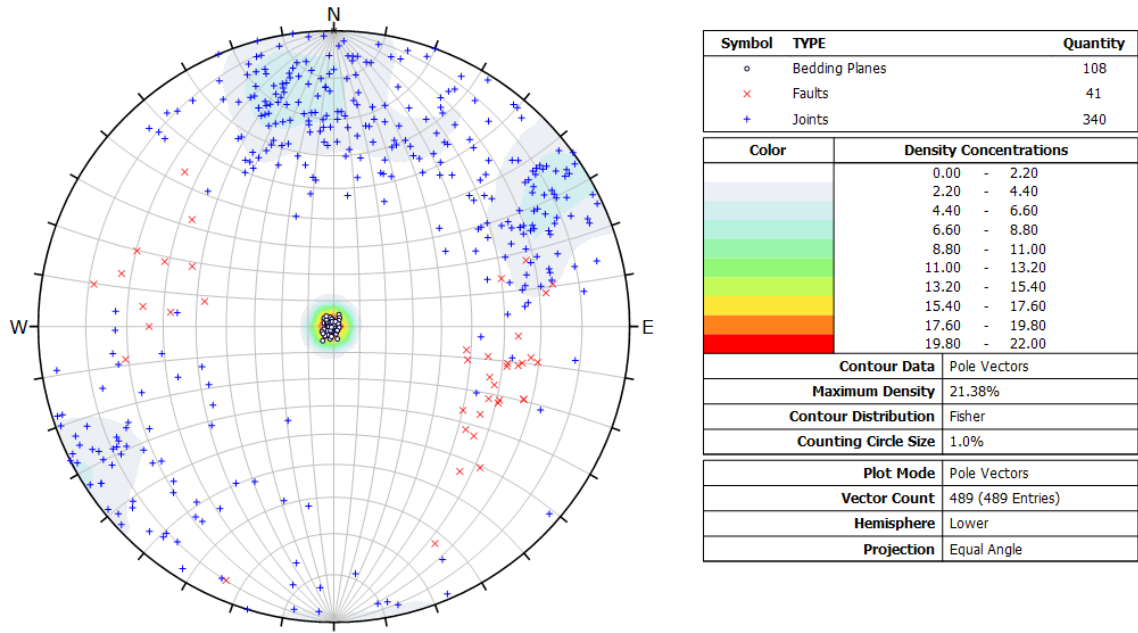
4.3.1 Stereonet assessment

Via a rosette diagram, the discontinuity orientation (undifferentiated) of the Telscombe cliffs is illustrated in Figure 57. The cliff face strikes at 114° (or dip direction = 204°), which means that it matches the fracturing direction of the East Sussex coastline, that is, WNW/ESE (Duperret et al., 2012). In this structural scenario, two general sets of discontinuities can be established: *a*) a discontinuity system orientated \sim ENE/WSW, with an average strike of about 80° (dip direction = 170°); and, *b*) an opposite/oblique discontinuity system orientated NNW-SSE, with an average strike of about 150° (dip direction = 240°). Considering all measurements taken in Brighton Marina, Peacehaven and Newhaven, the orientation of *a*) and *b*) tend to match those reported by Lemos de Oliveira (2013).

Figure 57: Rosette diagram of the cliff face and orientation all discontinuities



The general stereonet assessment and kinematic analysis were analysed using the equal angle (Wolff) equatorial projection on the lower hemisphere, and including the poles and contour plots of the 489 mapped discontinuities (using dip and dip direction as global orientation format). Also, discontinuities have been differentiated by type (faults, joints and bedding planes) and quantity (Figure 58).

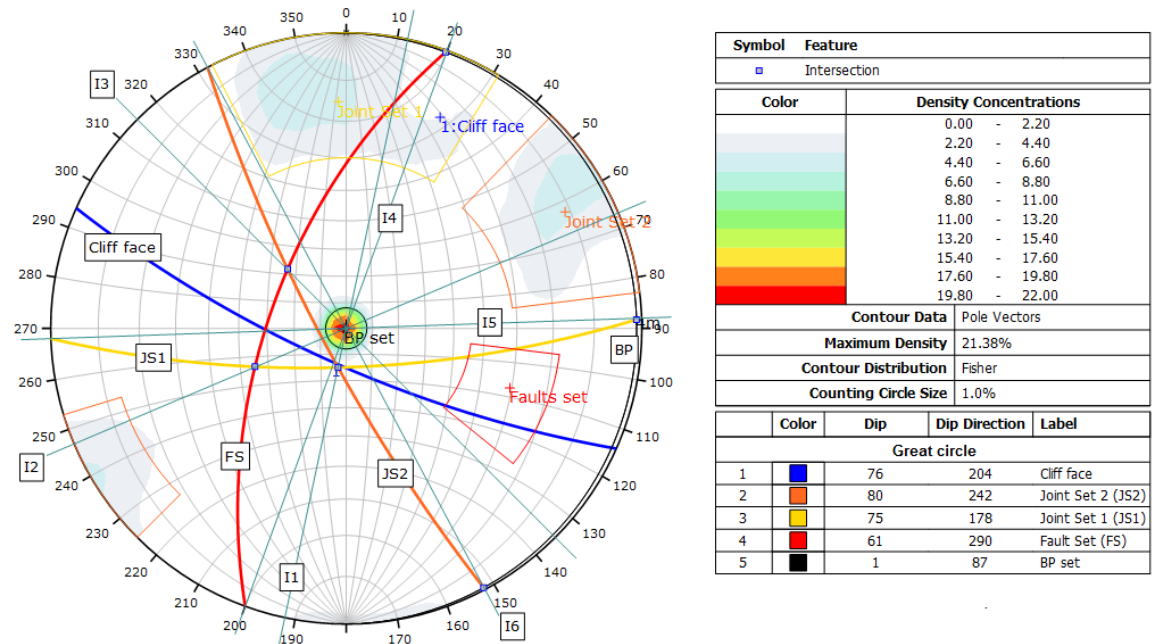
Figure 58: Stereographic projection with pole and contour plots

On the stereographic projection two clusters of joints can be seen (Figure 58). The first is concentrated towards the NNW quadrant of the stereogram (JS1 = 142 joints), while the second is located in the ENE-WSW quadrants (JS2 = 104 joints). Both have density concentrations ranging from 2.2 to 6.6%, hence representing two evident sets of principal joints. The remaining pole plots of joints show more scatter and are distributed preferentially towards the perimeter of the aforementioned sets. Faults show relatively more scatter since they do not lie within any interval of density concentrations. However, based solely on pole plot distribution, a clustering in direction ESE, forming a set of 19 faults (SF) may be seen. Most of the remaining faults are sparse and located in quadrant NW. In contrast, bedding planes exhibit the highest density concentration (8-22%), since all of the measurements are clustered in the centre of the stereograms. They form a cluster of 108 BP.

Based on the density concentration of each set of discontinuities and by fitting a dips set window tool around their contour plots, Figure 59 was obtained, which depicts the great circles associated with the different set of discontinuities, the great circle of the cliff face (ψ_{fi}) and the intersections between them (I_n). The direction of the great circles that represents both sets of joints (JS1=178° and JS2=242°) corresponds to the dominating orientation of discontinuities shown in the rosette diagram. Significantly, JS1 and JS2 are conjugate systems of master-joints that create pyramidal cliff profiles at the study site. The great circle representing the set of faults (SF) is 61°/290°, while BP is 1°/87°.

Additionally, the characteristics of the principal systems of intersections between great circles representing the main sets of discontinuities are summarized in Table 11.

Figure 59: Great circles of discontinuities, cliff face and lines of intersections (I_n)



Great circle representing the cliff face and those forming the possible kinematic wedge are highlighted.

Table 11: Characteristics of intersections between sets of discontinuities

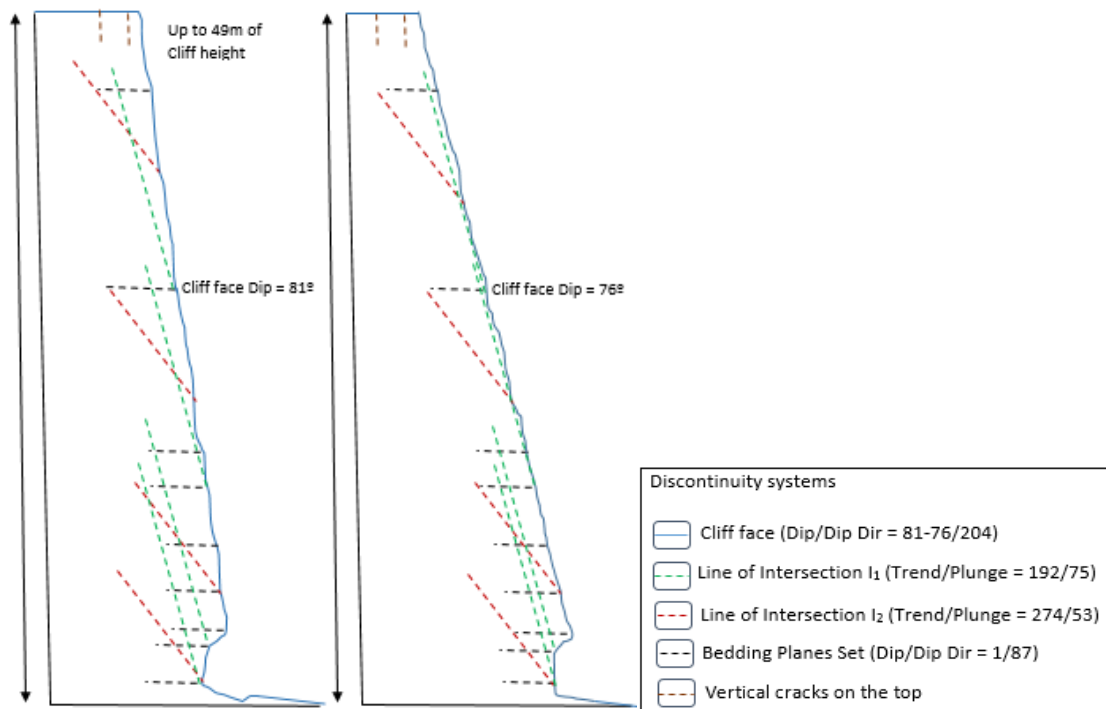
Line of Intersection (I_n)	Angle between Great circles ($^\circ$)	Trend/Plunge ($^\circ$)	Type of Intersection	Possibility of slope instability
I_1	117	192/75	Oblique	Wedge
I_2	78.9	247/53	Oblique	Wedge
I_3	131.3	315/58	Oblique	No
I_4	61.9	20/0	Oblique	No
I_5	75	88/1	Oblique	No
I_6	80.9	152/0	Oblique	No

By examining Figure 59 and Table 11, it can be seen that JS1 has a great circle with dip/dip direction of $75^\circ/178^\circ$, while JS2 reports $80^\circ/242^\circ$. They intersect at a wider oblique angle (117°), marginally outside the great circle of the cliff face, since the cliff face dips at 76° , while the plunge of the line of intersection (I_1) dips at 75° (i.e. $\psi_{fi} > \psi_i$). This means that JS1 and JS2 together could form a wedge failure that would slide in the direction of the trend of I_1 (192°). The great circle of JS1 intersects with the great circle of SF ($61^\circ/290^\circ$) at an acute angle (78.9°), outside the great circle of ψ_{fi} . In this case, the trend and the plunge of the line of intersection (I_2) is $247^\circ/53^\circ$, which means a higher possibility of wedge instability ($76^\circ > 53^\circ$), if they are frictionally unstable and if the cohesion of rock

bridges along joints are neglected. However, since the angle between planes JS1 and JS2 is higher than the angle formed between JS1 and SF, an open v/s a narrow wedge could be expected, respectively for both systems of discontinuities (Hoek and Bray, 1981). The plane of JS2 ($80^\circ/242^\circ$) intersects the plane of SF at a wider oblique angle (131.3°), but inside the great circle of ψ_{fi} . Consequently, since the trend of the line of intersection (I_3) is 315° , which dips inside the cliff face, there is no possibility of wedge instability between both sets.

Finally, the great circle of BP is the shallowest (1°), dipping toward the east of the stereogram at 87° . This great circle tends to intersect SF, JS1 and JS2 at acute oblique angles (61.9° , 75° and 80.9° , respectively). However, since the trend of the line of intersections between BP-SF (I_4) and BP-JS1 (I_5) lie inside the cliff face (at 20° and 88° , respectively), any wedge formed by BP and SF or JS1 is unlikely to slide. In contrast, the trend of the line of intersection between BP and JS2 (I_6) is 152° , that is, outside the cliff face. Nonetheless, due to the almost horizontal dip of BP, an effective kinematic failure of this wedge is not possible.

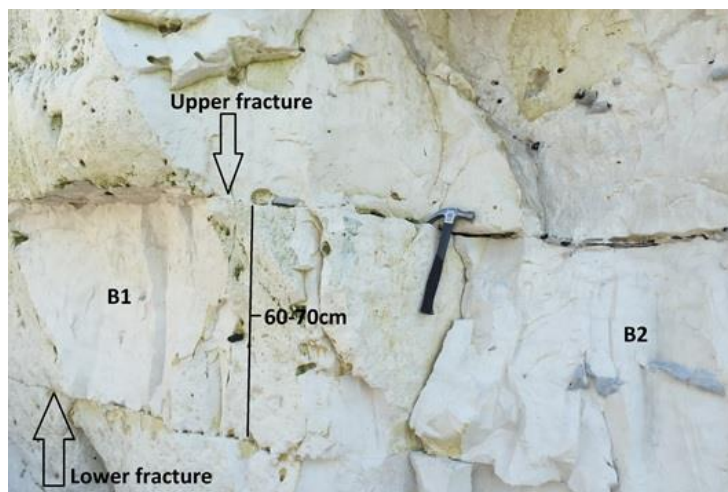
Figure 60: 2-dimensional modelling (not to scale) of the cliff face, I_1 and I_2 .



Derived from the aforementioned stereograms, Figure 60 shows the geometrical relationship between the cliff face, I_1 , I_2 and BP (2-dimensional). Here, I_1 and I_2 daylight on the cliff face ($\psi_{fi} > \psi_i$) can be seen, not only in cliff sections dominated by the average cliff face dip (76°), but also in sections with maximum dip (80° - 81°). However, in the first

scenario (76°), intersections dominated by I_1 are almost parallel to the cliff face, and hence they are more unstable in the cliff sections in which marine erosion is more intense, so that intersection type I_1 daylight is at the bottom of the cliff. On the other hand, I_2 dips at a flatter angle than the face, representing more hazard of wedge for the entire cliff length. Due to the horizontal and in some places sub-horizontal dip of BP, it can be deduced from Figure 60 that the size of the blocks prone to slide are controlled by the persistence of the potential slip planes in combination with the BP spacing. Vertical cracks are also controlling the instability at the top of Telscombe cliffs, in a similar way to the Seven Sisters type of cliff failure detailed by Mortimore et al. (2004a), but on a smaller scale. Geomorphological field-evidence of this is shown in Figures 61 and 62.

Figure 61: Fractures filled with layers of flints controlling chalk prone to slide



B1 and B2 represent fresh surfaces of Chalk blocks detached between fieldworks dates: 24/08/2016 and 17/09/2012. Two sub-horizontal discontinuities filled with flints conform the boundaries of the detached block, which is a common pattern in the study area.

Figure 62: Progressive opening of tension-cracks, sub-parallel to the cliff face



Left image: 10 cm wide and 70 cm long; Right image: 10 cm wide and 80-90 cm high.

4.3.2 General kinematic analysis

4.3.2.1 Planar sliding

The kinematic analysis for planar sliding was investigated using all 489 mapped discontinuities, the distribution of the sets on the stereonet, the friction cone of 35° , and the daylight envelope region (crescent shaded zone), whose external boundary is determined by the pole of the cliff face (Figure, 63). The model indicates that planar failure within the study site is kinematically possible, since 40 out of 489 discontinuities lie inside the daylight envelope region. However, the percentage of unfavourable poles of planar sliding for the entire cliff length is low (8%). Furthermore, the model suggests that 28 joints belonging to JS1 could slide, since this set daylights in the cliff face at an angle steeper than the friction angle but lower than the average dip of the cliff face. The remaining 12 joints that daylight within the hazard region do not belong to any set. These results correspond with rock mechanics literature, since planar instability is rare in rock slopes because it is infrequent that all the failure criteria needed to produce planar instability occur at the same time (Hoek and Bray, 1981). Here, the cliff face dip direction (and/or joints sets direction) is the main geometric criteria that restricts a higher possibility of planar instability, since its direction does not match with the mean direction of JS1 and JS2. That is, if the cliff direction had had a direction of about 175° or 245° , most of the JS1 and JS2 would lie in the critical region for planar instability to occur.

Figure 63: Stereographic model of kinematic analysis for planar sliding

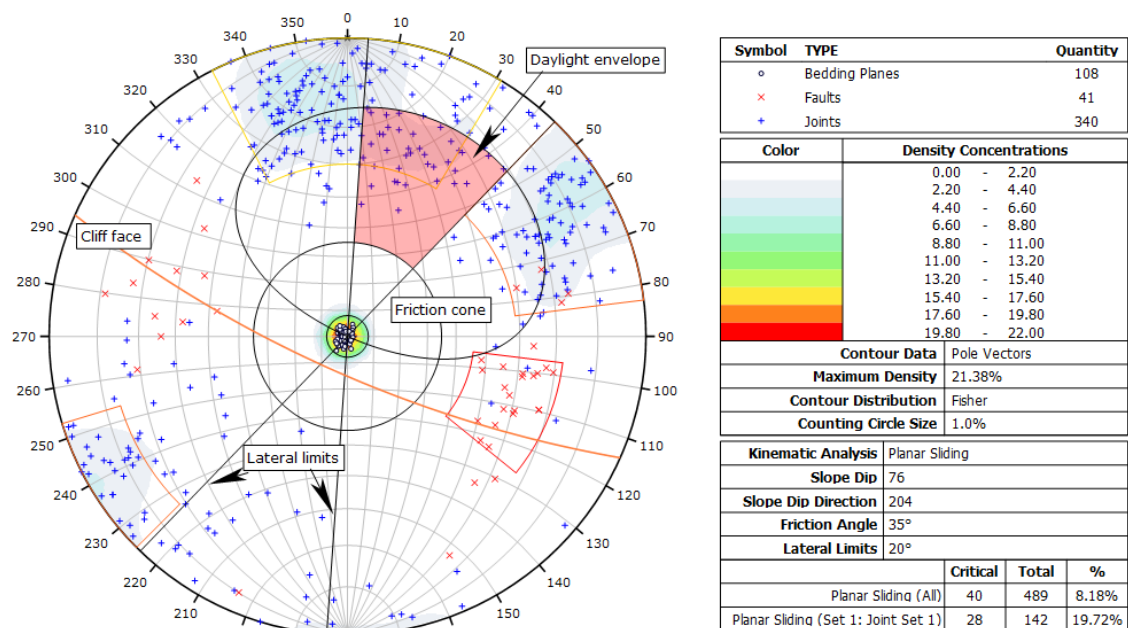
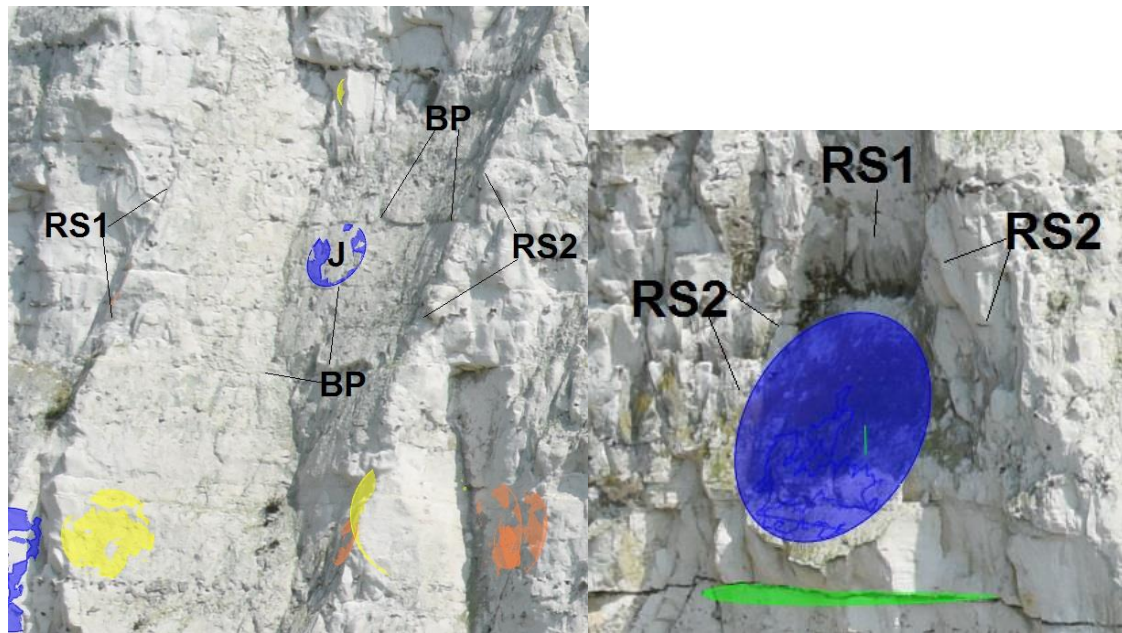


Figure 64, illustrates two actual joints from which planar sliding is likely to occur based on the stereographic model. Although planar sliding release surfaces are not explicitly modelled in the codes of the utilized software (Rocscience, 2016b), the ground-truth indicates that there are release planes on the cliff face able to provide low resistance to sliding.

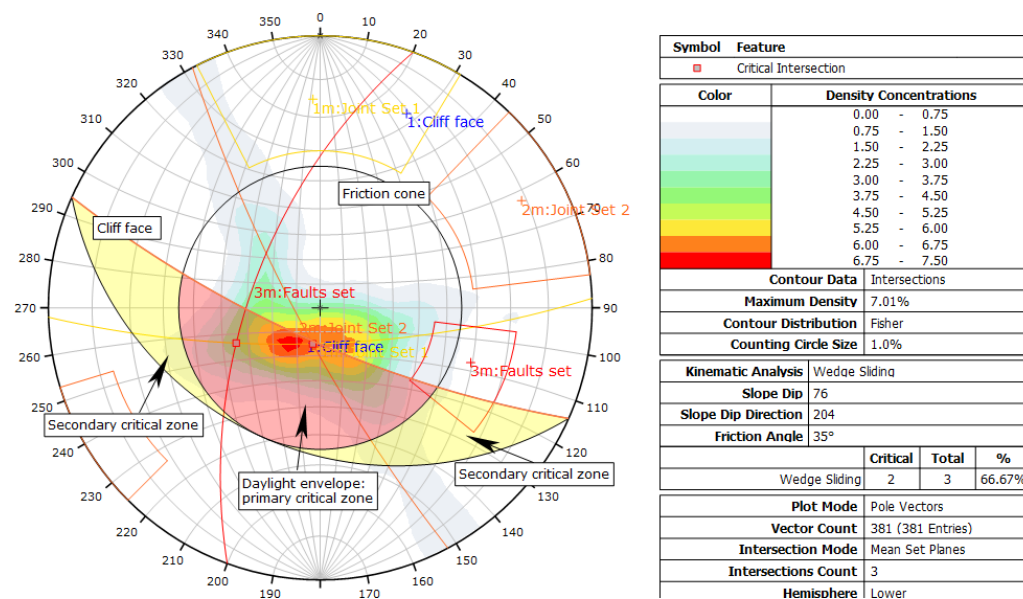
Figure 64: Examples of two actual joints prone to slide



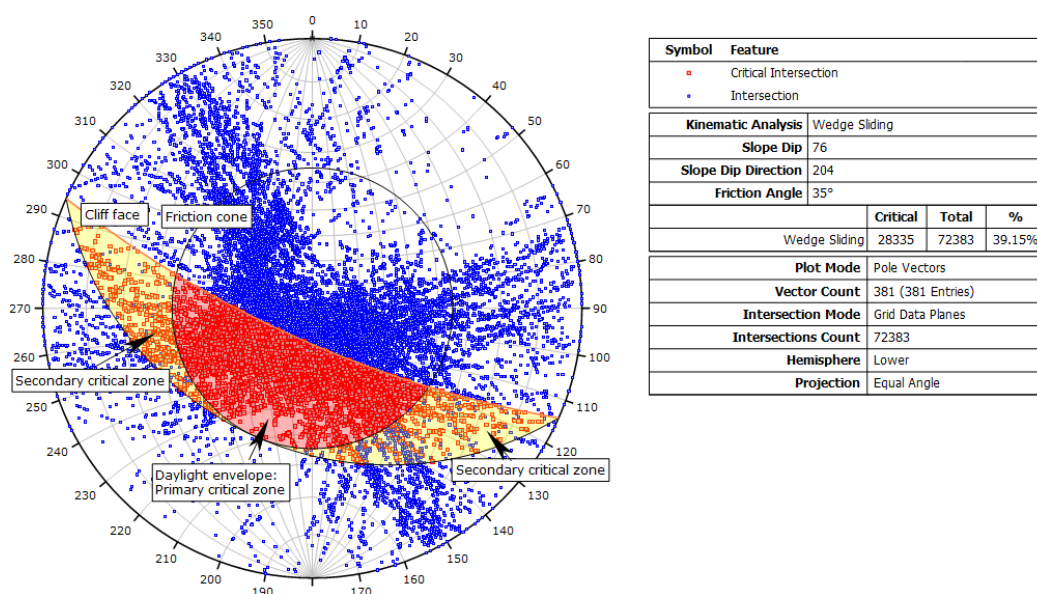
Left: Joint (J) with dip/dip direction = $73^{\circ}/212^{\circ}$; Right: Joint with dip/dip direction = $64^{\circ}/215^{\circ}$. According to the model, both joints are located within the critical zone for planar failure. Moreover, both have lateral release surfaces (RS) that permit sliding. In the right image, the disks representing JS1 (yellow) and JS2 (orange) acts as RS as well. Bedding Planes (BP), constrain the size of the blocks prone to slide.

4.3.2.2 Wedge sliding

Figure 65 shows the intersections of great circles that belong to sets of discontinuities that showed the possibility of wedge instability in the general stereonet assessment (Figure 59 and Table 11). Also, this mode of failure was investigated including the density concentration of all intersections between joints and faults, the friction cone of 35° (measured from the equator of the stereonet to its centre), and the primary and secondary envelope region for wedge failure to occur. First, it is noticed that I_1 and I_2 lie within the primary critical region of wedge failure. Furthermore, these intersections correspond with the maximum density concentration of intersections contours (4-8%), which lie within the daylight envelope region as well.

Figure 65: Critical intersections and contours of density concentrations

Furthermore, the kinematic analysis of wedge failure was analysed including all possible critical and non-critical intersections of joints and faults, the friction cone and both envelope regions (Figure 66). The results show that 18,758 (25.9%) intersections out of 72,383 possible intersections lie within the primary daylight envelope region (sliding in both planes). Moreover, 9,577 intersections (13.2%) lie within the secondary critical envelope (sliding on a single plane), and so a total of 39.1% of all possible intersections are favourable to wedge failure. Overall, these stereonet show that the line of the critical intersections dips out of the cliff face at a steeper angle than the friction angle ($\phi = 35^\circ$), but at a shallower angle than the average cliff face ($\psi_{fi} = 76^\circ$), thus, wedge sliding could occur.

Figure 66: Critical and non-critical intersections associated with wedge failure

To illustrate, Figure 67 presents an example of this failure mechanism involving JS1 and JS2. The left (yellow) disk represents JS1 ($72^{\circ}/181^{\circ}$), while the right (orange) disk depicts JS2 ($68^{\circ}/240^{\circ}$). As illustrated, JS1 and JS2 are representative surfaces of two intersecting master-joints dipping out of the cliff face, which are located in section 4 of the cliff (dip/dip direction = $80^{\circ}/199^{\circ}$). The specific kinematic analysis of these discontinuities is shown in Figure 68. It is evident that the great circles of JS1-JS2 intersect inside the primary critical zone (sliding on both joints) for wedge failure. The line of intersection dips at 67° , and the model suggests a direction of sliding of 221° .

Figure 67: Telscombe cliff face formed by two intersecting planes

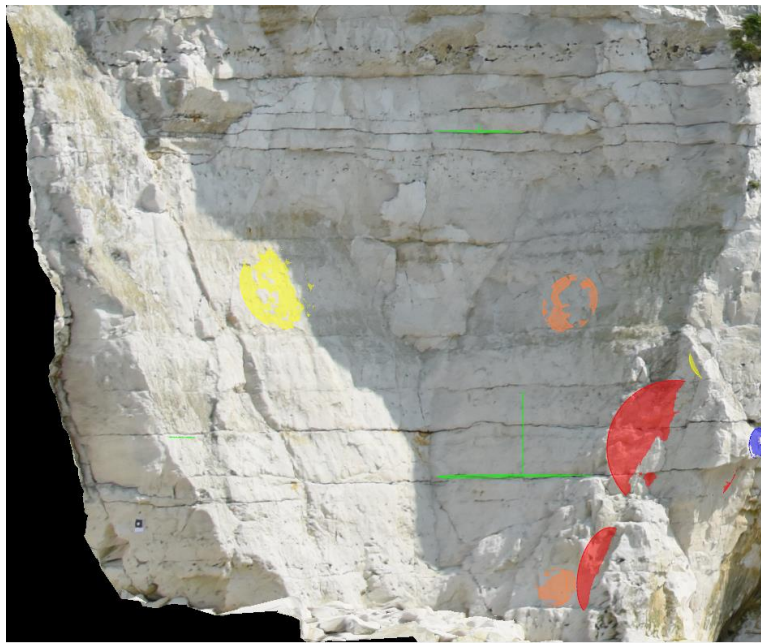
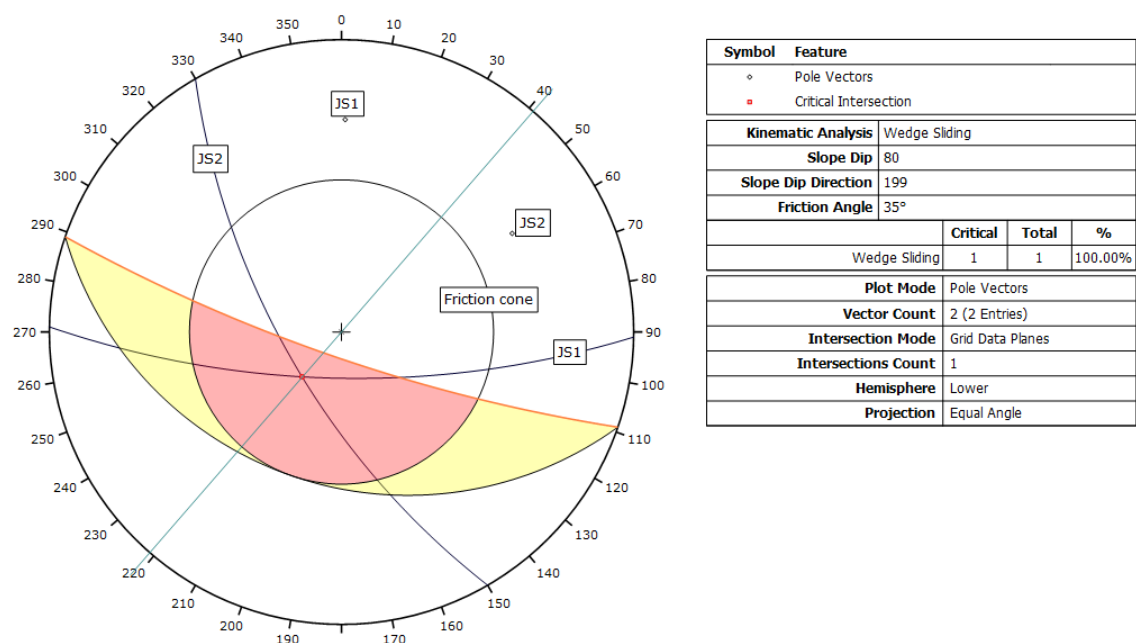


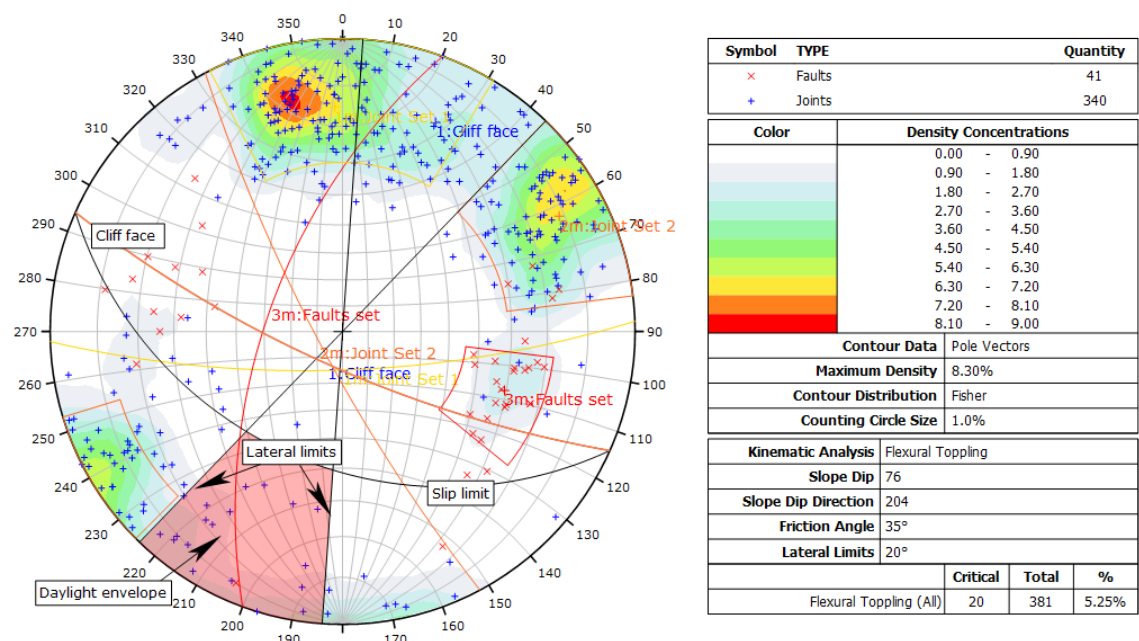
Figure 68: Kinematic Analysis of JS1 = $72^{\circ}/181^{\circ}$ and JS2 = $68^{\circ}/240^{\circ}$



4.3.2.3 Flexural toppling

The kinematic analysis for flexural toppling was modelled using the poles corresponding to all joints and faults and their related density concentration. The great circle representing the slip limit was determined by subtracting the friction angle value (35°) from the mean cliff face angle (76°), which resulted in a slip limit of 41° . Results are favourable with respect to this kind of slope failure. However, the percentage of favourable poles for flexural instability to occur is low (5%), since from 20 out of 381 discontinuities, 19 of them are represented by joints, meet all the failure criteria (Figure 69). Further, no discontinuity belonging to a specific set is located in the hazard region. Indeed, by examining Figure 69, the dip direction of these 20 discontinuities lie in opposite directions with respect to the dip of the cliff face. Also, their dip overcome the slip limit, and it is accomplished that the dip of the potential discontinuities is greater than 90° minus the mean dip of the cliff face (76°), plus the friction angle (35°), which is the condition for inter-layer slip to take place (Section 3.4.1.3). However, at this point, these results should be treated with caution, since no clear evidence of continuous columns of chalk dipping into the cliff face and breaking in flexure were detected during fieldwork and imagery inspection. Moreover, complementing the stereographic analysis, a block shape test is required to accurately assess the possibility of toppling (Hoek and Bray, 1981). This test is difficult to apply in the study site, since this not only requires the height of the potential blocks, but also the width towards inside the cliff face, which is difficult to measure because no lateral outcrop of inter-layer is exposed.

Figure 69: Kinematic analysis for flexural toppling



4.3.2.4. Direct toppling

The kinematic analysis for direct toppling was modelled using the points of intersection between joints, faults and bedding planes (Figure 70). The results indicate that this mode of failure is unlikely to occur in the study site, since 0.5% of all possible intersections meet the geometrical conditions. For oblique toppling this percentage increases to 7%. In some sections of the study area, joints and/or faults act as discontinuity surfaces whose intersections dip into the slope face, which permit the creation of the discrete rock blocks; and bedding planes act as sub-horizontal planes that conform the base of the toppling block. Discrete chalk blocks are preferentially located at the top of Telscombe cliffs, which have been favoured due to the presence of the Culver Chalk and its vertical fracture pattern. However, BP are near-horizontal, providing low dip angle to slide along its base (Figure 71). In addition, a block shape test is required to accurately assess this mode of failure (Hoek and Bray, 1981).

Figure 70: Kinematic analysis for direct toppling

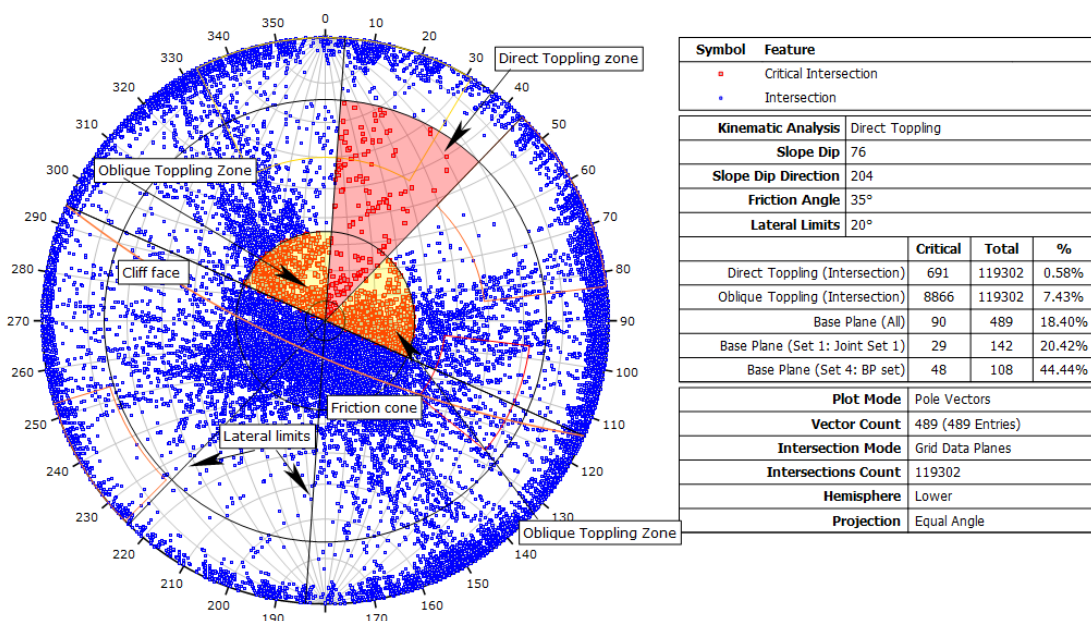


Figure 71: Blocks formed by orthogonal joints, with horizontal BP at the base



4.3.3 Kinematic analysis of cliff sections

The findings from the general kinematic analysis for the entire site confirm that wedge and planar sliding (Peacehaven type of failure) are the dominant types of failures. These results correspond with the literature, since these modes of failure are typical and also the major geohazard that characterizes the Newhaven Chalk between Newhaven and Brighton (Ove Arup and Partners, 1984; Mortimore et al., 2004a). As a result, a kinematic analysis was undertaken for the five representative sub-sections of the study site to determine the spatial variability in the percentages associated with wedge and planar failure. To accomplish this, the cliff was divided based on the homogeneous dip and dip direction values of the cliff face. The stereograms related to each section are shown in Figure 72.

The results of the kinematic analysis of the cliff section are further explored in Table 12. Evidently, wedge failure, as noted earlier, is the most likely mode of failure across all sections. However, the percentage of critical intersections and poles varies along the cliff length. Sections 1, 2 and 5, are less likely to fail because of wedge failure (28-37%), due to the lower cliff elevation in these sections (29 to 39m) in conjunction with the protection at the cliff toe, where marine energy is dissipated, and waves arrive to the cliff base with less frequency, since there are notches but they are less developed in terms of their lateral distance, height and depth (Table 9). Notably, the results of the kinematic analysis agree with the findings of Mortimore et al. (2004a) that Peacehaven failures can occur in cliff lines irrespective of the level of protection. It is important to note that sections 1 and 5 correspond with the most weathered sections of the cliff face nearing the dry valleys (Figure 72), and so that there were fewer chalk surfaces to be mapped and prone to slide, yielding to an estimated density of about 0.012-0.016 discontinuities per m², respectively.

Table 12: Percentages of critical intersections and poles by cliff section

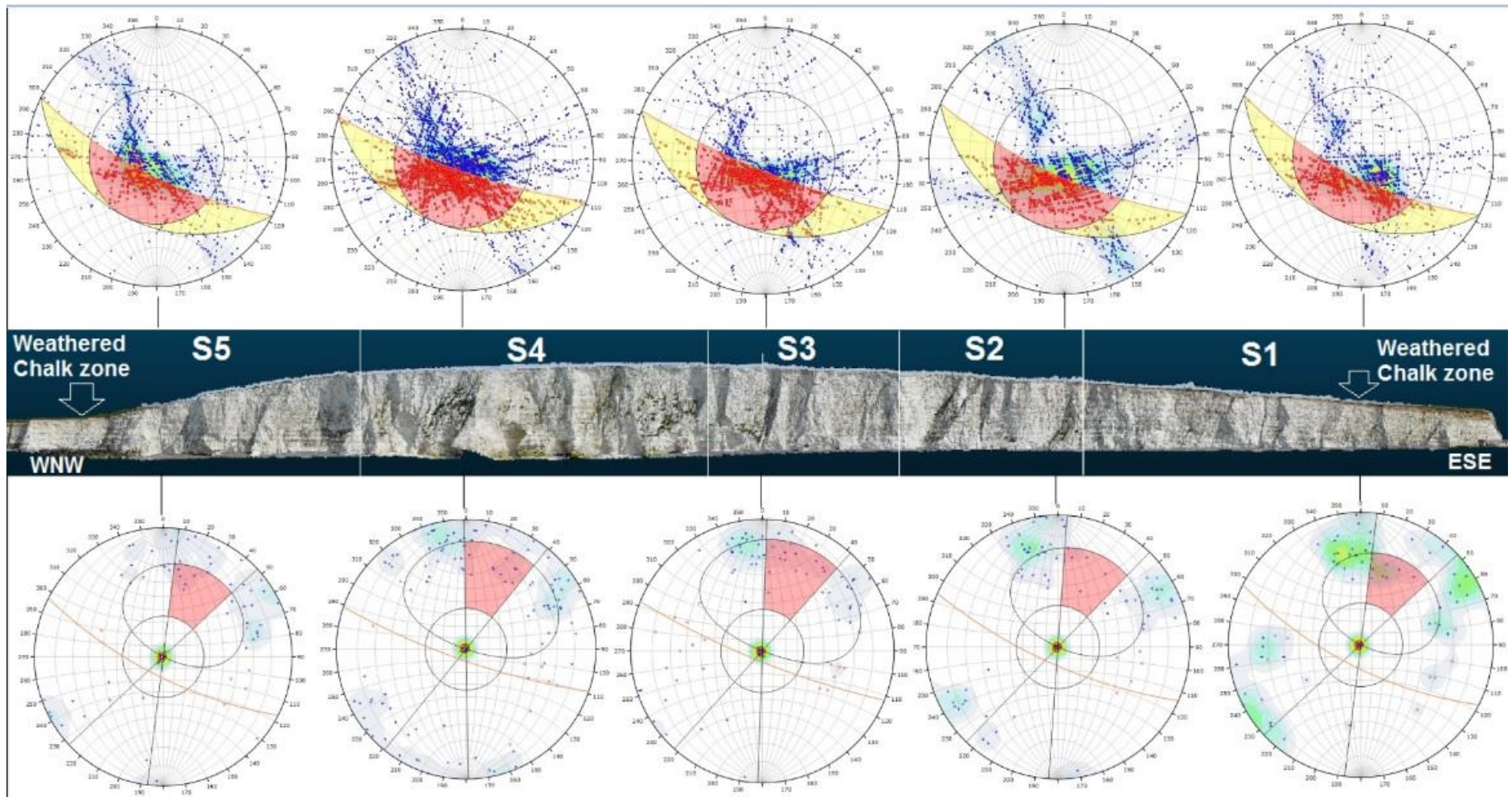
Cliff section (Dip/Dip Dir)	Wedge failure (%)	Planar failure (%)	Average height (m)	Length (m)	Area (m ²)	Number of discontinuities	Density discontinuities
1 (71/207)	36.2	11.3	29.5	198	5,841	71	0.012
2 (75/204)	37	5.7	39	87	3,393	87	0.025
3 (81/202)	54.2	12.2	43.3	106	4,589	107	0.023
4 (80/199)	41	8.5	43.2	183	7,905	142	0.018
5 (73/207)	28.7	6.1	30.6	166	5,079	82	0.016

In contrast, sections 3 and 4 show the highest percentages of favourable intersections and poles for wedges and planar failure to take place, which correspond with the tallest, average, sections of Telscombe cliffs (43m). Within these central sections of the study site there are more fresh chalk exposures that were digitised, resulting in an estimated density of about 0.023 and 0.018 discontinuities per m². It has been noted that the magnitude of failures of the Peacehaven type can be driven by cliff height (Mortimore et al., 2004a,b), which is also corroborated by the percentages of critical intersections. Importantly, these sections are the most exposed to wave attack (dip direction = 202° and 199°, respectively), which is illustrated by the increased concentration and size of notches (Table 9). These features contribute to increasing the instability, since breaking waves induce pressure variations that can propagate within the chalk mass if open sets of cracks transversely oriented to the cliff face are located at the cliff base (Brossard and Duperret., 2004). In sections 3 and 4 there is evidence of steeply conjugate discontinuities of JS1, JS2, faults and BP that frequently receive the impact of marine pressure pulses at the cliff base. As a result, the upper parts of these sections are more prone to fail along the mapped surfaces due to their own weight and lack of basal support.

To illustrate, between site visits on 17/08/2016 and 24/08/2016 a rock failure had occurred in Section 3 of the cliff (Figure 73). This failure coincided with a two-day period (20/08-21/08/2016) of strong winds, which were driven from the south west (orientation of the cliff) averaging 8.45ms⁻¹, with average and peak gusts of 11.29ms⁻¹ (25.25 mph) and 19.2ms⁻¹, respectively recorded at the nearby Brighton Marina meteorological station. The maximum high tides for this period were recorded between 6.3 and 6.9m (Chart Datum) at Brighton Marina, confirming substantial wave attack at the cliff base.

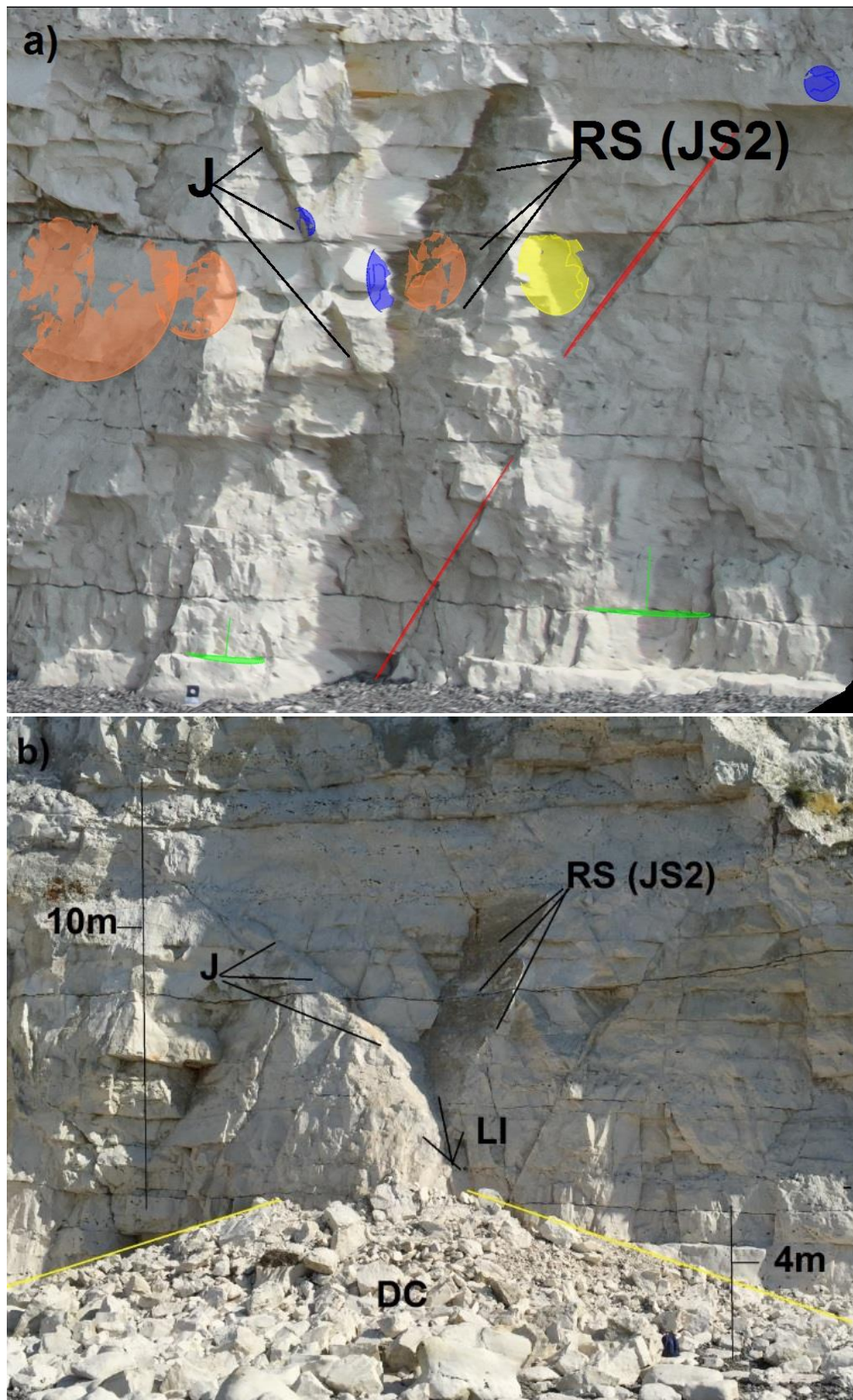
Figure 73a, identifies the discontinuity set which led to the wedge failure (UAV survey of 23/06/2016). To the left of the image, the discontinuity “J” (blue disk) is a joint that does not belong to either identified set, a dip and dip direction of 69°/71° were measured for this plane. To the right, the orange disk represents a joint of set 2 (JS2), and had a dip/dip direction of 78.5°/233.4°. The joints intersect towards the toe of the cliff and are limited at the top by harder bands of nodular flint. From Figure 73b, it is inferred that J and JS2 failed in wedge, but JS2 acted as a release surface (RS), since the sliding chalk took place along the surface of J. Between both joints, there is the line of intersection (LI), from which the mass of rock was spread, forming a debris cone of ~4m of high and ~25 of wide. The failure had a height, and run-out of ~10 m.

Figure 72: Kinematic analysis by cliff section



Stereonets: at the top represent wedge instability; at the bottom planar instability.

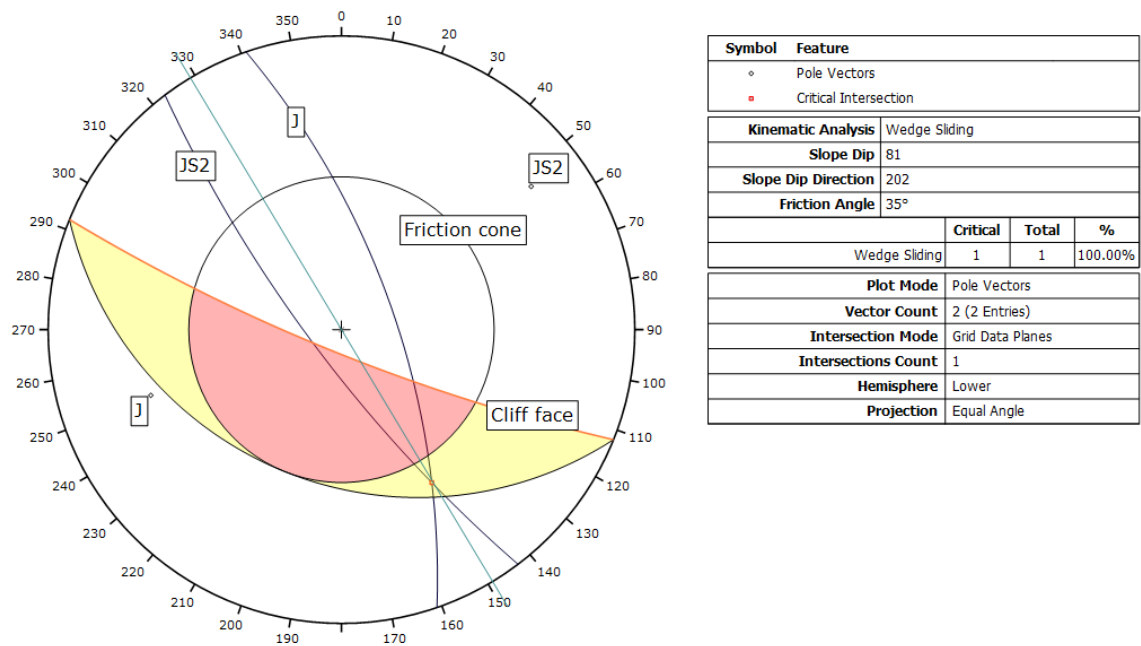
Figure 73: Wedge failure produced between site visits



a) Digital model showing mapped discontinuities before failure (UAV survey of 23/06/2016)
 b) Photographic register of 24/08/2016 after failure.

A kinematic analysis of the wedge failure was undertaken (Figure 74), which is one of the 28335 out of 72383 intersections shown in the stereogram of the general wedge assessment (Figure 66). Results indicate that the two great circles intersect at the secondary critical zone. This confirms the ground-truth, since the wedge took place on one discontinuity plane, which means that these models are able to identify accurately potential sliding surfaces for the study site. Here the model shows a trend/plunge of the line of intersection of $149^{\circ}/28^{\circ}$.

Figure 74: Kinematic Analysis of wedge failure produced between site inspection



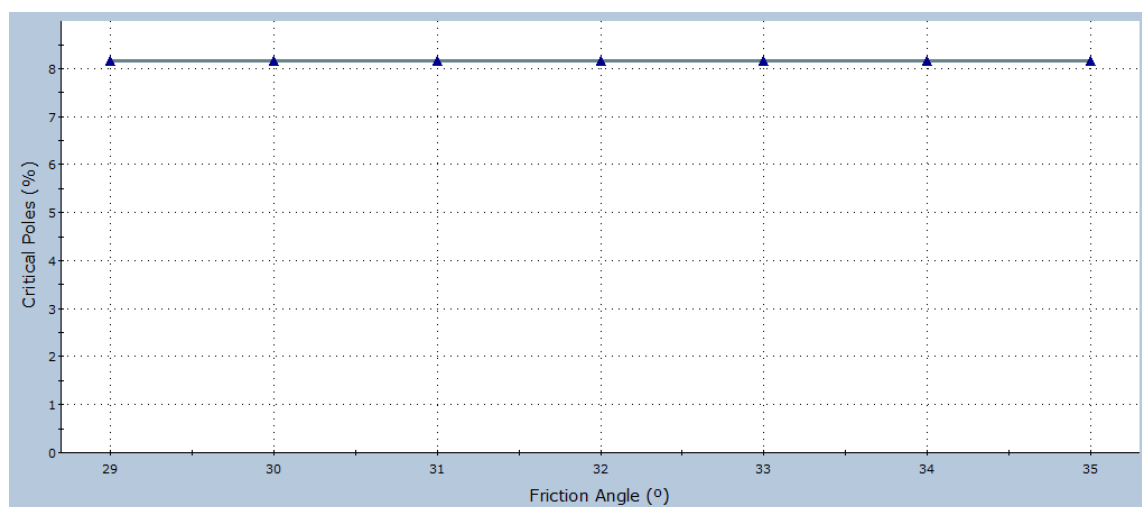
Overall, the kinematic analysis by cliff section suggests that there are higher percentages of favourable attitude of discontinuities for wedge and planar failures towards the centre of the study site. These percentages match with the highest cliff sections and the active geomorphological zones in terms of their exposition to marine erosion. Also, that there are less blocks prone to slide in zones of disintegrated and decolorized chalk.

4.3.4 Kinematic sensitivity analysis

The kinematic sensitivity analysis (KSA) was undertaken to assess the influence of the friction angle (ϕ) on the different modes of slope instability, by varying the chalk ϕ from 29° to 35° (Barton, 1973; Jaeger and Cook, 1976; Arup and Partners (1984); Mott MacDonald, 2009; Taibi et al., 2009; Bedjaoui et al., 2010), while the mean dip of the cliff face and dip direction remained constant at 76° and 204° respectively, as well as retaining the lateral limits (20°) for wedge, planar and flexural toppling. Each of the following graphs show the change of critical poles or intersections (%) with respect to the increment of ϕ .

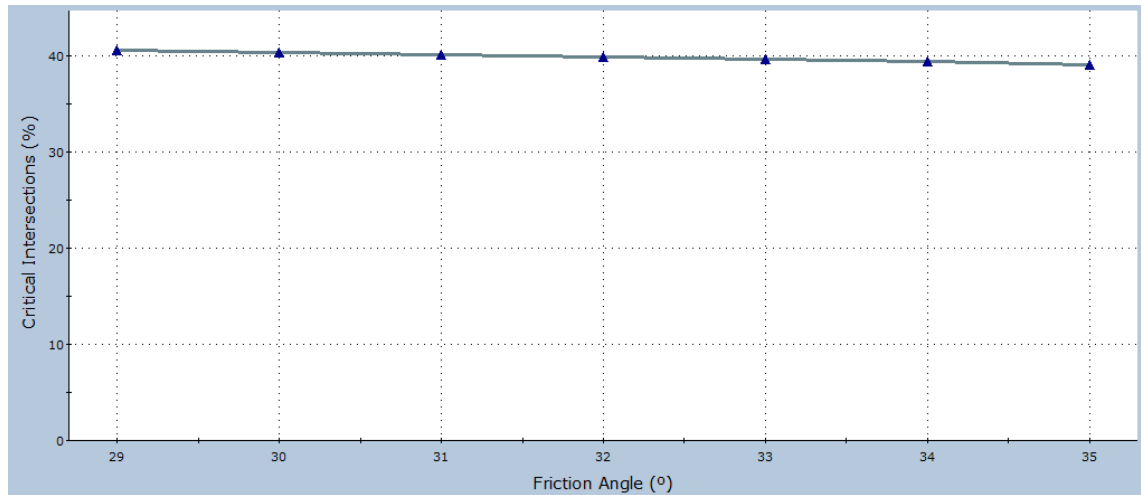
For planar sliding there was no variation in the number of critical poles, holding the percentage in 8%, with a decrease in ϕ from 35 to 29° (Figure 75). This is explained by examining the actual attitude of the discontinuities within the study site and the orientation and boundaries of the daylight envelope region, since no poles are distributed between 35 and 29° on the stereonet (Figure 63). Similarly, an assessment was undertaken to determine the friction angle at which planar failure would increase significantly. By analysing the general kinematic analysis for planar failure (Figure 63), the nearest pole on the daylight envelope zone (counting from the centre to the perimeter) has a dip of 48° . As a result, it would be necessary to change ϕ to 49° to detect a new change in the percentage of critical poles. The last is almost unfeasible, since high friction rock masses (e.g. basalt, granite, limestone) exhibit maximum ϕ of about 45° (Barton, 1973; Jaeger and Cook, 1976; Selby, 1993).

Figure 75: Critical percentages v/s ϕ of planar sliding



For the case of wedge failure, there is a slight variation in the number of critical intersections with reduction of the friction angle (Figure 76). On this occasion, the increase in percentage of intersections prone to sliding rises from 39 to 40%, with 1,063 (out of 72,383) critical intersections overcoming their respective critical angles.

Figure 76: Critical percentages v/s ϕ of wedge sliding



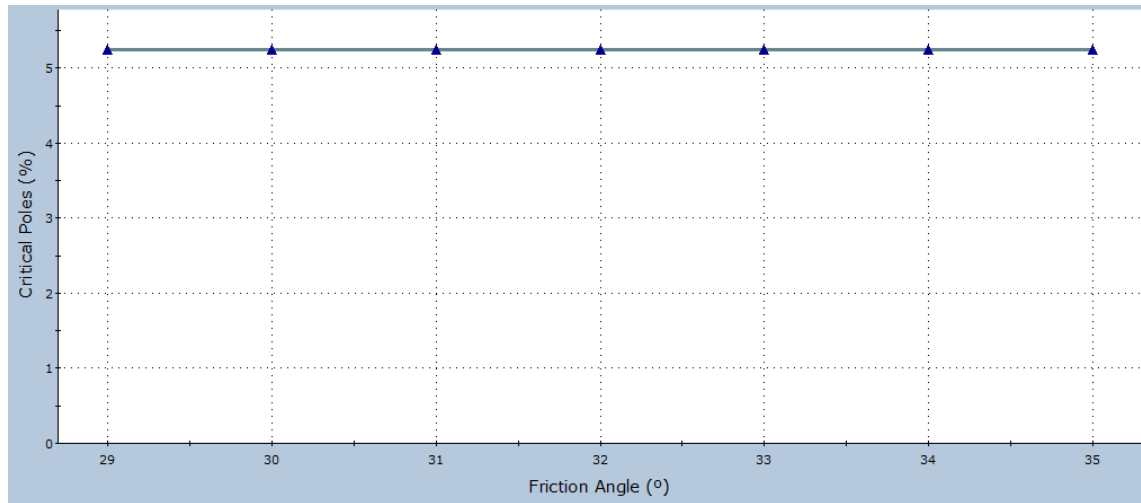
For flexural toppling, if ϕ is varied from 35° to 29° no change is observed (Figure 77). This is because the line of the normals to the potential planes of flexural failure ($90 - \beta$) shown on the critical region of the stereonet are lower than the cliff face dip (ψ) minus the friction angle (slip limit), so that a decrease in ϕ (e.g. 29°) will move the slip limit towards the centre of the stereonet instead of its perimeter, which is the area of poles with higher dip angles for the study site (see Figure 69 of general flexural toppling).

By testing the model, a $\phi = 47^\circ$ it would be necessary to create a decrease in the critical number of poles inside the daylight envelope zone (i.e. moving the slip limit toward the perimeter of the net), which is unfeasible considering even the maximum friction angle of higher rock masses. By contrast, a $\phi = 24^\circ$ would be needed to increase the hazard of flexural instability by only one intersection.

No kinematic sensitivity analysis for direct toppling was applied, since its daylight envelope area is solely defined by the slope face cone and the lateral boundaries. Hence, no change is detected by varying ϕ . This is because the kinematic failure criteria of this mode of instability is solely related to the geometry of the rock mass, rather than geometrical conditions and strength parameters, such as friction angle (Hudson and Harrison, 2000). However, this mode of toppling is more likely to occur if basal planes dip out of the slope face, but such a condition is not needed. In fact, if the dip of the basal

planes is less than ϕ , the sliding will not take place in association with direct toppling (Hudson and Harrison, 2000).

Figure 77: Critical percentages v/s ϕ of flexural toppling



Overall, these outputs show that the behaviour of the models is not sensitive to variations with respect to the considered range of friction angle, since no changes in the percentages of poles for planar (0%) and flexural failure (0%), and minimal variations for the case of intersections compromising wedge instability (1%) were detected. Therefore, the results determine that by using a ϕ of 35° for all the kinematic analysis executed, an accurate depictions of the potential modes of slope failure were depicted.

5. DISCUSSION

5.1. THE SELECTION CRITERIA USED FOR MAPPING DISCONTINUITY SURFACES

When assessing large unstable slope faces for rock slope characterization purposes but with limited time, making the measurement of all discontinuities unfeasible, it is strongly recommended to focus the mapping on the attitude of main joint sets, and trace lengths as well as other discontinuity proprieties relative to the slope stability (Tuckey and Stead, 2016). The UAV survey, photogrammetric planning and digital manual mapping of discontinuities were designed to meet these criteria. Furthermore, the selection of criteria such as truncation lengths or the identification of joints exhibiting fresh and smooth surfaces (see section 3.3) are methodological approaches that contribute to rapid mapping and reducing the subjectivity when selecting discontinuities (Tuckey and Stead, 2016; Barlow et al., 2017).

An important point is that individual joints can be selected for mapping on the basis of professional experience and judgment, similar to utilizing a traditional compass clinometer approach in the field (Haneberg, 2008). The virtual mapping environment provided by techniques such as UAV photogrammetry and terrestrial laser scanner, allows for a previous unrealistic amount of collaboration between project team members (Haneberg, 2008). Additionally, to reduce the subjectivity component related to the identification of discontinuities whether using photogrammetric models, TLS models, mapping windows or scanline survey, the criteria suggested by Haneberg (2008) and Martino and Mazzanti (2014) were adopted, which recommend that the mapping should be performed by two researchers to reduce subjectivity in the selection of major joint sets. For example, joints can be carefully inspected, which was also performed by rotating the 3D model to obtain different angular views of the same discontinuity.

On the other hand, although automatized methods for detection and mapping discontinuity surfaces have gradually been used (Hadjigeorgiou et al., 2003; Lato and Vöge, 2012), they have two principal limitations: a) the need to validate automatically identified surfaces and traces to check for accuracy; and b) the propensity for automatized approaches to underestimate the degree of fracturing within the rock mass (Tuckey and Stead, 2016). Hence, to date, even automatized detection of discontinuities requires professional skilled interpretation by at least two geoscientists to get a representative statistical sample of discontinuities. To illustrate, Martino and Mazzanti (2014) performed an automatized detection of joints using the Split-FX software.

However, the automatic surface detection was based on user-defined thresholds and contrasted with patches selected by the operator initially and then the outputs of the detection were validated. Even photogrammetric software such as 3D Analyst mine mapping suite have tools for automatized identification of joints but still require human supervision and analysis.

Field-based discontinuity data obtained along scanlines or windows need a large enough slope area to be mapped in order to get a statistically significant sample (Sturzenegger and Stead, 2009b). Also, it is suggested that mapping of different exposures is needed to avoid orientation bias (ISRM, 1978; Priest 1993; Sturzenegger and Stead, 2009b). Within this context, according to Haneberg (2008), an argument can be made that discontinuity attitudes obtained from 3D models, whether using TLS or digital photogrammetry, are more representative because they take into account and quantify the variability of irregular discontinuity surfaces in a way that manual measurements rarely can (Cronin, 2008). Consequently, remote sensing surveys should cover a large outcrop surface to provide statistically significant datasets and sampling of the higher elevation of an outcrop, so specific hazardous joints located higher on the slope can be measured, providing a comprehensive and representative dataset for analysis (Sturzenegger and Stead, 2009a).

Therefore, although in this research not all outcropping discontinuities at Telscombe cliffs were mapped, it is believed that the aforementioned and selected sets of criteria used for mapping provided a representative dataset, reducing the subjectivity related to the selection of discontinuities due to fact that: a) a large enough cliff face area was used, providing more data than if a scanline technique along the cliff toe had been used or by mapping on a virtual window located at specific sections of the cliff face; b) along the cliff face different exposures were mapped as recommended by Priest (1993) and Sturzenegger and Stead (2009b); c) the natural variability of irregular discontinuities was taken into account as suggested by Cronin (2008); d) higher risky joints which are prone to slide were measured, which would be impossible to map using traditional methods along the cliff base; e) other geoscientist supervised the mapping at different stages to reduce as much as possible the subjectivity selection of discontinuities as recommended by Haneberg (2008) and Martino and Mazzanti (2014); and f), by careful inspection of different joints exposures from different angular views. These sets of criteria were fully optimized due to the advantages provided by a remote sensing technique for data collection.

5.2 THE CAPABILITY OF UAV PHOTOGRAMMETRY FOR THE MEASUREMENT OF PROPERTIES OF DISCONTINUITIES RELATIVE TO SLOPE STABILITY

Remote sensing techniques, such as digital photogrammetry and terrestrial laser scanning, are being progressively utilized as complementary methods to traditional scanline and window mapping approaches for discontinuity characterization (Sturzenegger and Stead, 2009a). For instance, Salvini et al. (2013) performed a spatial modelling of joints using digital terrestrial photogrammetry. By applying this technique, they could obtain accurate data related to the position, orientation, spacing and persistence of discontinuities, in addition to determining block shape. Sturzenegger and Stead (2009a,b) demonstrated the capacity of combining close-range terrestrial digital photogrammetry and TLS for measuring discontinuity location, orientation and roughness. They also examined truncation bias associated with image pixel resolution for measuring the persistence of joints. Discontinuity attitude, persistence, fracture intensity and rock bridge intensity have been investigated by Tuckey and Stead (2006), using a combination of field mapping and digital photogrammetry. Discontinuity roughness has been studied by Fardin et al. (2004), Haneberg (2007) and Poropat (2008) utilizing both digital photogrammetry and TLS.

As noted in the Results Chapter (section 4) of this research, discontinuity location, dip, dip direction and trace length as a proxy measure of persistence were obtained to examine frequency distributions of discontinuities and to perform a kinematic analysis. However, additional properties relative to cliff stability that also could have been measured using the obtained DTMs from the UAV are spacing, roughness and block shape. These properties could have been mapped mainly due to the high pixel resolution and accuracy of the 3D models (RMSE = 0.25 pixels), in addition to the red-green-blue bands (RGB) information that allowed interpretation of the white chalk surface and cliff morphology, but also due to the strong network geometry achieved and the accuracy of the absolute orientation (see properties of Tables 7 and 8). To illustrate, by zooming the models shown in Figures 54-57, the perpendicular distance between adjacent conjugate and sub-vertical joints can be estimated. This can be performed using both windows or scanline mapping along defined cliff sections. Similarly, blocks shape length, width and height could have been measured in a similar way as the notch geometry along the cliff base was measured (see section 4.1). The measurement of discontinuity roughness could have been performed but with further research to investigate, selecting and applying a methodological approach and criteria, as for example, proposed by Sturzenegger and Stead (2009a).

Properties such as aperture, filling and small scale roughness are nowadays less amenable to achieve using remote sensing techniques. Unless the aperture is sufficiently wide, the pixel resolution of conventional DTMs will be of restricted use. This is also true for infill characterization (Sturzenegger and Stead, 2009a). These methodological limitations are reinforced by the results of this research, as the resolution of the obtained 3D models did not allow for the detection of aperture, filling and small size roughness. However, substantial potential exists for the use of DTMs obtained from remote sensing measurements to visually estimate the occurrence and origin of seepage on rock slopes (Sturzenegger and Stead 2009a). Nonetheless, explicit seepage conditions in white masses of chalk outcropping at Telscombe also could not be detected. When using terrestrial digital photogrammetry for rock mass characterization, Roman and Johnson (2012) similarly concluded that digital photogrammetry may not permit the observation joint infilling, aperture and weathering conditions.

According to Haneberg (2008), neither terrestrial digital photogrammetry nor TLS provide quantitative data about rock type, joint filling, or in situ rock quality. However, digital photogrammetry has the potential to provide some information about rock types and their degree of weathering. Martino and Mazzanti (2014) and Sturzenegger and Stead (2009a) concluded that to undertake a rock slope stability analysis mechanical parameters are requested that cannot be provided by remote sensing measurements, therefore a combined approach integrating direct and remote sensing methods is needed to provide a comprehensive rock slope characterization. The 3D models resolution obtained in this research also support the idea that traditional methods and UAV photogrammetry can be best used to complement each other when measuring properties of discontinuities relatives to sea cliff stability.

5.3 THE RELATIVE PERFORMANCE OF DIGITAL PHOTOGRAMMETRY AGAINST TLS AND DIRECT FIELD ASSESSMENT FOR MEASURING DIP AND DIP DIRECTION

Close-range digital photogrammetry and TLS can be utilized to investigate rock slope stability, overcoming issues such as complex slope morphology and inaccessibility of outcrops (Salvini et al., 2013), and principally in conditions where manual discontinuity measurements may be dangerous (Barlow et al., 2017). 3D slope face modelling and discontinuity mapping using either digital photogrammetry and TLS have been shown to

be efficient and useful approaches by several academic researchers, surface mine and civil projects (Haneberg, 2008). However, principal photogrammetric products are high-resolution 3D photogrammetric models that have advantages over TLS point clouds, such as equipment portability due to its heavy weight, cost and the capability to include discontinuities that appear as linear traces rather than flat planar surfaces (Haneberg, 2008). On the other hand, TLS laser pulse penetrates vegetation, it only one scanner position is required to collect data, and high point densities can be obtained (Kolecka, 2011). Nevertheless, both technologies are affected by problems such as reflective surfaces, surface roughness and wetness, and occlusion. The selection between both technologies depends mostly on the budget, time, equipment availability, user's experience and object shape/complexity or study site area (Kolecka, 2011). Within this context, another question arises about the relative performance between digital photogrammetry, TLS and traditional field scanline using compass-clinometer for rock mass assessment, especially in terms of the degree of statistical agreement when measuring properties such as dip and dip direction.

Salvini et al., (2013) demonstrated the high accuracy of digital photogrammetry with a camera mounted on a helicopter and TLS cloud points. Their results showed that mean discontinuity attitude values measured using photogrammetric models were similar to those using TLS models as differences smaller than 8° in dip and 4° in dip direction were detected. Also, their test demonstrated that digital photogrammetric absolute orientation and stereorestitution did not affect the accuracy of discontinuity measurements. Similarly, Haneberg (2008) performed a comparison between manually and photogrammetric models discontinuity measurements for 3-D rock slope modelling. Results showed good statistical agreement between both individual joints and entire sets of joints, in most cases with only $1\text{--}3^\circ$ of resultant difference between both methodological approaches, which is good when considering the range of imprecision that might be expected from the manually measured orientations (Cronin, 2008).

Furthermore, Martino and Mazzanti (2014) integrated TLS and direct geomechanical surveys using scanlines for sea cliff stability analysis. The comparison between joint set data derived from direct field-based measurements and TLS were quite similar, ranging from $0\text{--}10^\circ$ for dip angle, and $4\text{--}10^\circ$ in the case of dip direction. Sturzenegger and Stead (2009a) compared scanlines using compass clinometer measurements, TLS and digital photogrammetry approaches at the Murrin Lake, Mount Seymour, Manning Park and Lake Louise rock slope exposures in British Columbia. Stereonets obtained with these three approaches agree closely, especially in the case of systematically oriented joints.

Interestingly, maximum residuals of 4° and 8° for dip angle and dip direction were registered between all data collection approaches. According to the same authors, such accuracy is suggested to be acceptable for geotechnical studies, due to the natural variability of discontinuity attitude. Similarly, Sturzenegger and Stead (2009b) compared TLS modes at medium and high resolution against photogrammetric models using focal lengths of 50, 200 and 400 mm, at Turtle Mountain, Mount Edith Cavell, Bridal Veil Falls and Medicine lake rock slopes of British Columbia. The results obtained at varying resolutions showed very similar discontinuity sets on all stereonet. To illustrate, at Bridal Veil Falls, resultant differences ranged from about 0.1 to 6° for dip angle, and between 0.3 and 9° for dip direction.

Although in this research discontinuity measurements using scanline surveys with compass clinometer were not used due to risky conditions along Telscombe cliff base, some degree of statistical agreement for dip attitude can be expected using UAV photogrammetry, traditional scanline and TLS approaches, since the mapped structural features were consistent with results from other investigations that have been undertaken utilizing direct measurements in the field such as shown in Mortimore et al. (2004a). However, further research should be undertaken to investigate the degree of agreement of rock slope properties using different registration approaches at chalk sea cliffs. In this context, it should be considered that as discontinuities are never perfectly planar, a certain amount of statistical scatter in attitude measurements is to be expected (Anonymous, 1977). Consequently, Sturzenegger and Stead (2009a) state that dip and dip orientation values measured from compass clinometer are expected to be slightly different when compared with values obtained from remote sensing techniques. For these reasons, these authors suggest that remote sensing estimations of discontinuity attitude are possibly more realistic than discrete compass clinometer registrations made at arbitrary scanlines.

6. CONCLUSIONS

This research has demonstrated that UAV photogrammetry can create high-quality DTMs of a cliff face at an accuracy that permits the obtainment of structural geology data to be used for kinematic stability analysis, and with accuracies similar to those obtained using terrestrial photogrammetry. In addition, it has shown that the UAV platform offers a rapid method for data collection over a large coastal section (around 7 minutes of survey for around 750m of cliff line) and is a flexible platform from which it was possible to overcome constraints related to the height of the cliffs of the study site.

The use of an UAV was a safer method than using traditional scanline mapping methods for discontinuity characterization. Also, this allowed the obtainment of more rock slope assessment area for cliff stability analysis. To illustrate, only 24 discontinuities were mapped within 2 m of the cliff base such that about 95% would not have been recorded using manual measurement. Hence, the method not only can be used for difficult to access sites to mitigate safety risk, which is a key criteria governing commercial and research work, but also to support robust assessment and monitoring of cliff instability hazards.

Further research to improve the method and accuracy can be carried out regardless the 3D model due to inherent vibration suffered by the UAV during the flight, in combination with the use of fixed-camera focal lens (prime lens). This is suggested in order to analyse their possible influence on the photogrammetric parameters of the interior and exterior orientations, as well on the imagery alignment.

The cliff stability analysis indicated that the Newhaven Chalk cropping out at Telscombe shows highly inclined joints (mean = 75°), dipping out of the cliff face, which favour the presence of several unstable blocks, particularly when they daylight in the slope face at greater angles than the friction angle ($\phi = 35^\circ$). Two main sets of conjugate master-joints (JS1 and JS2) were found to create the possibility of wedge failure and generate pyramidal cliff profiles at this cliff section. They are characterized by great circles with dip and dip directions of $75^\circ/178^\circ$ and $80^\circ/242^\circ$, respectively.

The kinematic analysis revealed that wedge failure is by far the most likely mode of slope instability, since 39% of all possible joint intersections are favourable to wedge failure, and one of them occurred between successive data capture. Planar sliding is the second most probable mode of slope failure, comprising 8% of all mapped discontinuities. In contrast, flexural and direct toppling are not of concern, since their associated

percentages were found to be 5% (poles) and 0.5% (poles and intersections), respectively. Furthermore, by looking beyond the stereographic and statistical results, not enough structural evidence was found during site and imagery inspection for toppling failure. As defined by Mortimore et al. (2004a), the Newhaven Chalk is characterized by large wedge and planar modes of cliff failure, which is numerically supported by this research at the examined coastal section.

Notably, the findings obtained from the kinematic analysis per cliff section revealed that the tallest sections have the highest percentages of critical intersections for wedge failure, which corresponds with the zones of more intense basal erosion (illustrated by the increased frequency and size of lateral caves), providing a lack of basal support to the corresponding upper joints of these sections. According to Mortimore et al. (2004a), this morphological and geo structural configuration enables a progressive “bottom-up” working of the instability along the mapped shear surfaces. These configurations can result in differing rates of cliff retreat in a context of climate change due to the expected rise of sea level and storm surges.

Overall, these results indicate that the potential for wedge and planar failure is controlled by a combination of the rock mass geo-structural configuration (i.e. structurally controlled by the dip angle, its orientation, density concentration of discontinuities per cliff section, persistence, and cliff elevation) in interaction with their exposition to marine erosion (i.e. stress controlled).

Based on common geotechnical procedures to assess the stability of a slope, the proposed next step is to provide precise information about the factor of safety associated with wedge and planar failures for which cohesion and the friction angle can be measured and used to calculate the shear strength. After that, if necessary and/or economically feasible, the application of corresponding reinforcements to the study site.

Finally, these results are useful for coastal monitoring and its suitable management, since they provided further understanding and numerical data about potential modes of cliff failure for the Newhaven Chalk of East Sussex. Further, they provided a base line for engineering geological/geomorphological change detection at Telscombe cliffs, in addition to providing a methodological framework for its replication not only in coastal chalk cliffs but also for other structurally controlled cliffs subject to instability.

REFERENCES

ADAM Technology. (2004). 3DM Analyst 2.1 Trial at BMA Coal's Goonyella Mine. ADAM Technology. [http://www.ADAMtech.com.au/3dm/goonyella%20report%20\(abridged\).pdf](http://www.ADAMtech.com.au/3dm/goonyella%20report%20(abridged).pdf). Last accessed: 01/11/2016.

ADAM Technology (2006). Using 3DM Analyst Mine Mapping Suite for rock face characterization. ADAM Technology. <http://slideplayer.com/slide/4313823/>. Last accessed: 01/11/2016.

ADAM Technology. (2010). 3DM Analyst Mine Mapping Suite 2. 3D Measurement, Camera Calibration and Block Adjustment Software. User's Manual. ADAM technology, Australia.

Agouris, P., Doucette, P. Stefanidis, A. (2004). Automation and digital photogrammetric workstations. In: McGlone, J., Mikhail, E., Mullen, R. (Eds). Manual of Photogrammetry. American Society of Photogrammetry and Remote Sensing, Maryland.

Albertz, J., Kreiling, W. (1989). Photogrammetric Guide, Herbert Wichmann Verlag, Karlsruhe.

Aldiss, D., Farrant, A., Hopson, P. (2012). Geological mapping of the Late Cretaceous Chalk Group of southern England: a specialised application of landform interpretation. Proceedings of the Geologists' Association, 123 (5), 728-741.

Allen, E. (2010). Introduction to the imaging process. In: Allen, E., Triantaphillidou, S. (Eds). The Manual of Photography. 10th ed. Elsevier/Focal Press, Oxford.

Anonymous, 1977. The description of rock masses for engineering purposes. Working party report. Quarterly Journal Engineering Geology, 10, 355–388.

Awange, J. (2012). Environmental monitoring using GNSS, global navigation satellite system. Springer, Berlin. DOI: 10.1007/978-3-540-88256-5.

Awange, J., Kiema, J. B. K. (2013). Environmental geoinformatics: monitoring and management. Springer, Berlin. DOI: 10.1007/978-3-642-34085-7.

- Aydan, Ö., Kawamoto, T. (1990). Discontinuities and their effect on rock mass. In: Barton, N., Stephenson, O. (eds.). *Rock Joints*, 149-156. A.A. Balkema/Rotterdam/Brookfield, The Netherlands.
- Barlow, J., Gilham, J., Ibarra, I. (2017). Kinematic analysis of sea cliff stability using UAV photogrammetry. *International Journal of Remote Sensing*, 38 (8-10), 2464-2479.
- Barton, N. R. (1973) Review of a new shear strength criterion for rock joints. *Engineering Geology*, 7, 287–322.
- Bedjaoui, M.C. Allal, M.A., Duperret, A., Taibi, S., Rivoalen, E. (2010). Numerical Approach of the Littoral Instability of Chalk Cliffs: Case of Grandes Dalles (The Large Flagstones). *Jordan Journal of Civil Engineering*, 4(2), pp. 63-75.
- Beraldin, J. A. (2004). Integration of laser scanning and close-range photogrammetry—the last decade and beyond. *Proceedings: XXth International Society for Photogrammetry and Remote Sensing (ISPRS) Congress*, Istanbul, Turkey, July 12–23, pp. 972–983.
- Bilissi, E., Triantaphillidou, S., Allen, E. (2010). Exposure and image control. In: Allen, E., Triantaphillidou, S. (Eds.). *The Manual of Photography*. 10th ed. Elsevier/Focal Press, Oxford.
- Birch, J.S. (2006). Using 3DM Analyst mine mapping suite for rock face characterization. In: Tonon, F., Kottenstette, J. (Eds.), *Laser and Photogrammetric Methods for Rock Face Characterization*, ARMA, 13–32.
- Birch, J.S. (2009). 3DM Analyst Mine Mapping Suite Training. ADAM Technology. <http://slideplayer.com/slide/6869698/>. Last accessed: 01/11/2016.
- Bird, E. (2004). Cliff, coastal. In: Goudie, A. (Ed.). *Encyclopedia of Geomorphology*. Routledge, London.
- Boehler, W., Bordas, Vicent, M., Marbs, A. (2003). Investigating laser scanner accuracy. *Proceedings: XIXth CIPA Symposium*, Antalya, Sept. 30–Oct. 4.

Brossard, J., Duperret, A. (2004). Coastal Chalk cliff erosion: experimental investigation on the role of marine factors. In: Mortimore, R., and Duperret, A. (Eds.). Coastal Chalk Cliff Instability. Geological Society, London, Engineering Geology Special Publications, 20, 109-120.

Bundy, S. (2013). Geotechnical properties of chalk putties. PhD Thesis, University of Portsmouth, UK. <http://eprints.port.ac.uk/14841/> Last accessed: 06/09/2016.

Channel Coastal Observatory (CCO). (2015). Channel Coastal Observatory - Regional Coastal Monitoring Programmes Seaford Wave Buoy. http://www.channelcoast.org/data_management/real_time_data/charts/?chart=81. Last accessed: 01/05/2017.

Clifford, J. M., Förstner, W., Bernhard, W., Paderes F, Munjy, R. (2004). The mathematics of photogrammetry. In: McGlone, J., Mikhail, E., Mullen, R. (Eds). Manual of Photogrammetry. American Society of Photogrammetry and Remote Sensing, Maryland.

Davis, G. H. and Reynolds, S. J. (1996). Structural geology of rocks and regions, 2nd ed. John Wiley & Sons, New York.

De Freitas, M. (2009). Withdrawal of support by surface excavations. In: Price D, G. (Ed). Engineering Geology: principles and practices. Springer, Berlin, 250pp.

Dornbusch, U. (2015). Comment on: Lawrence, J., Mortimore, R., Stone, K., Busby, J., 2013. Sea saltwater weakening of chalk and the impact on cliff instability. *Geomorphology*, 231, 390-392.

Cronin, V. S. (2008). Finding the mean and 95 percent confidence interval of a set of strike-and-dip or lineation data. *Environmental & Engineering Geoscience*, 14(2), 113-119.

Duperret, A., Genter, A., Mortimore, R., Delacourt, B., De Pomerai, M. (2002). Coastal rock cliff erosion by collapse at Puys, France: the role of impervious marl seams within Chalk of NW Europe. *Journal of Coastal Research*, 18 (1), 52-61.

Duperret, A., Taibi, S., Mortimore, R., & Daigneault, M. (2005). Effect of groundwater and sea weathering cycles on the strength of Chalk rock from unstable coastal cliffs of NW France. *Engineering Geology*, 78 (3), 321-343.

Duperret, A., Vandycke, S., Mortimore, R. N., & Genter, A. (2012). How plate tectonics is recorded in chalk deposits along the eastern English Channel in Normandy (France) and Sussex (UK). *Tectonophysics*, 581, pp. 163-181.

Eberhardt, E. (2003). Rock slope stability analysis—utilization of advanced numerical techniques. *Earth and Ocean sciences at UBC*, Vancouver, Canada, 41pp.

Eisenbeiss, H. (2008). UAV photogrammetry in plant sciences and geology, In: 6th ARIDA Workshop on "Innovations in 3D Measurement, Modeling and Visualization, Povo (Trento), Italy.

Eisenbeiss, H. (2009). UAV Photogrammetry (Doctoral thesis). University of Technology Dresden, Zürich. http://www.igp-data.ethz.ch/berichte/Blaue_Berichte_PDF/105.pdf. Last accessed 5/01/2016.

El-Hakim, S.F., Beraldin, J.A. Blais, F. (2003). Critical factors and configurations for practical 3D image-based modeling. Proceedings: 6th Conference on 3D Measurement Techniques. Zurich, Switzerland, September 22–25.

Emery, K. O., Kuhn, G. G. (1982). Sea cliffs: their processes, profiles, and classification. *Geological Society of America Bulletin*, 93 (7), 644-654.

Fardin, N., Feng, Q., Stephansson, O. (2004). Application of a new in situ 3D laser scanner to study the scale effect on the rock joint surface roughness. *International Journal of Rock Mechanics and Mining Sciences* 41, 329–335.

Francioni, M., Salvini, R., Stead, D., Giovannini, R., Riccucci, S., Vanneschi, C., Gullì, D. (2015). An integrated remote sensing-GIS approach for the analysis of an open pit in the Carrara marble district, Italy: Slope stability assessment through kinematic and numerical methods. *Computers and Geotechnics*, 67, 381 pp. 46-62. DOI: 10.1016/j.compgeo.2015.02.009.

Goodman, R. E. (1989). *Introduction to Rock Mechanics*. John Wiley and Sons, New York.

Haarbrink RB, Eisenbeiss H. (2008). Accurate DSM production from unmanned helicopter systems. *International archives of photogrammetry, remote sensing and spatial information sciences*, vol. XXXVII/B1. Beijing: PRC; p. 159–64.

Hack, R. (2009). Geological masses. In: Price D, G. (Ed). *Engineering Geology: Principles and Practices*. Springer, Berlin, 250pp.

Hadjigeorgiou, J., Lemy, F., Cote, P., Maldague, X., (2003). An evaluation of image algorithms for constructing discontinuity trace maps. *Rock Mechanics and Rock Engineering*, 36 (2), 163–179.

Halcrow Group Ltd. (2002). Futurecoast. Technical report and interactive DVDs prepared for Defra.

Haneberg, W.C. (2007). Directional roughness profiles from three-dimensional photogrammetric or laser scanner point clouds. In: Eberhardt, E., Stead, D., Morrison, T. (Eds.), *Proceedings 1st Canada–U.S. Rock Mechanics Symposium*, Vancouver, May 27–31, 2007, pp. 101–106.

Haneberg, W. C. (2008). Using close range terrestrial digital photogrammetry for 3-D rock slope modeling and discontinuity mapping in the United States. *Bulletin of Engineering Geology and the Environment*, 67(4), 457-469.

Hoek, E. and Bray, J. (1981) *Rock Slope Engineering*, 3rd ed. Inst. Mining and Metallurgy, London, UK.

Honkavaara, E., Ahokas, E., Hyyppä, J., Jaakkola, J., Kaartinen, H., Kuittinen, R., Nurminen, K. (2006). Geometric test field calibration of digital photogrammetric sensors. *ISPRS Journal of photogrammetry and Remote Sensing*, 60 (6), 387-399.

Hudson, J. A., & Harrison, J. P. (2000). *Engineering rock mechanics-an introduction to the principles*. Elsevier, London, UK.

Hugenholtz, C. H., Whitehead, K., Brown, O. W., Barchyn, T. E., Moorman, B. J., LeClair, A., Riddell, K., and Hamilton, T. (2013). Geomorphological mapping with a small unmanned aircraft system (sUAS): Feature detection and accuracy assessment of a photogrammetrically-derived digital terrain model. *Geomorphology*, 194, 16-24. DOI:10.1016/j.geomorph.03.023.

Hussain, M; Bethel, J. (2004). Project and mission planning. In: McGlone, J., Mikhail, E., Mullen, R. (Eds). *Manual of Photogrammetry*. American Society of Photogrammetry and Remote Sensing, Maryland.

International Society for Rock Mechanics (ISRM). (1978). Commission on standardization of laboratory and field tests: suggested methods for the quantitative description of discontinuities in rock masses. *International Journal of Rock Mechanics and Mining Sciences and Geomechanics Abstracts*, 15(4), pp. 319–368. DOI: 10.1016/0148-409 9062(78)91472-9

International Society of Rock Mechanics (ISRM). (1981). *Rock Characterization, Testing and Monitoring; ISRM Suggested Methods*. Pergamon Press, Oxford, UK. ISBN: 0080273084, 9780080273082

Jaeger, J. C., Cook, N. G. W. (1976). *Fundamentals of Rock Mechanics*, 2nd ed. Chapman and Hall, London.

James, M.R., Robson, S. (2014). Mitigating systematic error in topographic models derived from UAV and ground-based image networks. *Earth Surface Processes and Landforms*, 39, pp. 1413-1420. DOI: 10.1002/esp.3609.

Jenner, H.N., Burfitt, R.H. (1974). Chalk: An engineering material: Paper read at meeting of the Southern Area of the Institution of Civil Engineers, Brighton on 6th March, (unpublished).

Johansson, M. (2003). Exploration into the behaviour of three different high-resolution ground-based laser scanners in the build environment. *Proceedings: CIPA WG 6 International Workshop on Scanning for Cultural Heritage Recording*, Corfu. Greece. <http://www.isprs.org/commission5/workshop>.

Kasser, M. Egels, Y. (2003). *Digital Photogrammetry*. CRC Press, London.

Kliche, C.A. (1999). *Rock Slope Stability SME*, Littleton, CO.

Kolecka, N. (2011). Photo-based 3D scanning vs. laser scanning—Competitive data acquisition methods for digital terrain modelling of steep mountain slopes. *International Archives of the Photogrammetry, Remote Sensing and Spatial Information Sciences*, 38 (4), 203-208.

Konecny, G. (2014). *Geoinformation: remote sensing, photogrammetry and geographic information systems*. CRC Press, London.

- Kumi-Boateng B. (2012). A spatio-temporal based estimation of vegetation changes in the Tarkwa mining area of Ghana. Ph.D. Thesis. University of Mines and Technology, Ghana.
- Lamont-Black, J. (1995). The engineering classification of chalk: with special reference to the origins of fracturing and dissolution. Ph.D. Thesis. University of Brighton, UK.
- Lara, M., Sepúlveda, S. (2008). Remociones en Masa. Curso GL62C. Department of Geology, University of Chile.
- Lato, M., Vöge, M., 2012. Automated mapping of rock discontinuities in 3D lidar and photogrammetry models. *International Journal of Rock Mechanics and Mining Sciences*, 54, 150–158.
- Lautridou, J. P., Letavernier, G., Lindé, K., Etlicher, B., & Ozouf, J. C. (1986). Porosity and frost susceptibility of flints and chalk: laboratory experiments, comparison of 'glacial' and 'periglacial' surface texture of flint materials, and field investigations. In: Sieveking, G. De G. & Hart, M. B. (Eds.). *The Scientific Study of Flint and Chert*. Cambridge University Press, Cambridge, 290pp.
- Lawrence, J. (2007). Engineering properties of chalk in relation to coastal cliff slope instability. Ph.D. Thesis. University of Brighton, UK.
- Lemos de Oliveira, V. (2013). Structural Geology and Fracture Patterns in the Chalk of Sussex, UK. (BSc dissertation in Geology). University of Brighton. UK.
- Leyshon, P. R., Lisle, R. J. (1996). *Stereographic Projection Techniques in Structural Geology*. Butterworth and Heinemann, Oxford.
- Li, Z., Zhu, C., Gold, C. (2004). *Digital terrain modeling: principles and methodology*. CRC press, London.
- Lichti, D.D., Gordon, S., Stewart, M., Franke, J., Tsakiri, M. (2002). Comparison of digital photogrammetry and laser scanning. *Proceedings: CIPA W6 International Workshop*, 1–2 September, Corfu, Greece, pp. 39–47.
- Linder, W. (2003). *Digital photogrammetry. Theory and applications*. Springer, Berlin.
- Linder, W. (2006). *Digital photogrammetry. A practical course*. Springer, Berlin.

- Lord, J., Clayton, C., & Mortimore, R. (2002). Engineering in Chalk, CIRIA Report C574, CIRIA, London.
- Luhmann, T., Robson, S., Kyle, S., Harley, I. (2011). Close range photogrammetry: principles, techniques and applications. Whittles publishing, Scotland.
- Luhmann, T., Robson, S., Kyle, S., Boehm, J. (2013). Close Range Photogrammetry and 3D Imaging, 2nd ed. Walter de Gruyter, Berlin/Boston.
- Luhmann, T., Fraser, C., & Maas, H. G. (2016). Sensor modelling and camera calibration for close-range photogrammetry. ISPRS Journal of Photogrammetry and Remote Sensing, 115, 37-46.
- Martino, S., & Mazzanti, P. (2014). Integrating geomechanical surveys and remote sensing for sea cliff slope stability analysis: the Mt. Pucci case study (Italy). Natural Hazards and Earth System Sciences, 14(4), 831-848.
- Mathis, J.I. (2011). Photogrammetric discontinuity mapping as applied to structural interpretation and drillhole planning at Barrick's Williams pit. Slope Stability 2011, Vancouver, Canada, September, 2011.
- McCaffrey, K. J. W., Jones, R. R., Holdsworth, R. E., Wilson, R. W., Clegg, P., Imber, J., Holliman, N., and Trinks, I. (2005). Unlocking the spatial dimension: digital technologies and the future of geoscience fieldwork. Journal of the Geological Society, 162, 927–938.
- McInnes RG., Moore R. (2011). Cliff instability and erosion management in Great Britain – A good practice guide. Halcrow Group Ltd. 88.
- Met Office. (2016a). <http://www.metoffice.gov.uk/climate/uk/regional-climates/so>. Last accessed: 01/05/2017.
- Met Office. (2016b). <http://www.metoffice.gov.uk/pub/data/weather/uk/climate/stationdata/eastbournedata.txt>. Last accessed: 01/05/2017.
- Moore, R., Davis, G. (2015). Cliff instability and erosion management in England and Wales. Journal of coastal conservation. Planning and Management 19, 771-782.
- Mortimore, R. (1986). Stratigraphy of the Upper Cretaceous White Chalk of Sussex. Proceedings of the Geologists' Association, 97 (2), 97-139.

Mortimore, R. (1997). The Chalk of Sussex and Kent. Geologists' Association Guide No. 57.

Mortimore, R., Lawrence, J., Pope, D., Duperret, A., Genter, A. (2004a). Coastal cliff geohazards in weak rock: the UK Chalk cliffs of Sussex. In: Mortimore, R., and Duperret, A. (Eds.). Coastal Chalk Cliff Instability. Geological Society, London, Engineering Geology Special Publications, 20, 3-31.

Mortimore, R., Stone, K., Lawrence, J., Duperret, A. (2004b). Chalk physical properties and cliff instability. In: Mortimore, R., and Duperret, A. (Eds.). Coastal Chalk Cliff instability. Geological Society, London, Engineering Geology Special Publications, 20, 75-88.

Mortimore, R. N. (2014). Logging the Chalk. Whittles Publishing, Scotland.

Mott MacDonald. (2005). Brighton and Hove WWT Scheme. Main Ground Investigation Phase I. Interpretative Report. London, UK.

Mott MacDonald. (2009). *Brighton and Hove WWT Scheme. Black Rock Quaternary Cliff Stability Study*. London, UK.

Niethammer U, Rothmund S, James MR, Travelletti J, Joswig M. (2010). UAV-based remote sensing of landslides. International Archives of Photogrammetry, Remote Sensing and Spatial Information Sciences, XXXVIII: 496–501.

Nunes, M., Ferreira, O., Schaefer, M., Clifton, J., Baily, B., Moura, D., and Loureiro, C. (2009). Hazard assessment in rock cliffs at Central Algarve (Portugal): A tool for coastal management, Ocean Coast. Manage., 52, 506–515.

Ove Arup & Partners. (1984). Black Rock Interchange: Geotechnical Report. UK.

Pahl, P. J. (1981). Estimating the mean length of discontinuity traces. International Journal of Rock Mechanics and Mining Sciences & Geomechanics Abstracts, 18, 221–8.

Paparoditis, N., Dissard, O. (2002). 3D data acquisition from visible images. In: Kasser, M. Egels, Y. (Eds.). Digital photogrammetry. CRC Press, London.

Poropat, G.V. (2008). Remote characterization of surface roughness of rock discontinuities. In: Potvin, Y., Carter, J., Dyskin, A., Jeffrey, R. (Eds.), Proceedings 1st Southern Hemisphere International Rock Mechanics Symposium, Perth, September 16–19, 2008, vol. 2, pp. 447–458.

Priest, S. D. and Hudson, J. A. (1981). Estimation of discontinuity spacing and trace length using scanline surveys. *International Journal of Rock Mechanics and Mining Sciences & Geomechanics Abstracts*, 18, 183–97.

Priest, S.D. (1993). *Discontinuity Analysis for Rock Engineering*. Chapman and Hall, London. 473 pp.

Ray, S. (2000a). The photometry of image formation. In: Jacobson, R., Ray, S., Attridge, G., Axford, N. (Eds.). *The Manual of Photography: Photographic and digital imaging*. 9th ed. Focal Press, Oxford, 459pp.

Ray, S. (2000b). The geometry of image formation. In: Jacobson, R., Ray, S., Attridge, G., Axford, N. (Eds.). *The Manual of Photography: Photographic and digital imaging*. 9th ed. Focal Press, Oxford, 459pp.

Ray, S. (2000c). Types of camera. In: Jacobson, R., Ray, S., Attridge, G., Axford, N. (Eds.). *The Manual of Photography: Photographic and digital imaging*. 9th ed. Focal Press, Oxford, 459pp.

Remondino, F., Barazzetti, L., Nex, F., Scaioni, M., and Sarazzi, D. (2011). UAV Photogrammetry for mapping and 3D modelling – current status and future perspectives. *International Archives of the Photogrammetry, Remote Sensing and Spatial Information Sciences*, Volume XXXVIII-1/C22, 2011 ISPRS Zurich 2011 Workshop, 14-16 September 2011, Zurich, Switzerland.

Richards, L. R., Leg, G. M. M., & Whittle, R. A. (1978). Appraisal of stability conditions in rock slopes. In: Bell, F.G. (Ed). *Foundation engineering in difficult ground*. Newnes-Butterworths, London, 449-512.

Robinson, D., and Williams, R. (1983). The Sussex coast past and present. In: Robinson, D., and Williams, R. (Eds.). *Sussex: Environment, Landscape and Society*. The Geography Editorial Committee, University of Sussex, England: 50-66.

Robinson, D., Jerwood, L. (1987a). Weathering of chalk shore platforms during harsh winters in South-East England. *Marine Geology* 77, 1–14.

Robinson, D., and Jerwood, L. (1987b). Frost and salt weathering of chalk shore platforms near Brighton, Sussex, UK. *Transactions of the Institute of British Geographers*, 12, 217-226.

Rocscience (2016a). Rocscience software products – *DIPS 7.0*. <http://www.rocscience.com>

Rocscience (2016b). Kinematic Analysis - Toppling, Planar Sliding, Wedge Sliding. <https://www.rocscience.com/rocscience/products/dips/resources/tutorials>. Last accessed: 01/09/2016.

Roman, W., Johnson, R. (2012). Application of digital photogrammetry to rock cut slope design. Transportation Research Board (TRB) 91st Annual Meeting. January 22-16, 2012. Washington, D.C. 1-18.

Salvini, R., Francioni, M., Riccucci, S., Vanciani, F., Callegari, I. (2013). Photogrammetry and laser scanning for analyzing slope stability and rock fall runout along the Domodossola–Iselle railway, the Italian Alps. *Geomorphology*, 185, pp. 110-122. DOI: 10.1016/j.geomorph.2012.12.020.

Schenk, T. (2005). Introduction to photogrammetry. The Ohio State University, Columbus.

Selby, M. (1993). *Hillslope Materials and Processes*, 2nd ed. Oxford University Press, Oxford.

Slatton, K. C., Carter, W. E., Shrestha, R. L., and Dietrich, W. (2007). Airborne laser swath mapping: achieving the resolution and accuracy required for geosurficial research. *Geophysical Research Letters*, 34, p. L23S10. DOI: 10.1029/2007GL031939.

Stavrou, A., Lawrence, J. A., Mortimore, R. N., & Murphy, W. (2011). A geotechnical and GIS based method for evaluating risk exposition along coastal cliff environments: a case study of the chalk cliffs of southern England. *Natural hazards and earth system sciences*, 11(11), 2997-3011. DOI:10.5194/nhess-11-2997-2011.

Sturzenegger, M., and Stead, D. (2009a). Close-range terrestrial digital photogrammetry and terrestrial laser scanning for discontinuity characterization on rock cuts. *Engineering Geology*, 106(3), pp. 163–182. DOI: 10.1016/j.enggeo.2009.03.004.

Sturzenegger, M., and Stead, D. (2009b). Quantifying discontinuity orientation and persistence on high mountain rock slopes and large landslides using terrestrial remote sensing techniques. *Natural Hazards and Earth System Sciences*, 9(2), pp. 267–287. DOI: 10.5194/nhess-9-267-2009.

Taibi, S., Duperret, A., & Fleureau, J. M. (2009). The effect of suction on the hydro-mechanical behaviour of chalk rocks. *Engineering Geology*, 106(1), 40-50.

Terzaghi, K. (1962). Stability of steep slopes on hard unweathered rock. *Geotechnique*, 12 (4):1-20.

Triggs, B., McLauchlan, P. F., Hartley, R. I., & Fitzgibbon, A. W. (1999). Bundle adjustment—a modern synthesis. In *International workshop on vision algorithms* (pp. 298-372). Springer Berlin Heidelberg.

Tuckey, Z., & Stead, D. (2016). Improvements to field and remote sensing methods for mapping discontinuity persistence and intact rock bridges in rock slopes. *Engineering Geology*, 208, 136-153.

Vandycke, S. (2002). Palaeostress records in Cretaceous formations in NW Europe: extensional and strike-slip events in relationships with Cretaceous-Tertiary inversion tectonics. *Tectonophysics*, 357, 119-136.

Vosselman, G., Sester, M., Mayer, H. (2004). Basic computer vision techniques. In: McGlone, J., Mikhail, E., Mullen, R. (Eds). *Manual of Photogrammetry*. American Society of Photogrammetry and Remote Sensing, Maryland.

Wyllie, D.C. and Mah, C.W. (2004). Rock Slope Engineering. 4th ed. Taylor & Francis, London.

Young, E. (2012). dGPS. In: Cook, S.J., Clarke, L.E. & Nield, J.M. (Eds.) Geomorphological Techniques (Online Edition). British Society for Geomorphology, London. ISSN: 2047-0371.

APPENDIX

Appendix 1: Object Distance Calculation Spreadsheet (ODCS)

ADAM TECHNOLOGY			
Object Distance Calculation Spreadsheet			
Camera Name:	Nikon D81000		
Camera Details			
	Width	Height	
Number of pixels:	7360 × 4912		Image size: 36.2 megapixels
Image sensor dimensions:	35.9 × 24	mm	Field of View Crop/Lens multiplier: 1.0 × 1.0
Actual focal length of lens x adapter:	24	mm	Equivalent 35mm camera focal length: 24 mm
Actual aperture: f/	8		Equivalent 35mm camera aperture: f/8.0
Focus distance:	50.00	m	Depth of field: 6.43m - Infinity
Desired circle of confusion (diameter):	2	pixels	Hyperfocal distance: 7.40 m
Size of each pixel in CCD array:	4.88 × 4.89		um
Warning: Diffraction limited! Minimum circle of confusion = 2.2 pixels (10.7 microns)			
Required Conversion:	Distance -> Pixel Size		Project Type: Terrestrial Strips
Model Details		Accuracy Estimates	
Desired object distance:	50	m	Estimated image accuracy: 0.5 pixels
Ground coverage of each Image:	74.8 × 50	m	Distance between camera stations: 25.0 m
Ground pixel size:	10.2 × 10.2	mm	Object distance/base ratio: 2.00 : 1
Desired target size:	61	mm	Estimated plan accuracy: 5.1 mm
Desired target + border size:	162.6	mm	Estimated distance accuracy: 10.2 mm
Nominal DTM point density:	40.6	mm per point	Estimated overall accuracy: 12.4 mm
Photoscale:	2083 : 1		
Area Details for Strip Planning			
Width and height of area:	100 × 60	m	Distance between camera stations: 29.9 m
Desired horizontal overlap:	60% =	44.9 m	Distance between strips: 32.5 m
Desired vertical overlap:	35% =	17.5 m	Number of images per strip: 3
Desired driving speed:	5	m/s	Number of strips: 2
Max. movement during exposure:	0.3	pixels	Total number of images: 6
Min. required shutter speed:	1/	1600 seconds	
Capture interval:	5.98		seconds

Source: ADAM Technology, 2010.

Appendix 2: Digital photogrammetry

2.1 Parameters of the camera calibration (interior orientation)

The 11 parameters of the camera calibration are defined as follows (ADAM technology, 2010; Luhmann (2016):

- **Principal distance (c):** perpendicular distance from the image plane in the negative z' direction to the perspective centre (O'). When focused at infinity, c is roughly equal to the focal length ($C \approx f'$). The unit is measured in millimeters (mm).

- **Principal point H'** (x_p, y_p): foot of perpendicular formed between the perspective centre and the image plane, with image coordinates (x'_0, y'_0). The unit is measured in millimeters (mm).

- **Radial distortion $\Delta r'$** (**K1, K2, K3, K4**): parameters that describe an observation error deviation closer to or further from the principal point. This error is created by variations in refraction at each component lens within the camera's compound lens. The unit is measured in microns (μm). $\Delta r'$ was calculated by the formula:

$$\Delta r'_{rad} = a_1 \cdot r' + a_3 \cdot r'^3 + a_5 \cdot r'^5 + a_7 \cdot r'^7 \quad (9.1)$$

The image coordinates are corrected proportionally:

$$\Delta x'_{rad} = x' \frac{\Delta r'_{rad}}{r'} \quad \Delta y'_{rad} = y' \frac{\Delta r'_{rad}}{r'} \quad (9.2)$$

With $\Delta r'_{rad}$, $\Delta x'_{rad}$, $\Delta y'_{rad}$ = radial distortion in image radius and image coordinates; r' = radial distance from the principal point; a_1 to a_7 are constants given in the camera calibration certificate.

- **Decentering distortion Δ_{dec}** (**P1, P2**): It is caused by vertical displacement or rotations of individual lens components from a perfect alignment at the time of camera manufacture. The unit is measured in microns (μm). Δ_{dec} and was determined by the formula:

$$\Delta x = P_1 \cdot (3 \cdot x^2 + y^2) + 2 \cdot P_2 \cdot x \cdot y \quad (9.3)$$

$$\Delta y = 2 \cdot P_1 \cdot x \cdot y + P_2 \cdot (x^2 + 3 \cdot y^2) \quad (9.4)$$

Where P_1 and P_2 are the decentering distortion parameters; x and y represent the image-coordinates (mm).

- **Scaling factors Δ_{aff}** (**B1, B2**): pixel scaling factors. Affinity and shear are utilized to determine deviations of the image coordinate structure regarding orthogonality and uniform scale of the coordinate axes. These are able to compensate differences in scale between pixels width and height. Δ_{aff} was defined by the standard formula:

$$\Delta x'_{aff} = B_1 \cdot x' + B_2 \cdot y' \quad \Delta y'_{aff} = 0 \quad (9.5)$$

With $\Delta x'_{aff}$, $\Delta y'_{aff}$ = affine distortion; B_1 = horizontal image scale (pixel spacing); B_2 = image shear.

2.2 Centroiding algorithm for digitising ground control points

For digital images the target centre is determined by centroid methods, in which a local centroid is used to define the centre. That centroid is a weighted mean of the pixel coordinates within a processing window, which is determined automatically following the standard formula (Luhmann et al., 2011):

$$X_M = \frac{\sum_{i=1}^n (x_i T g_i)}{\sum_{i=1}^n (T g_i)} \quad Y_M = \frac{\sum_{i=1}^n (y_i T g_i)}{\sum_{i=1}^n (T g_i)} \quad (10.1)$$

Where n is the number of processed pixels in a specific window; g_i represents the pixel value at the pixel location (x_i, y_i) . A decision function T is utilized to determine whether a pixel will be used for a calculation.

2.3 Least-Square Matching (LSM) for Relative Only Points.

Based on Konecny (2014) and Luhmann et al. (2011) the automated LSM model is summarized here as follows:

In image correlation, each density value $f(x, y)$ of the pattern matrix should correspond to an identical density value $g(x, y)$ of the search matrix, apart from a noise component $e(x, y)$:

$$f(x, y) - e(x, y) = g(x, y) \quad (11.1)$$

Assuming an affine deformation of the search matrix for a geometric and radiometric adjustment, each pixel value at location (x, y) in the reference image f_i is specified as the corresponding geometrically and radiometrically converted pixel value g_i at location (x, y) in the search image, the Eq. 6.1 may be expanded to form the observation equation:

$$f_i(x, y) - e_i(x, y) = r_0 + r_1 g_i(x', y') \quad i = 1, \dots, n \quad (11.2)$$

With:

$$\begin{aligned} x' &= a_0 + a_1 x + a_2 y & n &= pq \text{ (window size)} \\ y' &= b_0 + b_1 x + b_2 y & n &\geq 8 \end{aligned}$$

Where a_0 and b_0 are translation parameters which determine the relative shift between reference image and search image. x', y' are non-integer coordinate values. As the image function $g(x', y')$ is non-linear, the linearization of the Eq. 11.2 results in:

$$f_i(x, y) - e_i(x, y) = g^0(x, y) + g_x da_0 + g_x x da_1 + g_x y da_2 + g_y db_0 + g_y x db_1 + g_y y db_2 + r_0 + r_1 g^0(x, y) \quad (11.3)$$

Where the partial differential is calculated by the pixel value gradients g_x and g_y :

$$g_x = \frac{\partial g^0(x, y)}{\partial x} \quad g_y = \frac{\partial g^0(x, y)}{\partial y} \quad (11.4)$$

In the Eq. (11.3), the initial translation parameters are determined with the assumptions:

$$a_0^0 = a_2^0 = b_0^0 = b_1^0 = r_0^0 = 0 \quad \text{and} \quad a_1^0 = b_2^0 = r_1^0 = 1$$

The setting equations must be resolved iteratively. By each iteration unknowns values are corrected. This process brings new pixel value differences between search image and rectified reference image, until the least-square sum of the corrections is less than a predetermined threshold (Luhmann et al., 2011).

2.4 Image Resection

Base on Konecny (2014) and Luhmann et al. (2013), the conventional numerical model of resection uses a minimum of three measured image coordinates of reference points (X, Y, Z) , and with known parameters of interior orientation, the following structure of corrections are derived from collinearity equations (Eqs. 1.1 and 1.2):

$$x'_i + vx' = F(\mathbf{X}_0, \mathbf{Y}_0, \mathbf{Z}_0, \omega, \varphi, \kappa, x'_0, c, \Delta x', X, Y, Z) \quad (12.1)$$

$$y'_i + vy' = F(\mathbf{X}_0, \mathbf{Y}_0, \mathbf{Z}_0, \omega, \varphi, \kappa, y'_0, c, \Delta y', X, Y, Z) \quad (12.2)$$

Where function F is a depiction of Eqs. 1.1 and 1.2. The bold values represent the parameters of the exterior orientation, which are introduced as six unknowns. $x'_0, y'_0, c, \Delta x', \Delta y'$ are the five parameters of interior orientation. Regarding the six unknowns, these are non-linear equations, which are linearized by the Taylor series using its linear components as an initial approximation.

The system of Eqs. 12.1 and 12.2 for image resection can be linearized using the Taylor series and solved by least-squares adjustment. Each of the measured image points supplies two corrections equations, with iterations to follow (Albertz and Kreiling, 1989; Luhmann et al., 2013):

$$vx'_i = \left(\frac{\partial x'_i}{\partial X_0} \right)^0 dX_0 + \left(\frac{\partial x'_i}{\partial Y_0} \right)^0 dY_0 + \left(\frac{\partial x'_i}{\partial Z_0} \right)^0 dZ_0 + \left(\frac{\partial x'_i}{\partial \omega} \right)^0 d\omega + \left(\frac{\partial x'_i}{\partial \varphi} \right)^0 d\varphi + \left(\frac{\partial x'_i}{\partial \kappa} \right)^0 d\kappa - (x'_i - x_i^0) \quad (12.3)$$

$$vy'_i = \left(\frac{\partial y'_i}{\partial X_0}\right)^0 dX_0 + \left(\frac{\partial y'_i}{\partial Y_0}\right)^0 dY_0 + \left(\frac{\partial y'_i}{\partial Z_0}\right)^0 dZ_0 + \left(\frac{\partial y'_i}{\partial \omega}\right)^0 d\omega + \left(\frac{\partial y'_i}{\partial \varphi}\right)^0 d\varphi + \left(\frac{\partial y'_i}{\partial \kappa}\right)^0 d\kappa - (y'_i - y_i'^0)$$

Where; x'_i and y'_i : measured image coordinates; $x_i'^0$ and $y_i'^0$: image coordinates which represent the approximate values for all unknowns. By simplifying collinearity equations (1.1 and 1.2) through substituting k_x and k_y for the numerators and N for the denominator, this is obtained:

$$x' = x'_0 + -c \frac{k_x}{N} + \Delta x' \quad y' = y'_0 + -c \frac{k_y}{N} + \Delta y' \quad (12.4)$$

From which the derivatives of Eq. (12.3) are given as follows:

$$\begin{aligned} \frac{\partial x'}{\partial X_0} &= \frac{-c'}{N^2} (r_{13}k_x - r_{11}N) & \frac{\partial x'}{\partial Y_0} &= \frac{-c'}{N^2} (r_{23}k_x - r_{21}N) & \frac{\partial x'}{\partial Z_0} &= \frac{-c'}{N^2} (r_{33}k_x - r_{31}N) \\ \frac{\partial x'}{\partial \omega} &= \frac{-c'}{N} \cdot \left\{ \frac{k_x}{N} \cdot [r_{13}(Y - Y_0) - r_{23}(Z - Z_0)] - r_{31}(Y - Y_0) + r_{21}(Z - Z_0) \right\} \\ \frac{\partial x'}{\partial \varphi} &= \frac{-c'}{N} \cdot \left\{ \frac{k_x}{N} \cdot [k_y \cdot \sin k - k_x \cdot \cos k] - N \cdot \cos k \right\} & \frac{\partial x'}{\partial \kappa} &= \frac{-c'}{N} \cdot k_y \\ \frac{\partial y'}{\partial X_0} &= \frac{-c'}{N^2} (r_{13}k_y - r_{12}N) & \frac{\partial y'}{\partial Y_0} &= \frac{-c'}{N^2} (r_{23}k_y - r_{22}N) & \frac{\partial y'}{\partial Z_0} &= \frac{-c'}{N^2} (r_{33}k_y - r_{32}N) \\ \frac{\partial y'}{\partial \omega} &= \frac{-c'}{N} \cdot \left\{ \frac{k_y}{N} \cdot [r_{13}(Y - Y_0) - r_{23}(Z - Z_0)] - r_{32}(Y - Y_0) + r_{22}(Z - Z_0) \right\} \\ \frac{\partial y'}{\partial \varphi} &= \frac{-c'}{N} \cdot \left\{ \frac{k_y}{N} \cdot [k_y \cdot \sin k - k_x \cdot \cos k] + N \cdot \sin k \right\} & \frac{\partial y'}{\partial \kappa} &= \frac{-c'}{N} \cdot k_x \end{aligned}$$

Appendix 3: Interior orientation report

Status:	Successful
Posteriori Variance Factor:	1.02
Computed Image Accuracy:	0.25 pixels (X = 0.25 pixels, Y = 0.26 pixels)
Number of Degrees of Freedom:	36,762

Image Residuals

Image	RMS Error (pixels)			Number of Active Points
	X	Y	Total	
DSC_3483.TIF	0.088	0.153	0.176	148
DSC_3484.TIF	0.110	0.170	0.202	274
DSC_3485.TIF	0.142	0.153	0.209	340
DSC_3486.TIF	0.173	0.200	0.264	317
DSC_3487.TIF	0.149	0.180	0.234	442
DSC_3488.TIF	0.140	0.191	0.237	464
DSC_3489.TIF	0.146	0.174	0.227	521
DSC_3490.TIF	0.163	0.177	0.241	488
DSC_3491.TIF	0.140	0.199	0.244	431
DSC_3492.TIF	0.135	0.166	0.214	630
DSC_3493.TIF	0.146	0.196	0.245	464
DSC_3494.TIF	0.138	0.186	0.231	492
DSC_3495.TIF	0.146	0.214	0.259	308
DSC_3496.TIF	0.212	0.213	0.300	303
DSC_3497.TIF	0.135	0.176	0.221	538
DSC_3498.TIF	0.151	0.164	0.223	815
DSC_3499.TIF	0.165	0.170	0.237	743
DSC_3500.TIF	0.134	0.168	0.215	741
DSC_3501.TIF	0.105	0.167	0.197	576
DSC_3502.TIF	0.145	0.191	0.240	331
DSC_3503.TIF	0.139	0.155	0.208	555
DSC_3504.TIF	0.205	0.198	0.285	349
DSC_3505.TIF	0.134	0.151	0.202	634
DSC_3506.TIF	0.165	0.182	0.246	717
DSC_3507.TIF	0.253	0.275	0.373	676
DSC_3508.TIF	0.255	0.178	0.311	735
DSC_3509.TIF	0.245	0.210	0.322	805
DSC_3510.TIF	0.173	0.160	0.236	932
DSC_3511.TIF	0.163	0.177	0.241	979
DSC_3512.TIF	0.236	0.197	0.308	642
DSC_3513.TIF	0.164	0.168	0.235	870
DSC_3514.TIF	0.177	0.187	0.258	538
DSC_3515.TIF	0.178	0.170	0.246	745
DSC_3516.TIF	0.179	0.145	0.230	871

Image	RMS Error (pixels)			Number of Active Points
	X	Y	Total	
DSC_3517.TIF	0.189	0.170	0.254	734
DSC_3518.TIF	0.178	0.166	0.244	678
DSC_3519.TIF	0.200	0.179	0.268	648
DSC_3520.TIF	0.148	0.167	0.223	720
DSC_3521.TIF	0.099	0.134	0.167	331
DSC_3522.TIF	0.152	0.189	0.243	598
DSC_3523.TIF	0.186	0.186	0.264	572
DSC_3524.TIF	0.167	0.173	0.240	771
DSC_3525.TIF	0.174	0.156	0.234	743
DSC_3526.TIF	0.178	0.163	0.242	828
DSC_3527.TIF	0.180	0.190	0.262	828
DSC_3528.TIF	0.330	0.216	0.394	534
DSC_3529.TIF	0.236	0.180	0.297	541
DSC_3530.TIF	0.176	0.171	0.245	827
DSC_3531.TIF	0.181	0.171	0.249	923
DSC_3532.TIF	0.175	0.168	0.243	860
DSC_3533.TIF	0.154	0.177	0.235	643
DSC_3534.TIF	0.176	0.172	0.247	290
DSC_3535.TIF	0.120	0.177	0.214	355
DSC_3536.TIF	0.155	0.174	0.233	543
DSC_3537.TIF	0.185	0.177	0.256	429
DSC_3538.TIF	0.172	0.166	0.239	587
DSC_3539.TIF	0.158	0.171	0.233	484
DSC_3540.TIF	0.165	0.173	0.239	519
DSC_3541.TIF	0.190	0.223	0.293	100
DSC_3542.TIF	0.157	0.182	0.240	479
DSC_3543.TIF	0.173	0.171	0.243	424
DSC_3544.TIF	0.174	0.179	0.249	481
DSC_3545.TIF	0.188	0.199	0.274	374
DSC_3546.TIF	0.152	0.187	0.241	438
DSC_3547.TIF	0.168	0.194	0.257	370
DSC_3548.TIF	0.203	0.174	0.268	278
DSC_3549.TIF	0.153	0.196	0.249	246
DSC_3550.TIF	0.185	0.210	0.280	200

Appendix 3: Interior Orientation report (Cont. 1)

Control Point Residuals

Control Point ID	Image Co-ordinate Residuals (pixels)			Ground Co-ordinate Residuals (metre)			Adjusted Ground Co-ordinates (metre)		
	Observations	X	Y	X	Y	Z	X	Y	Z
101	7	0.744	0.492	0.03	0.06	0.19	539133.67	101494.61	34.32
102	7	0.816	0.233	0.08	0.05	0.21	539039.73	101544.50	40.59
103	7	1.273	0.568	0.08	0.01	0.19	538910.74	101592.73	45.45
104	7	1.070	0.404	0.04	0.04	0.16	538784.26	101637.75	43.81
105	6	0.552	0.468	0.15	-0.01	0.19	538620.35	101732.87	21.76
201	5	0.362	0.329	-0.02	-0.03	0.03	539267.39	101415.27	6.75
202	6	0.938	0.551	-0.00	0.00	-0.01	539228.94	101438.32	6.10
203	5	0.900	0.079	-0.01	0.02	-0.04	539194.48	101455.13	5.90
204	6	1.269	0.641	-0.03	-0.01	-0.03	539142.75	101484.11	7.28
205	5	0.299	0.480	-0.08	-0.03	-0.02	539086.22	101512.35	5.51
206	5	1.392	0.677	-0.01	0.05	-0.06	539061.53	101521.33	5.62
207	6	2.083	1.518	0.02	0.04	-0.06	539038.25	101532.43	7.11
208	6	3.394	2.314	-0.01	-0.00	-0.07	539004.70	101547.06	6.22
209	5	0.578	0.286	0.01	0.01	-0.09	538978.37	101557.02	5.52
210	6	1.260	0.810	0.02	-0.01	-0.09	538953.39	101568.89	5.23
211	6	1.393	0.960	0.01	-0.02	-0.09	538916.91	101585.62	4.44
212	7	0.820	1.099	-0.06	-0.11	-0.07	538868.91	101606.28	4.27
213	5	1.559	0.768	-0.07	-0.02	-0.13	538825.94	101614.38	2.78
214	7	2.965	1.014	-0.07	-0.09	-0.06	538762.89	101643.36	6.29
215	7	0.885	0.695	-0.03	-0.06	-0.03	538720.05	101666.99	5.58
216	7	0.567	0.556	0.01	0.00	-0.04	538679.59	101684.44	4.26
217	7	1.118	0.581	0.03	-0.00	-0.02	538644.99	101703.94	3.74
218	6	0.801	0.548	-0.08	0.11	-0.07	538589.02	101713.35	7.14
Component SE		1.400	0.839	0.06	0.05	0.11			
3D SE					0.13				

Camera Calibration: Parameter Correlation Matrix

Camera: "Nikon_D810_24mm (NEW)"

Parameter	C	X _p	Y _p	K ₁	K ₂	K ₃	P ₁	P ₂	B ₁	B ₂	Max	
C	1.00	0.00	0.01	-0.01	-0.00	0.00	-0.01	0.00	0.09	-0.01	-0.34	Image 42 _y
X _p		1.00	0.00	0.00	0.00	-0.00	0.03	-0.00	0.02	0.11	0.48	Image 48 _x
Y _p			1.00	-0.00	0.00	-0.00	-0.00	-0.04	-0.10	0.01	0.25	Image 37 _z
K ₁				1.00	-0.94	0.88	0.06	0.15	0.04	-0.01	-0.94	K ₂
K ₂					1.00	-0.98	-0.05	-0.04	-0.01	0.01	-0.98	K ₃
K ₃						1.00	0.05	0.04	0.00	-0.01	-0.98	K ₂
P ₁							1.00	0.08	-0.01	-0.16	-0.48	Image 28 _ω
P ₂								1.00	-0.08	-0.02	0.80	K ₁
B ₁									1.00	0.01	-0.77	Point 104 _z
B ₂										1.00	0.71	Point 104 _x

Camera Calibration: Interior Orientation Results

Camera Name	Parameter	Final Value		σ _{Final Value}	
			(pixels)		(pixels)
Nikon_D810_24mm (NEW)	C	24.78		4.80e-003	0.86
	X _p	3.51e-003	0.72	3.93e-003	0.80
	Y _p	3.19e-003	0.65	3.85e-003	0.79
	K ₁	2.03e-004	418.86	1.14e-007	0.23
	K ₂	-3.16e-007	-304.20	6.25e-010	0.60
	K ₃	2.19e-010	98.05	1.06e-012	0.48
	P ₁	-2.10e-005	-6.63	5.52e-007	0.17
	P ₂	-1.05e-004	-25.37	3.84e-007	0.09
	B ₁	-3.61e-003	-13.30	3.78e-004	1.39
	B ₂	-5.28e-004	-1.30	4.11e-004	1.01

Appendix 4: Exterior orientation report

Status:	Successful
Posteriori Variance Factor:	1.02
Computed Image Accuracy:	0.25 pixels (X = 0.25 pixels, Y = 0.26 pixels)
Number of Degrees of Freedom:	36,762

Image Residuals

Image	RMS Error (pixels)			Number of Active Points
	X	Y	Total	
DSC_3483.TIF	0.088	0.153	0.176	148
DSC_3484.TIF	0.110	0.170	0.202	274
DSC_3485.TIF	0.142	0.153	0.209	340
DSC_3486.TIF	0.173	0.200	0.264	317
DSC_3487.TIF	0.149	0.180	0.234	442
DSC_3488.TIF	0.140	0.191	0.237	464
DSC_3489.TIF	0.146	0.174	0.227	521
DSC_3490.TIF	0.163	0.177	0.241	488
DSC_3491.TIF	0.140	0.199	0.244	431
DSC_3492.TIF	0.135	0.166	0.214	630
DSC_3493.TIF	0.146	0.196	0.245	464
DSC_3494.TIF	0.138	0.186	0.231	492
DSC_3495.TIF	0.146	0.214	0.259	308
DSC_3496.TIF	0.212	0.213	0.300	303
DSC_3497.TIF	0.135	0.176	0.221	538
DSC_3498.TIF	0.151	0.164	0.223	815
DSC_3499.TIF	0.165	0.170	0.237	743
DSC_3500.TIF	0.134	0.168	0.215	741
DSC_3501.TIF	0.105	0.167	0.197	576
DSC_3502.TIF	0.145	0.191	0.240	331
DSC_3503.TIF	0.139	0.155	0.208	555
DSC_3504.TIF	0.205	0.198	0.285	349
DSC_3505.TIF	0.134	0.151	0.202	634
DSC_3506.TIF	0.165	0.182	0.246	717
DSC_3507.TIF	0.253	0.275	0.373	676
DSC_3508.TIF	0.255	0.178	0.311	735
DSC_3509.TIF	0.245	0.210	0.322	805
DSC_3510.TIF	0.173	0.160	0.236	932
DSC_3511.TIF	0.163	0.177	0.241	979
DSC_3512.TIF	0.236	0.197	0.308	642
DSC_3513.TIF	0.164	0.168	0.235	870
DSC_3514.TIF	0.177	0.187	0.258	538
DSC_3515.TIF	0.178	0.170	0.246	745
DSC_3516.TIF	0.179	0.145	0.230	871

Image	RMS Error (pixels)			Number of Active Points
	X	Y	Total	
DSC_3517.TIF	0.189	0.170	0.254	734
DSC_3518.TIF	0.178	0.166	0.244	678
DSC_3519.TIF	0.200	0.179	0.268	648
DSC_3520.TIF	0.148	0.167	0.223	720
DSC_3521.TIF	0.099	0.134	0.167	331
DSC_3522.TIF	0.152	0.189	0.243	598
DSC_3523.TIF	0.186	0.186	0.264	572
DSC_3524.TIF	0.167	0.173	0.240	771
DSC_3525.TIF	0.174	0.156	0.234	743
DSC_3526.TIF	0.178	0.163	0.242	828
DSC_3527.TIF	0.180	0.190	0.262	828
DSC_3528.TIF	0.330	0.216	0.394	534
DSC_3529.TIF	0.236	0.180	0.297	541
DSC_3530.TIF	0.176	0.171	0.245	827
DSC_3531.TIF	0.181	0.171	0.249	923
DSC_3532.TIF	0.175	0.168	0.243	860
DSC_3533.TIF	0.154	0.177	0.235	643
DSC_3534.TIF	0.176	0.172	0.247	290
DSC_3535.TIF	0.120	0.177	0.214	355
DSC_3536.TIF	0.155	0.174	0.233	543
DSC_3537.TIF	0.185	0.177	0.256	429
DSC_3538.TIF	0.172	0.166	0.239	587
DSC_3539.TIF	0.158	0.171	0.233	484
DSC_3540.TIF	0.165	0.173	0.239	519
DSC_3541.TIF	0.190	0.223	0.293	100
DSC_3542.TIF	0.157	0.182	0.240	479
DSC_3543.TIF	0.173	0.171	0.243	424
DSC_3544.TIF	0.174	0.179	0.249	481
DSC_3545.TIF	0.188	0.199	0.274	374
DSC_3546.TIF	0.152	0.187	0.241	438
DSC_3547.TIF	0.168	0.194	0.257	370
DSC_3548.TIF	0.203	0.174	0.268	278
DSC_3549.TIF	0.153	0.196	0.249	246
DSC_3550.TIF	0.185	0.210	0.280	200

Appendix 4: Exterior orientation report (Cont. 1)

Control Point Residuals

Control Point ID	Image Co-ordinate Residuals (pixels)			Ground Co-ordinate Residuals (metre)			Adjusted Ground Co-ordinates (metre)		
	Observations	X	Y	X	Y	Z	X	Y	Z
101	7	0.744	0.492	0.03	0.06	0.19	539133.67	101494.61	34.32
102	7	0.816	0.233	0.08	0.05	0.21	539039.73	101544.50	40.59
103	7	1.273	0.568	0.08	0.01	0.19	538910.74	101592.73	45.45
104	7	1.070	0.404	0.04	0.04	0.16	538784.26	101637.75	43.81
105	6	0.552	0.468	0.15	-0.01	0.19	538620.35	101732.87	21.76
201	5	0.362	0.329	-0.02	-0.03	0.03	539267.39	101415.27	6.75
202	6	0.938	0.551	-0.00	0.00	-0.01	539228.94	101438.32	6.10
203	5	0.900	0.079	-0.01	0.02	-0.04	539194.48	101455.13	5.90
204	6	1.269	0.641	-0.03	-0.01	-0.03	539142.75	101484.11	7.28
205	5	0.299	0.480	-0.08	-0.03	-0.02	539086.22	101512.35	5.51
206	5	1.392	0.677	-0.01	0.05	-0.06	539061.53	101521.33	5.62
207	6	2.083	1.518	0.02	0.04	-0.06	539038.25	101532.43	7.11
208	6	3.394	2.314	-0.01	-0.00	-0.07	539004.70	101547.06	6.22
209	5	0.578	0.286	0.01	0.01	-0.09	538978.37	101557.02	5.52
210	6	1.260	0.810	0.02	-0.01	-0.09	538953.39	101568.89	5.23
211	6	1.393	0.960	0.01	-0.02	-0.09	538916.91	101585.62	4.44
212	7	0.820	1.099	-0.06	-0.11	-0.07	538868.91	101606.28	4.27
213	5	1.559	0.768	-0.07	-0.02	-0.13	538825.94	101614.38	2.78
214	7	2.965	1.014	-0.07	-0.09	-0.06	538762.89	101643.36	6.29
215	7	0.885	0.695	-0.03	-0.06	-0.03	538720.05	101666.99	5.58
216	7	0.567	0.556	0.01	0.00	-0.04	538679.59	101684.44	4.26
217	7	1.118	0.581	0.03	-0.00	-0.02	538644.99	101703.94	3.74
218	6	0.801	0.548	-0.08	0.11	-0.07	538589.02	101713.35	7.14

Exterior Orientations

Image	Location (metre)			Rotation (°)				
	X	Y	Z	ω	ϕ	κ	Bearing	Tilt
DSC_3483.TIF	539270.23 ± 0.03	101360.01 ± 0.02	21.17 ± 0.03	96.59 ± 0.01	-24.37 ± 0.03	3.67 ± 0.00	24.51	6.00
DSC_3484.TIF	539259.62 ± 0.02	101364.85 ± 0.02	21.52 ± 0.03	96.61 ± 0.01	-24.29 ± 0.03	3.49 ± 0.00	24.43	6.02
DSC_3485.TIF	539249.27 ± 0.02	101371.17 ± 0.02	22.20 ± 0.03	96.74 ± 0.01	-24.53 ± 0.03	3.31 ± 0.00	24.68	6.13
DSC_3486.TIF	539239.02 ± 0.02	101377.46 ± 0.02	22.25 ± 0.03	96.41 ± 0.01	-24.21 ± 0.03	3.44 ± 0.00	24.34	5.84
DSC_3487.TIF	539228.49 ± 0.02	101383.30 ± 0.02	21.49 ± 0.03	96.31 ± 0.01	-24.26 ± 0.03	3.68 ± 0.00	24.39	5.75
DSC_3488.TIF	539217.58 ± 0.02	101389.19 ± 0.02	21.19 ± 0.03	96.14 ± 0.01	-24.41 ± 0.03	3.53 ± 0.00	24.53	5.59
DSC_3489.TIF	539206.76 ± 0.02	101394.96 ± 0.02	21.39 ± 0.03	96.37 ± 0.01	-24.39 ± 0.03	3.41 ± 0.00	24.52	5.80
DSC_3490.TIF	539196.15 ± 0.02	101400.79 ± 0.02	21.06 ± 0.03	96.64 ± 0.01	-24.33 ± 0.03	3.81 ± 0.00	24.48	6.04
DSC_3491.TIF	539185.28 ± 0.02	101406.83 ± 0.01	20.69 ± 0.03	96.57 ± 0.01	-24.19 ± 0.03	3.45 ± 0.00	24.33	5.99
DSC_3492.TIF	539174.58 ± 0.01	101412.72 ± 0.01	20.33 ± 0.03	96.30 ± 0.01	-24.57 ± 0.03	3.48 ± 0.00	24.70	5.73
DSC_3493.TIF	539163.81 ± 0.01	101418.60 ± 0.01	20.55 ± 0.03	96.50 ± 0.01	-24.47 ± 0.03	3.38 ± 0.00	24.61	5.91
DSC_3494.TIF	539153.17 ± 0.01	101424.57 ± 0.01	20.89 ± 0.03	96.32 ± 0.01	-24.18 ± 0.03	3.38 ± 0.00	24.31	5.77
DSC_3495.TIF	539142.55 ± 0.01	101430.44 ± 0.01	20.51 ± 0.02	96.36 ± 0.01	-24.56 ± 0.03	3.06 ± 0.00	24.69	5.79
DSC_3496.TIF	539131.78 ± 0.01	101436.00 ± 0.01	20.96 ± 0.02	95.88 ± 0.01	-24.22 ± 0.03	2.84 ± 0.00	24.33	5.36
DSC_3497.TIF	539120.79 ± 0.01	101441.61 ± 0.01	20.83 ± 0.02	96.06 ± 0.01	-24.48 ± 0.03	3.02 ± 0.00	24.60	5.52
DSC_3498.TIF	539109.88 ± 0.01	101447.51 ± 0.01	21.05 ± 0.02	96.57 ± 0.01	-24.22 ± 0.03	3.48 ± 0.00	24.37	5.99
DSC_3499.TIF	539099.16 ± 0.01	101453.10 ± 0.01	20.09 ± 0.02	96.31 ± 0.01	-24.25 ± 0.03	3.17 ± 0.00	24.38	5.75
DSC_3500.TIF	539088.10 ± 0.01	101458.76 ± 0.01	20.04 ± 0.02	96.23 ± 0.01	-24.59 ± 0.03	3.05 ± 0.00	24.72	5.66
DSC_3501.TIF	539077.61 ± 0.01	101464.47 ± 0.01	20.18 ± 0.02	96.14 ± 0.01	-24.51 ± 0.03	2.75 ± 0.00	24.64	5.59

Appendix 4: Exterior orientation report (Cont. 2)

DSC_3502.TIF	539067.19 ± 0.01	101470.20 ± 0.01	20.19 ± 0.02	96.56 ± 0.01	-24.43 ± 0.02	3.20 ± 0.00	24.57	5.97
DSC_3503.TIF	539056.35 ± 0.01	101475.67 ± 0.01	20.33 ± 0.02	96.49 ± 0.00	-24.58 ± 0.02	2.90 ± 0.00	24.72	5.90
DSC_3504.TIF	539046.06 ± 0.01	101481.23 ± 0.01	20.46 ± 0.02	96.41 ± 0.01	-24.51 ± 0.02	2.98 ± 0.00	24.64	5.83
DSC_3505.TIF	539035.45 ± 0.01	101486.58 ± 0.01	20.83 ± 0.02	96.34 ± 0.00	-24.40 ± 0.02	2.95 ± 0.00	24.54	5.77
DSC_3506.TIF	539024.85 ± 0.01	101492.19 ± 0.01	20.79 ± 0.02	96.48 ± 0.00	-24.40 ± 0.02	3.09 ± 0.00	24.54	5.90
DSC_3507.TIF	539014.04 ± 0.01	101497.73 ± 0.01	20.98 ± 0.02	96.42 ± 0.00	-24.46 ± 0.02	2.92 ± 0.00	24.60	5.84
DSC_3508.TIF	539002.99 ± 0.01	101502.10 ± 0.01	21.00 ± 0.02	96.58 ± 0.00	-24.49 ± 0.02	2.91 ± 0.00	24.64	5.98
DSC_3509.TIF	538991.59 ± 0.01	101506.27 ± 0.01	20.80 ± 0.02	96.60 ± 0.00	-24.59 ± 0.02	2.68 ± 0.00	24.73	6.00
DSC_3510.TIF	538980.57 ± 0.01	101510.22 ± 0.01	20.50 ± 0.02	96.66 ± 0.00	-24.44 ± 0.02	2.92 ± 0.00	24.59	6.06
DSC_3511.TIF	538969.34 ± 0.01	101514.06 ± 0.01	20.12 ± 0.02	96.70 ± 0.00	-24.45 ± 0.02	2.97 ± 0.00	24.60	6.10
DSC_3512.TIF	538958.13 ± 0.01	101518.06 ± 0.01	20.18 ± 0.02	96.91 ± 0.00	-24.45 ± 0.02	3.04 ± 0.00	24.61	6.29
DSC_3513.TIF	538946.57 ± 0.01	101522.14 ± 0.01	20.42 ± 0.02	96.86 ± 0.00	-24.52 ± 0.02	2.81 ± 0.00	24.68	6.24
DSC_3514.TIF	538935.13 ± 0.01	101526.05 ± 0.01	20.42 ± 0.02	96.89 ± 0.00	-24.49 ± 0.02	2.92 ± 0.00	24.65	6.26
DSC_3515.TIF	538923.70 ± 0.01	101529.86 ± 0.01	20.57 ± 0.02	96.81 ± 0.00	-24.43 ± 0.02	2.87 ± 0.00	24.58	6.19
DSC_3516.TIF	538912.50 ± 0.01	101533.67 ± 0.01	20.60 ± 0.02	96.69 ± 0.00	-24.53 ± 0.02	2.96 ± 0.00	24.68	6.08
DSC_3517.TIF	538901.26 ± 0.01	101537.46 ± 0.01	20.77 ± 0.02	96.56 ± 0.00	-24.34 ± 0.02	2.73 ± 0.00	24.48	5.98
DSC_3518.TIF	538890.09 ± 0.01	101540.94 ± 0.01	20.95 ± 0.02	96.68 ± 0.00	-24.42 ± 0.02	2.70 ± 0.00	24.57	6.08
DSC_3519.TIF	538878.61 ± 0.01	101544.72 ± 0.01	20.57 ± 0.02	96.60 ± 0.00	-24.43 ± 0.02	2.70 ± 0.00	24.58	6.01
DSC_3520.TIF	538867.12 ± 0.01	101548.60 ± 0.01	20.61 ± 0.02	96.51 ± 0.01	-24.42 ± 0.02	2.95 ± 0.00	24.56	5.92
DSC_3521.TIF	538855.62 ± 0.01	101552.59 ± 0.01	20.49 ± 0.02	96.51 ± 0.01	-24.61 ± 0.02	2.91 ± 0.00	24.75	5.92
DSC_3522.TIF	538843.96 ± 0.01	101556.67 ± 0.01	20.62 ± 0.03	96.49 ± 0.01	-24.79 ± 0.03	2.80 ± 0.00	24.93	5.89
DSC_3523.TIF	538832.39 ± 0.01	101560.62 ± 0.01	20.71 ± 0.03	96.47 ± 0.01	-24.78 ± 0.03	2.53 ± 0.00	24.92	5.87
DSC_3524.TIF	538820.82 ± 0.01	101564.46 ± 0.01	20.24 ± 0.03	96.62 ± 0.01	-24.77 ± 0.03	2.77 ± 0.00	24.92	6.01
DSC_3525.TIF	538809.09 ± 0.01	101568.42 ± 0.01	20.48 ± 0.03	96.55 ± 0.01	-24.67 ± 0.03	2.91 ± 0.00	24.81	5.95
DSC_3526.TIF	538797.39 ± 0.01	101572.24 ± 0.01	20.55 ± 0.03	96.53 ± 0.01	-24.76 ± 0.03	2.70 ± 0.00	24.91	5.92
DSC_3527.TIF	538785.64 ± 0.01	101576.27 ± 0.01	20.76 ± 0.03	96.53 ± 0.01	-24.85 ± 0.03	2.85 ± 0.00	24.99	5.92
DSC_3528.TIF	538774.57 ± 0.01	101580.29 ± 0.01	21.02 ± 0.03	96.43 ± 0.01	-24.74 ± 0.03	2.64 ± 0.00	24.88	5.84
DSC_3529.TIF	538763.61 ± 0.01	101585.04 ± 0.01	21.02 ± 0.03	96.41 ± 0.01	-25.06 ± 0.03	2.74 ± 0.00	25.19	5.81
DSC_3530.TIF	538752.83 ± 0.01	101589.78 ± 0.01	20.82 ± 0.03	96.34 ± 0.01	-24.90 ± 0.03	2.84 ± 0.00	25.03	5.74
DSC_3531.TIF	538741.76 ± 0.01	101594.99 ± 0.01	20.59 ± 0.03	96.28 ± 0.01	-24.92 ± 0.03	2.62 ± 0.00	25.05	5.69
DSC_3532.TIF	538730.46 ± 0.01	101600.17 ± 0.01	20.75 ± 0.03	96.37 ± 0.01	-24.89 ± 0.03	2.94 ± 0.00	25.02	5.78
DSC_3533.TIF	538719.33 ± 0.01	101605.25 ± 0.01	20.74 ± 0.03	96.39 ± 0.01	-24.96 ± 0.03	2.76 ± 0.00	25.09	5.79
DSC_3534.TIF	538708.13 ± 0.01	101610.69 ± 0.01	20.92 ± 0.03	96.49 ± 0.01	-24.90 ± 0.03	2.79 ± 0.00	25.04	5.88
DSC_3535.TIF	538697.05 ± 0.01	101615.79 ± 0.01	20.85 ± 0.03	96.56 ± 0.01	-24.93 ± 0.03	2.84 ± 0.00	25.07	5.95
DSC_3536.TIF	538686.16 ± 0.01	101620.88 ± 0.01	21.00 ± 0.03	96.61 ± 0.01	-25.02 ± 0.03	2.76 ± 0.00	25.17	5.99
DSC_3537.TIF	538675.30 ± 0.01	101625.91 ± 0.01	21.22 ± 0.03	96.69 ± 0.01	-25.00 ± 0.03	2.69 ± 0.00	25.15	6.06
DSC_3538.TIF	538664.50 ± 0.01	101631.10 ± 0.01	21.16 ± 0.03	96.71 ± 0.01	-25.09 ± 0.03	2.52 ± 0.00	25.24	6.07
DSC_3539.TIF	538653.76 ± 0.01	101636.43 ± 0.01	21.19 ± 0.03	96.65 ± 0.01	-25.13 ± 0.03	2.61 ± 0.00	25.28	6.02
DSC_3540.TIF	538643.07 ± 0.01	101641.47 ± 0.01	20.98 ± 0.03	96.69 ± 0.01	-25.09 ± 0.03	2.60 ± 0.00	25.24	6.05
DSC_3541.TIF	538632.05 ± 0.02	101646.25 ± 0.02	20.76 ± 0.03	96.81 ± 0.01	-25.08 ± 0.03	2.52 ± 0.00	25.24	6.17
DSC_3542.TIF	538621.21 ± 0.01	101651.12 ± 0.02	20.48 ± 0.03	97.02 ± 0.01	-25.06 ± 0.03	2.76 ± 0.00	25.22	6.36
DSC_3543.TIF	538610.86 ± 0.02	101655.78 ± 0.02	20.47 ± 0.03	96.88 ± 0.01	-25.30 ± 0.03	2.58 ± 0.00	25.46	6.22
DSC_3544.TIF	538600.25 ± 0.02	101660.89 ± 0.02	20.59 ± 0.03	96.88 ± 0.01	-25.29 ± 0.03	2.24 ± 0.00	25.45	6.22
DSC_3545.TIF	538589.51 ± 0.02	101665.58 ± 0.02	21.03 ± 0.03	96.79 ± 0.01	-24.92 ± 0.03	2.19 ± 0.00	25.08	6.15
DSC_3546.TIF	538578.71 ± 0.02	101670.52 ± 0.02	21.22 ± 0.03	96.42 ± 0.01	-25.17 ± 0.03	2.01 ± 0.00	25.31	5.81
DSC_3547.TIF	538569.10 ± 0.02	101675.16 ± 0.02	21.38 ± 0.03	96.69 ± 0.01	-25.40 ± 0.03	2.27 ± 0.00	25.56	6.04
DSC_3548.TIF	538563.19 ± 0.02	101677.74 ± 0.02	21.28 ± 0.03	96.27 ± 0.01	-25.45 ± 0.03	1.69 ± 0.00	25.58	5.66
DSC_3549.TIF	538557.49 ± 0.02	101680.49 ± 0.02	21.11 ± 0.03	96.75 ± 0.01	-25.45 ± 0.03	2.00 ± 0.00	25.60	6.09
DSC_3550.TIF	538552.84 ± 0.02	101682.98 ± 0.02	20.79 ± 0.03	96.90 ± 0.01	-25.31 ± 0.03	2.32 ± 0.00	25.47	6.23

Appendix 5: Input data table for kinematic analysis

ID	dip (°)	dip direction (°)	Discontinuity type	Centre Coord. X	Centre Coord. Y	Centre Coord. Z	Persistence (m)
1	78.8	61.9	Joints	538870.15	101607.07	29.54	0.9
2	61.8	210	Joints	538873.34	101603.91	11.56	2
3	63.6	136.7	Joints	538827.99	101614.73	3.99	0.96
4	70.7	60.5	Joints	538832.8	101624.33	29.19	1.16
5	76	44.3	Joints	538833.05	101623.8	30.74	2
6	89.6	17.4	Joints	538835.27	101622.98	30.77	0.76
7	89.6	199.7	Joints	538834.21	101623.39	33.22	2
8	89.2	337.3	Joints	538772.76	101639.32	28.09	1.91
9	72.4	212.3	Joints	538777.21	101639.82	33.44	1.07
10	61.6	239.6	Joints	538779.92	101636.04	22.7	0.74
11	83.2	9	Joints	538821.53	101625.22	12.78	1.63
12	56.1	295.3	Joints	538825.22	101618.26	9.92	1.17
13	53	273.6	Joints	538794.44	101618.58	12.48	2.32
14	79.3	205.8	Joints	538788.5	101630.64	13.82	0.82
15	74.9	56.6	Joints	538751.66	101649.72	28.93	1.39
16	85.1	137.2	Joints	538749.12	101651.86	30.77	1.7
17	84.6	142.2	Joints	538750.62	101651.11	34.75	2
18	57.1	242.4	Joints	538746.52	101651.38	23.32	2.09
19	88.3	346.9	Joints	538745.8	101653.12	24.04	0.58
20	82.3	334.5	Joints	538775.41	101635.22	8.18	2
21	62	236.4	Joints	538741.4	101652.42	12.56	1.82
22	86.6	207.3	Joints	538731.22	101668.28	17.01	2
23	80.6	204.9	Joints	538729.42	101671.69	29.39	0.97
24	75.3	53.2	Joints	538713.17	101669.59	6.55	1.04
25	71.9	224.7	Joints	538742.03	101647.88	6.37	1.06
26	72.1	210.9	Joints	538743.64	101648.09	8.13	0.72
27	74.8	222.5	Joints	538705.03	101671.73	12.47	1.25
28	56.8	197.2	Joints	538695.23	101680.76	12.83	1.61
29	89	69.6	Joints	538689.93	101683.28	13.4	0.86
30	88.5	311	Joints	538688.72	101683.92	13.47	0.77
31	78.2	9.2	Joints	538689.22	101683.88	13.85	0.59
32	60.6	197.3	Joints	538689.21	101683.79	12.94	2
33	56.3	50.8	Joints	538680.5	101684.92	12.05	0.99
34	38.6	25.5	Joints	538677.14	101687.13	13.69	2
35	69	231.3	Joints	538713.35	101676.35	30.86	1.18
36	76.1	64	Joints	538673.49	101690.36	22.86	2
37	72.7	207.5	Joints	538673.82	101690.07	23.6	2
38	88.4	194.8	Joints	538666.44	101697.58	8.43	1.81
39	50.2	64.9	Joints	538675.58	101686.61	6.5	1.18
40	87.8	199.3	Joints	538873.06	101606.1	33.84	2
41	76.4	199.1	Joints	538933.09	101578.22	7.73	0.61
42	68.2	228.8	Joints	538932.41	101578.97	10.98	0.48
43	74.1	38.1	Joints	538952.65	101574.1	34.1	0.7
44	65.2	225.6	Joints	538954.33	101568.2	7.61	2
45	76.3	216.4	Joints	538954.95	101571.81	27.93	1.63
46	83.7	206.6	Joints	538956.44	101566.53	6.74	0.78
47	88.1	71.9	Joints	538964.24	101562.26	11.48	0.91
48	83.9	147.6	Joints	538919.95	101585.37	10.9	1.08
49	79.7	195.3	Joints	538960.23	101568.3	28.71	1.5
50	78.6	62.6	Joints	539009.02	101550.7	29.4	2
51	76.9	210.9	Joints	539007.17	101547.16	10.46	1.69
52	74.9	193	Joints	539002.19	101548.62	10.24	0.57
53	64.1	236.4	Joints	539031.37	101537.1	14.91	0.71
54	83.8	68.2	Joints	539034.27	101534.81	8.76	0.8
55	64.6	228.1	Joints	539051.05	101532.3	36.59	0.91
56	85.5	154.8	Joints	539052.71	101530.94	30.36	0.91
57	66.9	213.2	Joints	539052.41	101531.03	15.32	1.27
58	63.9	31.5	Joints	539053.78	101530.2	16.95	0.82
59	74.2	46.2	Joints	539055.5	101529.1	16.63	0.94
60	53.9	171.5	Joints	539043.75	101536.78	20.75	2
61	51.6	226.6	Joints	539079.34	101517.23	8.51	0.47
62	49.2	201.5	Joints	539093.67	101510.25	12.28	1.24
63	57.9	170.4	Joints	539092.47	101513.55	16.72	1.6

ID	dip (°)	dip direction (°)	Discontinuity type	Centre Coord. X	Centre Coord. Y	Centre Coord. Z	Persistence (m)
64	74.7	65.1	Joints	539092.57	101513.33	17.4	0.86
65	82.7	206.3	Joints	539108.78	101502.44	13.52	0.97
66	82.1	216.7	Joints	539110.14	101502.81	22.98	2
67	56.6	198.2	Joints	539128.86	101491.76	13.34	2.15
68	84.6	47.8	Joints	539134.95	101488.34	6.59	0.71
69	62.7	7.6	Joints	539128.47	101492.31	15.13	1.05
70	86.8	66.8	Joints	539126.42	101492.22	15.03	0.71
71	54	189.3	Joints	539180.1	101465.29	9.04	2
72	52.5	57.2	Joints	539172.33	101468.97	10.39	0.39
73	88.2	219.7	Joints	539172.54	101468.84	9.63	1.36
74	72.6	89.1	Joints	539172.75	101468.47	9.53	1.07
75	81.2	60.9	Joints	539167.26	101471.07	10.52	1.06
76	66	217.8	Joints	539189.39	101458.47	9.74	2.58
77	87.3	81.2	Joints	539185.22	101460.69	8.1	0.7
78	65.3	207	Joints	539185.29	101460.44	6.45	0.84
79	61.1	81.2	Joints	539185.5	101460.29	6.79	0.47
80	74.4	82.5	Joints	539189.74	101457.45	8.44	0.62
81	87.8	219.3	Joints	538648.59	101705.48	8.49	0.61
82	65.8	264.3	Joints	538734.72	101667.75	28.94	4.09
83	89.1	212.2	Joints	538748.01	101650.26	13.9	1.32
84	79.2	278.2	Joints	538748.04	101649.49	22.61	2
85	85.9	41.7	Joints	538748.08	101649.54	23.46	1.11
86	83.3	3	Joints	538751.61	101649.63	23.31	2.01
87	86.9	222.2	Joints	538754.33	101650.39	35.39	5.14
88	78.1	207.2	Joints	538741.49	101649	8.07	1.07
89	80.9	262.1	Joints	538743.96	101648.01	8.19	0.57
90	85.6	191.9	Joints	538740.66	101649.28	8.25	0.68
91	87.8	2.7	Joints	538740.6	101649.23	7.66	2
92	63.5	280.4	Joints	538754.17	101641.91	6.12	2.14
93	84.1	211.6	Joints	538752.69	101644.11	6.86	1.16
94	74	292.4	Joints	538752.32	101644.94	6.97	1.24
95	72.6	52.4	Joints	538752.3	101644.76	7.95	2
96	65.5	205.3	Joints	538754.1	101642.7	7.9	0.64
97	70.2	225.1	Joints	538770.83	101642.43	37.24	1.12
98	79.8	60.9	Joints	538770.53	101642.74	38.77	0.61
99	77.8	74.9	Joints	538774.19	101638.73	25.66	1.07
100	87.2	65.4	Joints	538775.12	101638.54	25.54	0.49
101	87.2	348.5	Joints	538776.22	101635.18	11.36	2
102	87.6	31.5	Joints	538784.76	101636.19	34.35	0.48
103	76.8	34.2	Joints	538789.39	101634.03	32.17	0.42
104	89.9	157.2	Joints	538781.43	101635.99	22.41	1.44
105	85.8	24	Joints	538780.76	101635.83	22.63	0.62
106	89.9	165.2	Joints	538783.1	101636.28	26.94	0.75
107	60.9	266.2	Joints	538777.88	101634.73	6.83	2
108	83.9	144.3	Joints	538750.18	101649.49	24.08	4.48
109	64.2	215.1	Joints	538875.75	101602.97	22.3	2.93
110	79.8	355	Joints	538901.62	101592	7.6	2
111	69.4	71.3	Joints	538918.41	101585.18	11.85	0.48
112	75.4	217.8	Joints	538938.13	101575.75	6.01	0.34
113	87.9	7.6	Joints	538956.01	101566.7	7.68	2
114	60.6	26.8	Joints	538955.25	101567.11	6.91	1
115	60.8	236.1	Joints	538957.35	101565.59	9.95	1.88
116	88.6	71.8	Joints	538945.3	101572.38	10.14	0.75
117	55.6	95.4	Joints	538962.3	101563.04	11.43	1.28
118	85.6	193.6	Joints	538963.33	101562.73	14.31	1.07
119	80.9	138	Joints	538906.19	101591.65	12.92	2.52
120	71.9	32.4	Joints	538905.44	101591.42	12.92	2
121	62.9	15.9	Joints	538906.68	101591.66	13.6	0.93
122	83.4	137.6	Joints	538914.43	101588.43	31.02	3.35
123	88.4	189.1	Joints	538915.6	101588.96	30.11	3.07
124	43.5	160.6	Joints	539004.97	101547.21	7.66	0.68
125	67.6	209.6	Joints	539003.79	101547.66	7.77	0.35
126	50.1	73.3	Joints	539009.57	101547.3	11.99	0.96
127	80.9	154.1	Joints	539019.21	101551.39	20.77	1.2
128	84.5	38.7	Joints	539019.88	101551.54	20.75	0.67

ID	dip (°)	dip direction (°)	Discontinuity type	Centre Coord. X	Centre Coord. Y	Centre Coord. Z	Persistence (m)
129	48.3	186	Joints	538999.12	101549.55	7.35	0.76
130	72.9	79.8	Joints	539001.72	101548.2	7.84	0.4
131	71.2	198	Joints	539032.9	101535.38	8.45	0.64
132	48.8	235.5	Joints	539025.28	101537.84	8.36	0.25
133	77.8	60.1	Joints	539025.37	101537.91	8.79	0.37
134	48.6	170	Joints	539023.5	101538.4	6.6	0.52
135	84.3	35.9	Joints	539023.54	101538.44	6.97	0.54
136	77.3	35.7	Joints	539045.67	101532.06	11.27	0.37
137	86.9	351	Joints	539049.71	101531.02	20.86	0.65
138	58.4	72.2	Joints	539050.01	101530.99	20.79	0.51
139	56.8	200.6	Joints	539103.17	101505.39	14.47	1.43
140	80.4	58.7	Joints	539091.6	101513.97	18.83	0.79
141	84.2	49.1	Joints	539165.5	101472.61	10.18	1.26
142	73	94	Joints	539165.66	101472.15	10.44	0.96
143	57.1	253.1	Joints	539163.43	101474.16	9.65	1.43
144	89.1	177.6	Joints	539163.3	101473.64	19.04	0.59
145	84.7	39.3	Joints	539163.73	101473.42	18.97	0.55
146	52.6	173.1	Joints	539186.4	101460.12	6.81	0.53
147	66.7	263.1	Joints	539186.63	101459.67	6.29	0.38
148	75.2	203.7	Joints	538748.34	101649.1	22.13	0.77
149	58	94.6	Faults	539115.33	101498.57	15.16	21.11
150	49.3	279.6	Faults	539074.24	101521.19	11.93	16.23
151	65.9	318.7	Faults	539110.82	101502.02	18.64	0.87
152	72.4	260.9	Faults	539109.97	101502.46	17.57	0.81
153	60.9	254.2	Faults	539109.03	101502.92	16.26	2.19
154	69.6	279.6	Faults	539107.63	101502.8	14.06	4.02
155	59.6	294.5	Faults	539160.46	101477.14	18.17	5.58
156	62.9	294.2	Faults	539156.56	101478.96	11.28	9.76
157	55.2	112.6	Faults	538665.21	101701.64	24.77	6.58
158	62	308.3	Faults	538657.87	101704.05	15.38	6.18
159	58	287.8	Faults	538697.47	101681.71	17.72	7
160	68.2	278.7	Faults	538691.59	101681.15	8.62	6.71
161	68.6	290.9	Faults	538725.51	101672.83	35.66	5.77
162	86.1	22.8	Faults	538773.71	101636.22	8.08	3.19
163	77.9	335.4	Faults	538771.92	101636.57	5.15	2.16
164	72.2	136.4	Faults	538794.47	101628.17	11.31	12.84
165	69	290.5	Faults	538780.56	101632.23	5.24	5.16
166	69.3	313.7	Faults	538832.22	101625.26	35.07	10.09
167	54.8	303.4	Faults	538923.8	101583.78	11.54	4.51
168	60.2	301.4	Faults	538921.02	101585.06	6.36	4.15
169	71.5	111.1	Faults	538956.75	101566.33	6.47	3.69
170	65	281.7	Faults	538953.2	101569.1	6.16	3.37
171	62.9	110.8	Faults	538942.41	101574.31	9.48	9.72
172	64.4	90.4	Faults	538961.97	101565.55	23.36	5.09
173	79.5	99.5	Faults	538947.99	101571.41	6.83	3.5
174	61.6	281.6	Faults	538961.77	101563.43	12.52	1.71
175	62.1	126.7	Faults	538968.95	101561.39	11.37	13.67
176	56.5	281.2	Faults	538979.42	101558.43	10.88	10.12
177	48.5	101.4	Faults	538972.38	101561.14	7.67	2.46
178	74.3	258.7	Faults	538976.45	101559.11	7.6	2.26
179	60.5	289.9	Faults	539006.4	101546.81	7.28	4.79
180	63.6	272.8	Faults	539024.05	101553.04	37.83	1.27
181	63.2	294.9	Faults	539023.24	101553.51	35.63	2.72
182	59.1	308.2	Faults	539053.95	101526.52	6.36	1.92
183	71	81.4	Faults	539109.92	101503.4	30.27	6.28
184	66.1	96.1	Faults	539111.74	101501.99	29.07	3.16
185	66.3	281.4	Faults	539080.41	101521.79	22.89	12.97
186	50.3	283.5	Faults	538864.02	101609.94	7.19	7.47
187	73	104	Faults	538839.1	101617.94	16.33	10.93
188	62.4	283.4	Faults	538847.12	101612.85	16.38	12.89
189	68.8	251	Faults	538685.15	101683.55	10.88	12.77
190	0.5	78.8	Bedding Planes	538678.14	101686.36	17.89	8.33
191	1.8	310.5	Bedding Planes	538678.12	101685.98	15.81	6.35
192	5.1	202.6	Bedding Planes	538676.15	101686.98	10.94	3.88
193	2.8	23.1	Bedding Planes	538719.43	101670.59	13.4	2.94

ID	dip (°)	dip direction (°)	Discontinuity type	Centre Coord. X	Centre Coord. Y	Centre Coord. Z	Persistence (m)
194	2.2	18.1	Bedding Planes	538799.74	101616.76	17.22	4.47
195	0.6	351.2	Bedding Planes	538795.38	101615.41	11.12	3.41
196	2.7	37.8	Bedding Planes	538887.2	101596.3	17.57	3.34
197	2	144.3	Bedding Planes	538944.97	101574.37	20.9	3.58
198	4.7	344.4	Bedding Planes	538993.8	101556.87	21.75	3.59
199	2.4	222.3	Bedding Planes	539056.16	101528.99	18.12	2.79
200	2.1	219	Bedding Planes	539050.01	101531.43	18.04	3.13
201	2.7	140	Bedding Planes	539060.48	101525.96	18.14	2.78
202	0.9	133.3	Bedding Planes	539203.51	101452.85	12.36	2.23
203	1	91.1	Bedding Planes	539191.18	101457.61	12.8	2
204	2.8	120.4	Bedding Planes	539154.43	101480.29	15.32	3.39
205	4.5	37.9	Bedding Planes	539160.92	101475.43	7.58	2.13
206	2.7	39.6	Bedding Planes	539140.74	101490.17	16.72	2
207	0.7	232.7	Bedding Planes	539110.83	101500.47	11.97	2
208	3.7	110.3	Bedding Planes	539104.67	101501.98	9.53	2.32
209	1.8	60.6	Bedding Planes	539102.25	101504.14	9.6	2.97
210	0.9	203.7	Bedding Planes	539090.59	101511.81	11.53	1.33
211	1.3	0.2	Bedding Planes	539067.49	101523.39	21.64	1.97
212	0.4	70.8	Bedding Planes	539076.11	101520.88	12.36	2
213	2.2	59.7	Bedding Planes	539113.39	101501.3	30.7	2
214	3.3	72	Bedding Planes	539062.58	101523.84	13.8	2
215	1.9	132.3	Bedding Planes	539060.83	101526.16	21.72	2.01
216	0.6	90.7	Bedding Planes	539050.71	101529.58	9.11	2
217	0.6	293	Bedding Planes	539065.27	101521.5	8.69	2
218	1.5	139.9	Bedding Planes	539039.34	101534.37	14.13	0.97
219	2.3	46.7	Bedding Planes	539030.03	101537.07	12.67	2
220	1.2	282.4	Bedding Planes	539032.96	101536.6	14.17	1.16
221	2.9	27.9	Bedding Planes	539066.01	101521.9	11.47	1.56
222	3.2	24.9	Bedding Planes	539062.42	101524.68	17.8	2
223	1.4	345.2	Bedding Planes	539045.02	101534.72	17.86	2
224	2.7	154.7	Bedding Planes	539074.09	101520.97	10.72	2
225	1.9	43.8	Bedding Planes	539035.4	101536.19	18.22	2
226	4	48.3	Bedding Planes	539063.58	101525.25	32.49	2
227	1.5	77.9	Bedding Planes	539005.81	101549.95	22.05	3.59
228	1.6	69.9	Bedding Planes	539013.13	101549.98	22.04	2.45
229	1	47.4	Bedding Planes	539001.38	101551.68	17.58	1.85
230	3	343.9	Bedding Planes	538993.6	101555.51	17.34	2.49
231	3.4	40.3	Bedding Planes	538998.31	101554.11	17.48	2.08
232	2.5	46.7	Bedding Planes	539004.04	101548.33	11.09	1.64
233	0.9	213.5	Bedding Planes	539003.79	101550.2	19	2.65
234	0.8	89.1	Bedding Planes	539011.34	101547.13	11.07	2
235	0.5	165.6	Bedding Planes	538985.78	101558.85	17.44	2
236	2.9	148.7	Bedding Planes	538982.02	101562.92	31.71	2
237	2.2	95	Bedding Planes	538951.63	101574.11	33.2	1.74
238	3.1	167.1	Bedding Planes	538968.06	101561.46	17.03	1.46
239	3.4	116.2	Bedding Planes	538952.09	101570.36	9.03	0.97
240	1.8	245	Bedding Planes	538970.82	101560.84	17.05	2.39
241	4.8	41.7	Bedding Planes	538955.26	101570	17	1.09
242	4.9	17.3	Bedding Planes	538963.13	101562.69	8.11	2.17
243	2.1	121.5	Bedding Planes	538962.87	101563.3	16.97	2
244	3.4	67.6	Bedding Planes	538953.45	101572.02	20.81	2
245	0.9	28.7	Bedding Planes	538969.91	101560.44	13.73	3.49
246	2.5	26.5	Bedding Planes	538927.96	101581.18	5.59	1.66
247	3.2	62.7	Bedding Planes	538924.02	101583.97	5.73	2
248	3.4	67.9	Bedding Planes	538923.32	101582.29	20.96	2
249	1.8	66.5	Bedding Planes	538924.12	101583	17.1	2.88
250	2.6	162	Bedding Planes	538912.81	101589.15	11.63	2.72
251	5	130.7	Bedding Planes	538917.49	101585.6	4.97	1.24
252	1.6	188.4	Bedding Planes	538911.36	101591.8	33.07	3.09
253	2.4	182.3	Bedding Planes	538916.01	101589.12	32.99	1.48
254	0.9	52.7	Bedding Planes	538930.74	101581.32	20.99	1.43
255	3.1	121.9	Bedding Planes	538921.55	101586.49	31.87	1.6
256	4.2	156.4	Bedding Planes	538895.61	101593.91	13.39	1.44
257	1.2	88.2	Bedding Planes	538876.15	101602.5	20.37	3.96
258	2.1	172.4	Bedding Planes	538866.07	101608.06	17.64	2.36

ID	dip (°)	dip direction (°)	Discontinuity type	Centre Coord. X	Centre Coord. Y	Centre Coord. Z	Persistence (m)
259	1.1	99.4	Bedding Planes	538875.77	101603.1	17.67	5.53
260	1.2	170.4	Bedding Planes	538857.01	101609.42	13.53	2
261	2.2	129.8	Bedding Planes	538847.01	101616.25	35.86	2
262	1.6	125.4	Bedding Planes	538847.35	101612.28	12.04	1.87
263	4	213.4	Bedding Planes	538842.72	101615.96	12.11	2.17
264	2.3	173.4	Bedding Planes	538836.09	101619.82	17.52	1.66
265	3.2	128.2	Bedding Planes	538829.04	101618.3	12.08	2.69
266	2.2	195.2	Bedding Planes	538817.51	101623.17	18.48	2.85
267	2.5	149.7	Bedding Planes	538809.56	101621.78	20.11	2
268	1.8	326	Bedding Planes	538827.89	101620.78	17.38	1.83
269	3.2	58.4	Bedding Planes	538789.01	101629.91	16.05	1.3
270	0.5	33.5	Bedding Planes	538784.21	101632.24	15.09	2
271	0.9	77.9	Bedding Planes	538771.4	101639.26	7.45	4.03
272	1.7	88.4	Bedding Planes	538771.96	101641.96	15.64	2.03
273	3.4	56.2	Bedding Planes	538767.57	101643.45	20.45	1.58
274	3.4	56.3	Bedding Planes	538765.05	101645.54	31.5	3.95
275	3	162.5	Bedding Planes	538763.94	101642.9	8.48	1.08
276	2.4	279.8	Bedding Planes	538748.93	101649.98	15.81	1.06
277	3.6	74.6	Bedding Planes	538751.3	101648.42	15.85	0.91
278	4.7	66.9	Bedding Planes	538753.54	101643.01	7.4	1.3
279	2.7	220.2	Bedding Planes	538744.21	101651.31	16.01	2
280	1.2	98	Bedding Planes	538735.62	101664.06	17.12	1.56
281	3.7	36.4	Bedding Planes	538730.42	101663.95	7.22	1.32
282	1.7	144.5	Bedding Planes	538719.42	101671.34	17.85	0.7
283	5	43.8	Bedding Planes	538725.67	101670.22	17.76	1.3
284	7.4	38.4	Bedding Planes	538716.71	101668.61	7.16	1.93
285	1.2	180.9	Bedding Planes	538702.87	101671.88	11.06	1.15
286	3.9	134.4	Bedding Planes	538706.87	101672.45	13.95	2.55
287	2.3	144.7	Bedding Planes	538702.39	101673.26	17.93	2
288	3.8	14	Bedding Planes	538708.17	101674.15	17.77	2.22
289	2.2	41	Bedding Planes	538693.38	101682.79	18.01	2
290	1.3	72.5	Bedding Planes	538677.35	101689	23.98	1.84
291	2.5	202.6	Bedding Planes	538698.47	101672.46	10.93	2
292	5	56.6	Bedding Planes	538690.7	101681.57	10.9	2
293	4.6	143.9	Bedding Planes	538666.49	101699.58	17.26	1.77
294	2	234.9	Bedding Planes	538665.22	101698.65	10.49	1.72
295	1.6	162.5	Bedding Planes	538645.49	101704.63	4.85	1.01
296	2.4	198	Bedding Planes	538641.7	101705.47	7.3	1.45
297	2.1	319	Bedding Planes	538648.03	101705.49	9.87	2
298	71	162.4	Joints	538857.64	101610	15.14	3.14
299	71.1	153.9	Joints	538851.6	101608.26	11.25	2.68
300	87.3	165.3	Joints	538867.55	101606.15	7.96	0.49
301	63	177.8	Joints	538828.29	101619.4	14.27	1.48
302	60.3	184.4	Joints	538835.28	101617.01	10.48	2
303	69.9	177.3	Joints	538828.73	101626.81	31.09	2.49
304	81.3	178.9	Joints	538774.25	101639.11	28.73	1.41
305	86.6	164.4	Joints	538781.56	101635.99	23.8	1.49
306	77.4	179.2	Joints	538784.66	101631.33	10.74	2
307	80	168.9	Joints	538789.5	101630.68	13.85	2
308	72.5	181.6	Joints	538767.3	101643.56	11.98	2
309	62.5	150.2	Joints	538747.62	101649.74	12.2	2.29
310	64.9	192.4	Joints	538725.66	101668.02	12.55	2
311	74.4	160.5	Joints	538718.77	101674.99	31.01	1.58
312	83.7	184.3	Joints	538727.11	101672.39	29.54	2
313	84.5	163	Joints	538717.87	101671.92	17.44	2
314	64.7	165.5	Joints	538701.48	101672.08	12.25	2.13
315	83.7	187.2	Joints	538682.7	101683.67	8.1	0.74
316	64.5	155.5	Joints	538673.78	101687.52	11.84	1.37
317	68.5	184.4	Joints	538651.43	101705.88	13.64	1.28
318	79.2	174.1	Joints	538671.12	101691.39	7.29	0.87
319	71.7	174	Joints	538925.44	101582.11	20.01	2
320	71.7	180.6	Joints	538940.68	101576.2	12.17	2
321	81.4	172.4	Joints	538937.03	101582.43	39.65	0.65
322	70.9	178.1	Joints	538949.47	101571.21	13.04	2
323	82.2	170.3	Joints	538964.04	101562.34	10.06	2

ID	dip (°)	dip direction (°)	Discontinuity type	Centre Coord. X	Centre Coord. Y	Centre Coord. Z	Persistence (m)
324	77.8	168.1	Joints	538922.41	101584.38	11.08	1.38
325	62.2	184.5	Joints	538927.43	101580.81	15.92	1
326	67.3	172.8	Joints	538982.31	101562.84	29.19	1.64
327	66.2	161.3	Joints	538964.09	101565.29	29.14	1.22
328	77.4	185.6	Joints	538966.57	101564.16	30.54	2
329	71.5	194.2	Joints	538978.5	101557.44	7.88	0.94
330	76.1	163.3	Joints	539007.81	101550.55	29.32	2.39
331	84	172	Joints	539009.14	101549.09	20.58	2.19
332	66.6	202.8	Joints	539004.8	101547.81	10.71	1.06
333	87.6	182.1	Joints	539033.02	101536.59	14.96	1.68
334	65.5	152	Joints	539030.9	101537.22	14.84	0.91
335	75.7	160.8	Joints	539036.5	101543.08	31.29	2.7
336	59.9	161.3	Joints	539033.76	101535.15	8.57	1.55
337	61.6	152.7	Joints	539040.1	101535.21	16.97	2
338	89.1	174.6	Joints	539046.54	101532.21	16.63	0.69
339	89.8	172.3	Joints	539060.3	101526.16	31.17	1.57
340	78.9	161.3	Joints	539072.43	101523.04	20.69	0.92
341	68.2	179	Joints	539078.01	101520.74	11.78	0.56
342	87.8	168.5	Joints	539077.79	101520.9	14.74	0.78
343	85.3	183	Joints	539089.02	101511.8	9.71	0.6
344	73.7	186.1	Joints	539085.28	101513.79	8.84	0.56
345	83.6	160.9	Joints	539075.25	101524.23	32.1	0.51
346	85.2	178.7	Joints	539101.02	101505.11	7.05	0.56
347	66.2	198.8	Joints	538800.24	101617.79	20.44	1.03
348	72.4	174.9	Joints	539101.8	101509.33	29.55	1.04
349	72.4	172	Joints	539092.19	101513.67	20.53	1
350	67	161.5	Joints	539125.14	101492.16	10.78	1.43
351	69.4	173.4	Joints	539138.02	101491.57	18.91	1.1
352	63.9	181.1	Joints	539135.34	101492.7	22.31	0.58
353	75.4	184.8	Joints	539134.53	101488.51	6.58	0.56
354	60.1	188.8	Joints	539155.22	101479.47	9.36	0.51
355	81	184.9	Joints	539148.94	101482.36	11.29	0.78
356	80.2	167.9	Joints	539175.7	101469.48	13.21	0.92
357	77.7	166.3	Joints	539173.63	101468.14	8.95	1.15
358	78.6	156.6	Joints	539171.97	101468.87	9.73	1.68
359	70.7	164.1	Joints	539166.97	101471.27	10.43	0.8
360	71.2	166.3	Joints	539187.39	101459.96	7.8	0.55
361	67.9	177	Joints	539185.72	101460.5	8.3	0.75
362	71.5	152.9	Joints	538646.04	101705.79	13.11	3.79
363	67.9	200.7	Joints	538677.69	101686.76	11.85	5.36
364	83.8	165.2	Joints	538718.71	101675.49	34.81	1.64
365	68.8	189.6	Joints	538712.33	101674.61	21.45	6.37
366	74.4	190.3	Joints	538714.05	101669.65	8.02	2
367	70.5	181.2	Joints	538725.4	101671.88	22.03	5.38
368	87.4	180.6	Joints	538733.69	101669	31.01	1.95
369	79.4	160.4	Joints	538745.83	101650.55	19.58	1.65
370	77.3	166.9	Joints	538754.04	101648.24	24.73	6.21
371	66.8	198.2	Joints	538745.06	101647.75	8.16	1.33
372	85.9	162.4	Joints	538742.8	101647.99	6.78	0.98
373	79.7	177.2	Joints	538770.11	101642.9	38.78	0.74
374	82.8	170.6	Joints	538774.69	101638.61	25.73	1.05
375	63.9	176.9	Joints	538774.43	101635.88	10.07	0.93
376	79.7	166.1	Joints	538789	101634.08	31.99	1.21
377	85.2	183.5	Joints	538785.11	101636.1	33.7	0.87
378	79.9	183.1	Joints	538782.56	101636.54	29.15	0.86
379	84.9	184.8	Joints	538773.22	101640.5	33.34	1.35
380	81.5	170.2	Joints	538777.2	101640.53	36.09	0.64
381	75.6	165.8	Joints	538779.11	101638.06	29.19	2.12
382	70.4	173.2	Joints	538822.94	101623.39	23.34	2.48
383	83.7	173.6	Joints	538870.96	101606.86	29.25	3.49
384	74.6	168.3	Joints	538936.99	101576.18	5.94	0.72
385	82.6	164.9	Joints	538937.96	101575.8	5.94	0.46
386	82.1	175.2	Joints	538959.5	101570.45	37.07	1.33
387	66.7	176.4	Joints	538959.86	101569.86	33.84	0.64
388	81.4	162.2	Joints	538963.03	101565.17	26.23	1.27

ID	dip (°)	dip direction (°)	Discontinuity type	Centre Coord. X	Centre Coord. Y	Centre Coord. Z	Persistence (m)
389	64.7	159.1	Joints	538944.62	101572.51	10.01	1.12
390	79.5	168.3	Joints	538951.58	101574.18	34.53	2.07
391	84.1	187.7	Joints	538962.01	101563.35	11.46	2
392	77.7	177.9	Joints	538959.92	101564.48	11.54	1
393	64.4	153.4	Joints	538905.25	101591.05	11.47	3.22
394	77.3	163	Joints	539006.07	101547.53	10.22	2
395	78	178.2	Joints	539007.36	101547.13	12.49	0.94
396	82.2	180.1	Joints	539003.28	101547.88	8.37	0.58
397	70.6	191.3	Joints	539001.45	101548.51	8.12	0.83
398	74.3	162	Joints	539027.74	101537.67	10.42	1.57
399	74.7	170.9	Joints	539031.28	101536.42	8.98	0.77
400	66.5	154.5	Joints	539032.68	101535.38	8.5	1.07
401	75.6	161.1	Joints	539032.63	101536.44	11.21	0.73
402	76.1	163.9	Joints	539025.23	101537.97	6.59	1.72
403	76	175.7	Joints	539024.96	101537.9	8.64	0.87
404	73.8	162.5	Joints	539045.35	101532.09	11.24	0.63
405	71.5	168.3	Joints	539049.86	101531.3	18.99	0.48
406	68.9	189.2	Joints	539094.06	101515	28.02	2
407	70.9	182.5	Joints	539164.49	101473.24	9.99	1.31
408	65.5	198.4	Joints	539160.55	101475.98	10.19	0.71
409	61.4	168.2	Joints	539163.33	101473.52	18.37	0.8
410	65.9	187	Joints	539167.59	101471.29	11.64	0.52
411	65.2	164.3	Joints	539167.28	101471.05	8.47	0.81
412	87	236.4	Joints	538867.93	101606.05	7.98	0.45
413	71.1	243.6	Joints	538828.36	101614.59	4.01	0.43
414	88.8	243.3	Joints	538832.81	101623.96	31.77	0.77
415	66.3	259.2	Joints	538798.96	101618.6	19.6	2
416	78.1	242.3	Joints	538778.03	101637.99	28.75	0.76
417	68.9	241	Joints	538772.96	101639.58	11.55	1.44
418	77.7	235.7	Joints	538752.89	101648.27	22.43	2
419	77.4	246.2	Joints	538749.94	101649.41	13.26	1.51
420	89.2	245.3	Joints	538742.48	101654.59	16.13	2
421	85.8	236.9	Joints	538722.74	101673.92	30.39	0.54
422	80.7	232.7	Joints	538718.61	101671.69	17.41	0.77
423	77.1	251.9	Joints	538683.14	101683.37	8.88	0.73
424	77.1	239.8	Joints	538683.71	101683.18	12.89	1.25
425	73.2	238.3	Joints	538673.52	101690.36	21.59	1.23
426	88.5	232.3	Joints	538652.28	101705.42	13.4	1.15
427	70.8	241.6	Joints	538911.58	101589.8	27.44	2
428	72.7	243.5	Joints	538945.11	101573.41	19.64	2.82
429	78.5	233.4	Joints	538920.67	101585.22	11.01	1.22
430	73.7	242.6	Joints	538962.21	101566.19	30.09	1.17
431	64	248.1	Joints	538964.54	101564.55	22.63	0.63
432	79.1	234.8	Joints	538965.07	101565	30.37	1.58
433	79.4	245.3	Joints	539002.47	101548.45	10.25	0.5
434	84.7	255.8	Joints	539034.37	101536.48	15.41	0.79
435	85.7	247.3	Joints	539034.12	101535.07	9.71	1.19
436	80.8	231.5	Joints	539046.65	101537.55	35.16	2.5
437	81.6	240.1	Joints	539058.46	101527.56	32.38	1.3
438	72.5	250.9	Joints	539045.47	101532.95	16.39	1.69
439	80	243.5	Joints	539073	101522.62	20.13	2.1
440	86.2	248	Joints	539088.68	101512.05	9.58	0.89
441	68.4	255	Joints	539086.15	101513.28	8.65	0.47
442	62.7	256.4	Joints	539097.78	101514.37	32.57	1.34
443	85.5	234.6	Joints	539076.14	101523.76	30.68	1.41
444	76.2	239.8	Joints	539101.99	101505.41	13.17	1.09
445	82.4	238.6	Joints	539101.39	101504.81	7.16	0.87
446	79.8	237.6	Joints	539074.99	101524.5	32.23	1.37
447	82.7	244.7	Joints	539100.76	101510.58	29.55	0.78
448	83.5	233.4	Joints	539138.4	101491.41	18.78	0.99
449	86.8	236.7	Joints	539135.66	101492.28	21.19	1.29
450	89.7	233.7	Joints	539175.95	101469.42	13.06	1.14
451	77.1	246	Joints	539188.19	101459.46	8.13	1.87
452	71.1	258.7	Joints	538680.87	101684.67	11.22	1.45
453	70.2	247.6	Joints	538669.56	101695.99	13.18	2.7

ID	dip (°)	dip direction (°)	Discontinuity type	Centre Coord. X	Centre Coord. Y	Centre Coord. Z	Persistence (m)
454	79.9	227.9	Joints	538721.7	101674.14	34.23	1.27
455	74	255.9	Joints	538731.41	101670.63	29.76	2
456	74.2	257.9	Joints	538736.74	101665.17	32.3	1.28
457	84.2	233.2	Joints	538751.24	101650.75	34.82	3.06
458	74.3	254.6	Joints	538738.13	101661.35	19.12	3.53
459	77.1	247.1	Joints	538753.26	101643.2	4.71	0.73
460	82.1	238.4	Joints	538774.06	101635.74	8.16	1.14
461	74.1	244.2	Joints	538773.79	101640.26	32.82	1.07
462	79.2	232.9	Joints	538753.59	101644.52	12.49	2.73
463	80.2	255.7	Joints	538873.57	101605.35	34.18	5.66
464	71.1	242.2	Joints	538903.82	101590.95	10.9	1.92
465	82.5	231.6	Joints	538915.69	101587.27	10.75	3.16
466	66.8	238.6	Joints	538939.94	101576.87	12.41	2
467	70.3	252.1	Joints	538938.43	101575.79	7.47	0.69
468	82.6	232.4	Joints	538953.89	101573.62	34.12	0.51
469	81.8	231.9	Joints	538960.75	101563.96	11.1	1.05
470	79.3	226.8	Joints	538919.79	101587.73	29.67	2.31
471	89.3	235.6	Joints	539003.63	101547.77	8.42	0.38
472	69	239.2	Joints	539028.56	101537.78	11.07	0.85
473	66.6	258.2	Joints	539031.76	101536.24	8.84	0.75
474	72.1	241.6	Joints	539032.81	101536.29	11.08	0.63
475	84.4	240.6	Joints	539025.95	101537.68	8.68	0.72
476	67	244.6	Joints	539102.69	101509.15	30.58	1.05
477	88.8	64.1	Joints	538703.94	101672.12	12.71	0.65
478	89.5	62.1	Joints	538654.92	101703.4	8.9	0.84
479	88	48.9	Joints	538942.52	101582.43	40.11	1
480	83.8	60.1	Joints	539086.14	101513.3	8.96	0.3
481	83.2	57.6	Joints	539089.08	101517.24	24.72	1.14
482	86.6	55.7	Joints	538719.65	101675.23	35.01	1.57
483	85.5	62.7	Joints	538762.1	101644.71	13.7	0.92
484	88.8	47	Joints	538783.61	101636.14	26.86	0.72
485	89.2	51.1	Joints	538780.23	101637.91	28.89	1.85
486	89.1	56.6	Joints	538937.38	101576.07	5.92	0.56
487	87.4	56.1	Joints	538908.11	101591.53	8.52	3.41
488	83.9	61.5	Joints	539050.4	101531.16	19.16	0.42
489	89.8	63.2	Joints	539160.04	101476.3	9.82	1.09